To the Graduate Council:

I am submitting herewith a thesis written by Daniel Michael Rooney entitled "Analysis of an Experimental Pulsed Plasma Accelerator." I have examined the final paper copy of this thesis for form and content and recommend that it be accepted in partial fulfillment of the requirements for the degree of Master of Science, with a major in Aerospace Engineering.

Trevor Moeller, Major Professor

We have read this thesis
and recommend its acceptance:

Basil N. Antar

Roy J. Schulz

Accepted for the Council:

Vice Chancellor and
Dean of Graduate Studies

Thesis
2006
.R65

Analysis of an Experimental Pulsed Plasma Accelerator

A Thesis
Presented for
Master of Science Degree
The University of Tennessee, Knoxville

Daniel Michael Rooney
August 2006

Dedication

This thesis is dedicated to my parents, James and Dolores.

Acknowledgements

I would like to thank all the people who have helped, guided, lectured, taught, advised, and just generally put up with me over the years following this crazy dream of mine. Especially to my advisor Dr. Moeller, whose patience and interest in the subject fueled my own. To Dr. Smith, Bob Rhodes and Newt Wright who put up with my constant questions and had the patience to answer them. To Dr. Schulz who gave me my shot here at UTSI and, along with Dr. Antar, supported me on my committee. To my family and friends who will always keep me in check and not let my head get too big. Lastly to my parents whose constant support and encouragement have kept me going over the years. Thank you.

Abstract

The purpose of this study was to gather and analyze data taken from a laboratory Pulsed Plasma Accelerator to understand its operation, and also for future comparison of the experimental data with predictions made with computer simulations based on the codes named MACH2 and GEMS. This comparison will allow for further validation of these two computer simulations in order to more accurately model the laboratory thruster. Data was collected from three different instruments: B-Dot probes; a laser interferometer; and Rogowski coils. These devices measure the time dependent current sheets, the electron number density, and the capacitor discharge current respectively.

The B-Dot probes were an excellent source of data once the correct procedure for their analysis was determined. Using this data and that of the main Rogowski coil, a total resistance and a total inductance of the thruster was determined to be 0.009 Ω and $4.5X10^{-8}$ Henry, respectively. Then, using a simple circuit analysis, the current sheet was modeled as a damped sine wave based on the experimentally determined thruster impedance, for use in the MACH2 computer simulation. In the future, a straight comparison of the electron number density from MACH2 will be made once new developments of MACH2 are completed.

Recommendations for future development of both the MACH2 and GEMS computer simulations are provided in the final chapter of this thesis.

Table of Contents

Chapter 1: Introduction 1
Chapter 2: Background 4
a. History of Electric Propulsion Devices 4
b. How Electric Propulsion Works 5
i. Electrothermal Propulsion 7
ii. Electrostatic Propulsion 8
iii. Electromagnetic Propulsion 10
c. Pulsed Plasma Thrusters 11
i. Operation 13
ii. Problems 13
iii. Past and Future 15
d. Electric Propulsion in Use Today 15
Chapter 3: Approach 19
a. Thruster and Setup 19
b. Diagnostics 25
c. B-Dot Probes 29
d. MACH2 32
Chapter 4: Theory 33
a. Thruster Operation 33
b. MHD Assumptions 34
c. B-Dot Probes 36
d. Circuit Analysis 39
Chapter 5: Data and Results 43
a. Data 43
i. B-Dot Probes 43
ii. Rogowski Coils 45
iii. Laser Interferometer 46
b. Data Analysis 46
i. Thruster Current 53
ii. Thruster Current Sheet 56
iii. Laser Interferometer Data Analysis 67
Chapter 6: Conclusion 70
a. Summary 70
b. Recommendations 71
References/Bibliography 73
Appendix A 76
Appendix B 80
Vita 92

List of Tables

Table 1: Benefits of using a PPT 14

Table 2: Project Requirements for the HiPEP Project 18

Table 3: JIMO Project Requirements 18

Table 4: B-Dot Integration Constants 39

Table 5: Total Resistance and Inductance Constants for Thruster Circuit with Plasma Present 56

Table 6: Table Showing Times When Current Passes B-Dot Probes (Nov. 29, 2005) 59

Table 7: B-Dot Peak Analysis 83

List of Figures

Figure 1: Typical EP System [8] 5
Figure 2: Resistojet [18] 8
Figure 3: Arcjet [18] 9
Figure 4: Schematics of an Ion Thruster [6] 10
Figure 5: Schematics of FEEP Thruster [6] 11
Figure 6: Schematics of an MPD Thruster [6] 12
Figure 7: Schematics of a Hall Thruster [6] 12
Figure 8: Schematics of an APPT [6] 14
Figure 9: EO-1 APPT Thruster [5] 16
Figure 10: Main Capacitor 20
Figure 11: "Doghouse" Capacitor and Spark Gap 20
Figure 12: Power Supplies 21
Figure 13: Thruster Schematic [30] 22
Figure 14: 2 in. Inner and 4 in. Outer Electrodes with Axial Slots 22
Figure 15: Gold Sputter Fuse Ring 23
Figure 16: Non-Uniform Plasma Discharge [13] 23
Figure 17: New and Old Trigger Hookup [2] 24
Figure 18: Vacuum Pump 26
Figure 19: Camera Setup 27
Figure 20: Laser Power Supply and Optics for Interferometer 27
Figure 21: One End of Fiber Optic Laser Interferometer Located at Thruster Exit 28
Figure 22: Two Oscilloscopes 28
Figure 23: One of Two Data Collectors 30
Figure 24: B-Dot Probes in Place on Thruster 30
Figure 25: B-Dot Probe Locations [13] 31
Figure 26: Forces in Thruster 33

Figure 27: 3-D Thruster Diagram with Plasma Discharge 34
Figure 28: Thruster Set-Up with Current Flow 35
Figure 29: Thruster with the Fuse Removed for Calibration Purposes 37
Figure 30: Back of Thruster with Plate Bolted to it for Calibration Purposes 38
Figure 31: Front of Thruster Setup for Calibration 38
Figure 32: Transient Circuit 41
Figure 33: Raw Signal from B-Dot probe 1 Upstream of the Plasma Flow (Sept. 20, 2005) 44
Figure 34: B-Dot Probe Locations 44
Figure 35: Raw Data from the Main and Trigger Rogowski Coils (Nov. 29, 2005) 46
Figure 36: Raw Data from the Interferometer (Nov. 29, 2005) 47
Figure 37: Raw B-Dot Data with Median Filters (Sept. 7, 2005) 48
Figure 38: Integrated B-Dot Data from the Raw Data in Figure 33 (Sept. 20, 2005) 50
Figure 39: Integrated Rogowski Coil Data from the Raw Data in Figure 35 (Nov. 29, 2005) 50
Figure 40: Shifted B-Dot 1 Data (Sept. 20, 2005) 53
Figure 41: Comparison of B-Dot Probe 1 and Theory (without Plasma) (Oct. 22, 2005) 54
Figure 42: Comparison between B-Dot 1 and Theory (with Plasma) (Nov. 29, 2005) 55
Figure 43: Comparison between B-Dot 2 and Theory (with Plasma) (Nov. 29, 2005) 56
Figure 44: Integrated Data from B-Dot 13 (Sept. 7, 2005) 58
Figure 45: Peak 1 to Peak 2 Comparison for Sets 1-3 (Nov. 29, 2005) 60
Figure 46: Azimuthal Position of the thruster vs. Time (Nov. 29, 2005) 61
Figure 47: Current comparison for Set 2 (Nov. 29, 2005) 62
Figure 48: Velocity Data for Set 3 (Nov. 29, 2005) 63
Figure 49: Velocity for all Three Sets (Nov. 29, 2005) 64
Figure 50: Picture of Thruster Firing (9/20/05). 65
Figure 51: Comparison of Integrated B-Dot 1 Data for Multiple Thruster Runs 66
Figure 52: Current Sheet Velocity for Multiple Thruster Runs 66
Figure 53: Interferometer Phase Shift Data (July 1 , 2005) 69

Figure 54: Electron Number Density taken from Interferometer (July 1, 2005) 69
Figure 55: Set 1 B-Dot Integration 82
Figure 56: Set 2 B-Dot Integration 82
Figure 57: Set 3 B-Dot Integration 83
Figure 58: B-Dot Peak Position vs. Time (for Peaks 1 & 2) 84
Figure 59: B-Dot Axial Position vs. Time (Peak 1) 84
Figure 60: Time vs. B-Dot Peak # (Set 1) 85
Figure 61: B-Dot Peak Analysis (Set 1) 85
Figure 62: B-Dot Peak Analysis (Set 2) 86
Figure 63: B-Dot Peak Analysis (Set 3) 86
Figure 64: Magnetic Field Velocity vs. Time (B-Dot) 87
Figure 65: Raw Rogowski Coil Data 87
Figure 66: Integrated Rogowski Coil Data 88
Figure 67: Integrated B-Dot Data Compared against Integrated Rogowski Coil Data 88
Figure 68: Normalized Rogowski Data 89
Figure 69: Circuit Analysis Compared against Integrated B-Dot Data 89
Figure 70: Raw Interferometer Data 90
Figure 71: Interferometer Phase Shift Data 90
Figure 72: Interferometer Electron Number Density 91

Nomenclature

A – area
B – magnetic flux density
C – capacitance
cc – cross correlation constant
c – integration constant
D – electric displacement
d – time delay
dl – change in circuit length
E – electric field intensity
e – induced emf
f_B – body force
H – magnetic field intensity
h – time step (t_2-t_1)
I – current
i_r – unit vector pointed in the direction of increasing r, current
j – electric current density
L – impedance, inductance
l – circuit length
m – mass
mx – mean average of x
my – mean average of y
N – number of single turns
n – unit vector
P – any point in a complete circuit
R – resistance
r – distance
s – closed path
t – time
V – voltage

Greek
α – angle between **B** and the normal, constant
θ – the angle between dl and r
μ_o – permeability of free space [$4\pi*10^{-7}$ Weber/amp-m]
φ – number of magnetic flux lines
η – charge density
ω – constant
ω_a – analog cutoff frequency
ζ – mass fraction
ξ – truncated error term

Chapter 1: Introduction

To effectively use electric propulsion (EP) thrusters, reliable electrical power must be available in space vehicles. To date, solar panels on space vehicles have provided a maximum of tens of kilowatts for EP devices. As a result, EP thrusters have been widely developed for this power range. Other power sources have been proposed and developed with rather limited use in space applications; these space powered systems include Radioisotope Thermal Generators (RTG) and nuclear fission reactor (NFR). RTGs have been successfully employed to provide electrical power (up to ~300 Watts) [1] for space exploration probes but have never been used to power EP devices. NFRs could provide power at the MW level, but have yet to be developed for space applications, mostly do to political and environmental restrictions. In recent years, NASA's new space initiative proposed by President Bush has generated a lot of interest in high power EP (HiPEP) devices. High power-density nuclear electric power supplies are expected to be available for use in space and will provide the needed power for HiPEP devices at the megawatt power level.

In order to further develop any EP device, much less high power ones, a valid computer simulation tool is required to help in development. Many computer simulation codes exist for low power EP devices, but few are available for higher power EP devices of interest. Magnetoplasmadynamic (MPD) thrusters and pulsed plasma accelerators (PPA) or pulsed plasma thrusters (PPT), are believed to be well suited for high power operation because they can offer high power densities. Modeling PPAs is very difficult with conventional magnetohydrodynamic (MHD) codes because the assumption of an insignificant time derivative of displacement current (in Ampere's Law) is inherent in MHD modeling formulations. Because PPAs contain vacuum regions as well as regions of dense plasma, usual MHD assumptions do not apply. This will be discussed in greater detail in Chapter 4. To properly model these devices, the full set of Maxwell's Equations must be solved. Traditionally, MHD codes were utilized for EP thrusters because the propagation of the EM fields by diffusion could be modeled as a second order equation in magnetic induction that eliminates the need to store values for the electric field throughout the computational

domain. Thus, less computer memory was required, greatly reducing costs at a time when computer RAM was extremely expensive. Today, inexpensive computer memory and modern computational fluid dynamics (CFD) algorithms have made the solution of the full set of Maxwell's Equations practical.

The University of Tennessee Space Institute (UTSI) has been assigned an Arnold Engineering Development Center (AEDC) task order to carry out detailed diagnostics of a laboratory prototype EP thruster and utilize the resulting data to validate a complex, three-dimensional electromagnetic code based on Dr. Charles Merkle's General Equation and Mesh Solver (GEMS) CFD code [2]. The laboratory prototype HiPEP thruster being utilized is classified as a Pulsed Plasma Accelerator (PPA). The MACH2 [3-5] code was used in early thruster design and initial thruster simulations. Mr. Bob Rhodes at UTSI used MACH2 to design the fuse for the thruster. MACH2 has also been used to simulate a variety of plasma devices at UTSI, including electrothermal guns, pulsed plasma thrusters, and cableguns. In addition to the constraints associated with the MHD assumptions, MACH2 has a couple of limitations; it is only capable of simulating 2-D systems, and it utilizes outdated algorithms. The 3-D GEMS code will alleviate these limitations, but MACH2 was necessary in setting up the thruster and conducting initial simulation runs.

Interferometric and photographic measurements were used in the present experiment to characterize the time evolution of the plasma in the thruster. A single-beam, heterodyne laser interferometer was used to measure the time dependent line of site electron number density at the exit of the thruster. Rogowski coils measure the time evolution of the current in the trigger and main capacitor circuits. Thirteen B-dot (magnetic field flux coil) probes were installed on the outer electrode of the thruster. These probes measured the time evolution of the current sheet as it travels down the length of the thruster during firing.

This thesis describes an experimental program that used the 13 B-dot probes to gather spatially and temporally resolved data on the time evolution of the magnetic field strength and current of a PPA during firings, and the acquired data was archived for future comparisons with theoretical results from MACH2 simulations. Along with B-Dot probes, Rogowski coil data and laser interferometer data were analyzed. Tasks completed for this thesis include collecting and analyzing the B-Dot probe data, determining the plasma exit velocity, resistance, inductance, and overall plasmadynamic trends in the

thruster. The analysis of the B-Dot probe data and the interferometer data provided insight into the overall thruster operation and will guide future code improvements. This thesis will conclude with an assessment of the thruster, and recommendations for further diagnostics.

Chapter 2: Background

a. History of Electric Propulsion Devices

While only recently becoming popular, the concept of electric propulsion (EP) has been around since the early 1900's. Robert Goddard first conceptualized EP in 1906 [6]. He tested electric gas discharge tubes from which he formed the basic concepts of EP. However, it was not until the 1950's that development of practical EP devices started. Dr. Ernst Stuhlinger laid out a basic tutorial assessment of EP in his book entitled "Ion Propulsion for Space Flight" [6]. The United States, Soviet Union, Europe, and Japan all began development of EP devices later in that decade [7]. The scientists and engineers from these countries drew from past experiences of other electrostatic devices such as arc-heated wind tunnels, welding systems, and rail guns to devise these initial devices [6]. The engineers saw EP as an alternative to chemical propulsion for high power missions because they were able to produce very large Δv's in theory. However, EP was slow to develop in practice because of the lack of the on-board high power sources needed, the same reason HiPEP device are not widely used today [8]. Due to this power constraint, EP found a niche in low-power applications. EP saw its first space application a decade later in 1964 aboard the Soviet Zond-2 spacecraft. It used six ablative pulsed plasma thrusters (APPT) for sun pointing control [6].

Utilization of EP devices continued into the 1970's with the use of a Hall thruster on Soviet satellites and the continued use of pulsed plasma thrusters (PPT) on Soviet and American satellites [8]. Early on, the Americans were less likely to take the risk of using EP devices than were the Soviets. As the 1980's progressed interest in the scientific community on EP thrusters increased. Resistojets became a common option for station keeping and attitude-control on satellites [6]. Arcjets were used a decade later for north-south station keeping (NSSK) on commercial satellites in geosynchronous orbit (GEO) [6]. In 1994, ion thrusters were also used for NSSK and in 1996 they were used to power NASA's Deep Space One (DS-1) mission [6]. Ion thrusters are still among the most successful and well publicized EP devices used by many nations. Other EP-utilization missions include EO-1, ST, CNSR, and the Mars Sample return mission [7]. Increased support for EP has continued into the 21st century with the NSTAR, JIMO,

HiPEP, and Prometheus projects funded by NASA. EP devices have grown in number from use on a few spacecraft in the 1960's to use on tens of spacecraft in the 1970's and 1980's to more than one hundred used in the 1990's [5]. But in order for EP to become more versatile, high power levels (>100 KW) must be obtained. This will allow them to be used on the energetic missions, with large cargo and piloted payloads to other planets as well as proposed human and robotic interplanetary missions [6].

b. How Electric Propulsion Works

Independent of which type of EP device you consider, they all consist of four major components (Figure 1). These components are: power processing unit or PPU (which takes raw power from the power supply and converts it to the waveform and amount required by the thruster); a power system (supplies power to a PPU); the thruster itself; and the propellant tanks. The PPU is the most complex sub-system on the EP devices and is usually the most difficult to develop [6].

EP devices come in many shapes and sizes. They can be pulsed or steady; gas acceleration can be by thermal, electrostatic, electromagnetic, or hybrid propulsion; and propellant can be a noble gas, a chemical monopropellant, or gases from a burning or thermally decomposing solid [8]. Even with all these different variations, EP devices can be sorted into three different categories [8]:

1. Electrothermal thruster– the propellant is electrically heated, then expanded through a nozzle, similar to liquid and solid rockets

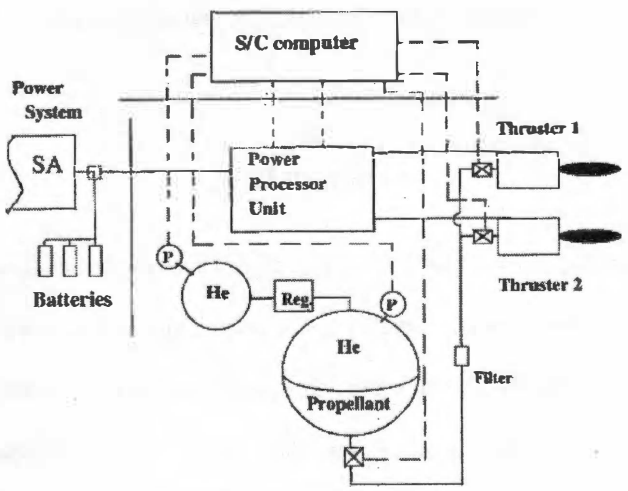


Figure 1: Typical EP System [8]

2. Electrostatic thruster – ionized propellant particles are created, accelerated through an electric field, then de-ionized before leaving the spacecraft
3. Electromagnetic thruster – current is driven through propellant plasma and interacts with an internal or external magnetic field to provide a stream-wise directed body force that accelerates the plasma

Although each category utilizes a different mechanism to accelerate the propellant, all add energy to a working fluid from an electrical source [8]; hence the reference to the name electric propulsion.

EP has strengths and weaknesses that make it attractive for some missions and impractical for others. As stated before, the main reason EP devices were first developed was because they were theoretically capable of producing very large Δv's, much larger than today's chemical rockets. A Δv associated with an orbit change represents the change in vehicle or spacecraft velocity needed to transfer from one orbit to another, or to break from an orbit. EP devices produce very large exhaust velocities, making missions from low Earth orbit to the moon fuel efficient, and human missions to Mars plausible, because of the large Δv's and Isp provided. Some EP devices are also easily throttled, and thus, are capable of producing a wide range of exhaust velocities. In addition, EP devices can be turned on and off again multiple times, a characteristic that some liquid rockets and no solid rockets are capable of. This makes EP a very attractive choice for near earth applications, such as attitude control, station keeping, drag reduction, and modest orbit-changing functions [6], the function for which most EP devices are used today. EP thrusters are also capable of a wide range of mass fraction, ζ, given by Equation 1, where m_p and m_o are the

$$\zeta = \frac{m_p}{m_o}$$

Equation 1

mass of the propellant and initial mass respectively. This allows such devices to be tailored to different missions. Lastly, EP devices often use chemically passive propellants, which generally can easily be handled and stored, unlike some of the complex and dangerous liquid and solid propellants.

With all these advantages over chemical propulsion, EP still has many drawbacks that keep it from being used as a primary source of propulsion for many space applications. First, EP development is far less

mature compared to chemical propulsion. Only in the last two decades have major advancements in the EP field occurred, while chemical rockets have had major funding since before the establishment of NASA in the late 1950's. Since EP is so underdeveloped, these devices have not been used extensively [6]. Therefore, it is still unknown how some of the EP devices will perform when used in space over long periods of time, making potential customers less likely to take risks on these emerging technologies. In addition, the EP thruster is only as powerful as its on-board power source. These power sources tend to be very complex and sophisticated and are hard to develop and maintain.

The primary reason chemical propulsion is favored over EP is due to the fact that today's EP devices provide extremely low thrust and have low thrust densities (thrust per unit area) when compared with chemical rockets [6]. In addition, the low thrust associated with EP thrusters precludes their use in applications that require rapid maneuvering or relatively short orbital transit times (i.e. some missions to Mars). EP devices cannot be used to launch payloads from objects with significant gravitational pull. One such case would be an earth launch; chemical rockets are still needed to put EP thrusters into orbit. The low thrust densities associated with EP also force the trajectories of the spacecraft to become a lot more complex. EP driven spacecraft tend to have to take the long way to get to their destination, but in theory the spacecraft gets there cheaper and with less risk involved [6].

i. Electrothermal Propulsion

As mentioned before, EP device are divided into three different categories. The first to be described is electrothermal propulsion. Electrothermal propulsion is similar to chemical propulsion in that a heated propellant is expanded through a nozzle to convert thermal energy into kinetic energy, thus providing thrust [6]. The difference is that chemical propulsion utilizes chemical reactions to provide the energy; electrothermal propulsion devices electrically heat propellant [6] with electric energy.

According to Jahn and Choueiri [6], electrothermal propulsion can be divided into three sub-categories:

1. *Resistojets - wherein heat is transferred to the propellant from some solid surface, such as the chamber wall or heater coil (*Figure 2*)*

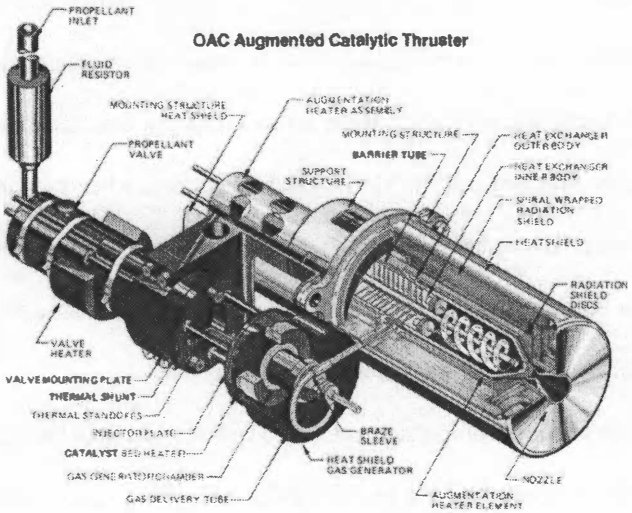


Figure 2: Resistojet [18]

2. *Arcjets - wherein the propellant is heated by an electric arc driven through it (*Figure 3*)*
3. *Inductively and radiatively heated devices – wherein some form of electrodeless discharge or high-frequency radiation heats the flow*

While resistojets and arcjets have been used for early in-space propulsion and are still used today, the inductively and radiatively heated devices have yet to be used in space. The main drawback with electrothermal propulsion is that the specific impulses provided by the thrusters are limited to the thermal energy that can be input to the propellant and the expansion process through the nozzle [6]. This is a similar drawback to chemical propulsion, in that the maximum thrust is limited by the amount of chemical energy that can be converted to thermal energy before expansion through the nozzle. This is not the case with the other two forms of EP that in theory, are only limited by the power supply.

ii. Electrostatic Propulsion

In another use of electric energy to generate propulsive thrust one can directly accelerate the propellant by an external electric body force provided by an applied electric field. This is referred to as electrostatic propulsion [6]. The most widely used form of electrostatic propulsion is based on accelerating ions or charged particles. An ion thruster works when a beam of charged particles is accelerated by a

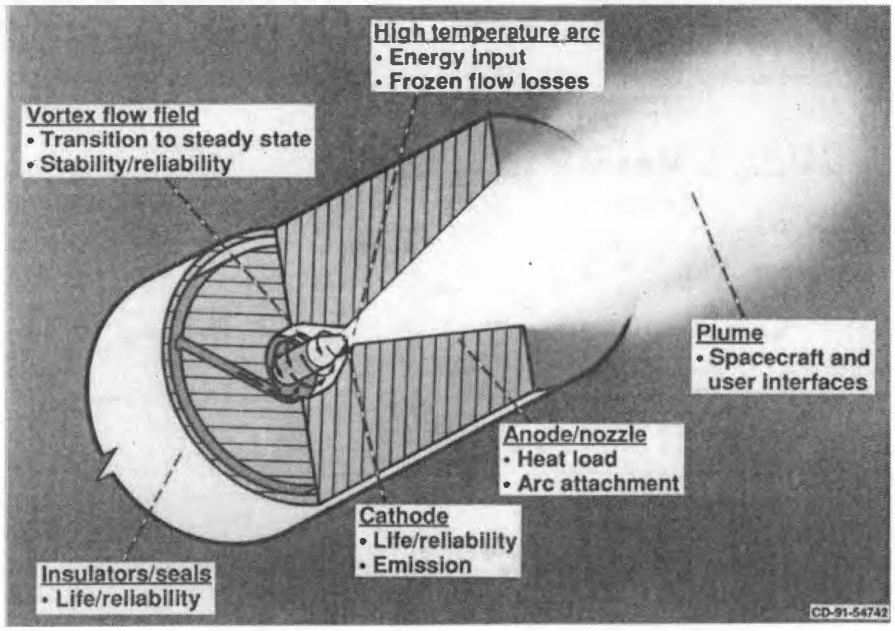


Figure 3: Arcjet [18]

suitable electric field and subsequently neutralized by an equal flux of free electrons downstream of the acceleration grid (Figure 4) [6]. Ion thrusters are one of the more complex forms of EP but are also the most developed of all EP devices [6]. The complexity of Ion thrusters comes from the fact that they are so difficult to optimize for a given mission. One must conduct a trade-off study to include, but not be limited to, the exhaust speed, thrust density, efficiency, and power system specific mass [6]. Ion thrusters are so attractive because they have been tested over long periods of time (>20,000 hrs), have high efficiencies (65%), and have high exhaust velocities (30,000 m/s) compared to other forms of EP [6]. Unfortunately, there are also negative characteristics associated with these devices. Ion thrusters, like all EP devices have low thrust densities, a very complex control system, and high voltage requirements. However, ion thrusters have been used extensively. The DS-1 mission [6] was one of the more well known missions that utilized ion propulsion. Flown in 1998 the mission included a rendezvous with the asteroid Braille and the DAWN asteroid [9].

Another type of electrostatic propulsion, although less developed, is field emission electric propulsion (FEEP). FEEP devices have been developed in Europe since the 1970's and they utilize a high electric field concentrated at the lips of a capillary slot to allow for a direct ionization of a metal in liquid

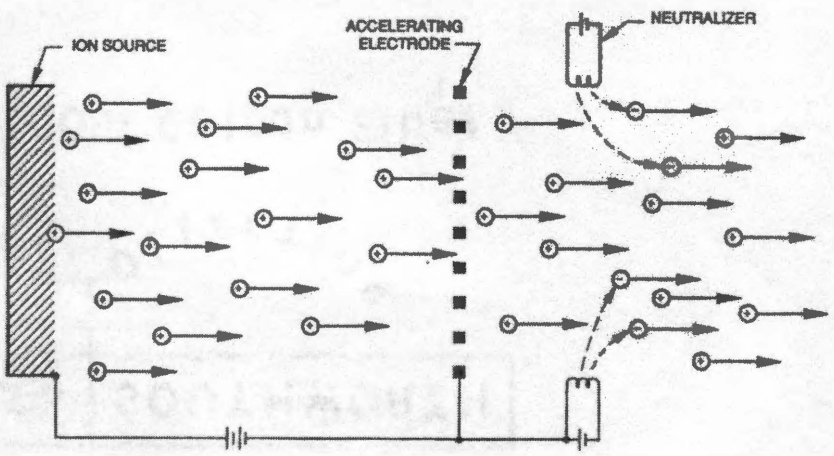


Figure 4: Schematics of an Ion Thruster [6]

form [6]. The resulting ions can be accelerated electrostatically to very high velocities (Figure 5). Although no FEEP devices have been flown in space, a number of missions are already planned in the U.S. and Europe to utilize FEEP [6]. The last type of electrostatic propulsion thruster is the colloidal thruster. It is similar to FEEP but "*non-metallic liquids are used and sub-micron charged particles (colloids) are produced and accelerated*" [6] instead of ions. This thruster was developed in the 1960's but is still an EP option for Russia and the U.S.

iii. Electromagnetic Propulsion

Electromagnetic Propulsion thrusters are the last of the three types of EP to be discussed and, out of the three categories of EP, will likely have the biggest impact on space propulsion in the near future. Electromagnetic propulsion is able to produce higher exhaust velocities than electrothermal propulsion [6] and is capable of producing larger thrust densities than electrostatic propulsion. But inherently these advantages over the other two types of EP make the system more complex to develop and harder to model. Also, very high energy sources for electric power are required. Jahn and Choueiri [6] define electromagnetic propulsion as:

> *"where some electrically conducting fluid, usually a highly ionized gas is subjected to an electric field* ***E*** *and a magnetic field* ***B****, perpendicular to each other and to the fluid velocity* ***u****. The*

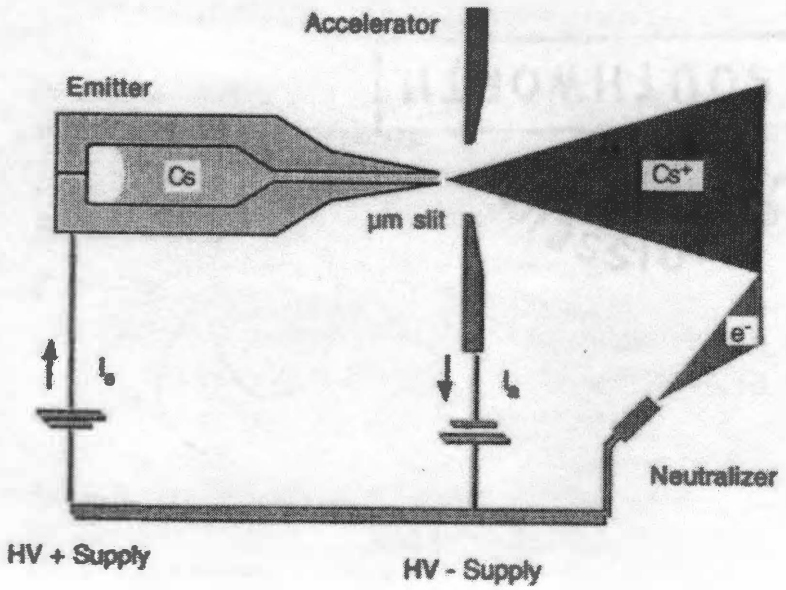


Figure 5: Schematics of FEEP Thruster [6]

*current density **j** driven by the electric field interacts with **B** to provide a streamwise body force **f** = **j** x **B** that accelerates the fluid along the channel".*

Electromagnetic propulsion is possible in many different variations: the applied field current may be steady, pulsed or operate at variable frequencies; the magnetic field may be applied externally or induced by the current flow; and a wide range of propellants may be used [6]. Of these variations the three most popular and consequently most developed plasma thrusters are the magnetoplasmadynamic (MPD) thruster (Figure 6), the Hall thruster (Figure 7), and the pulsed plasma thruster (PPT).

c. Pulsed Plasma Thrusters

PPTs are similar to the pulsed plasma accelerator (PPA) that is the subject of this thesis. PPTs were the first EP device to be successfully used in space [6]. The United States first used a PPT on the LES- 6 satellite in the 1960's [8]. The following sections discuss how they operate, problems that arise when using PPTs, and the future kinds of missions that are being planned using PPTs.

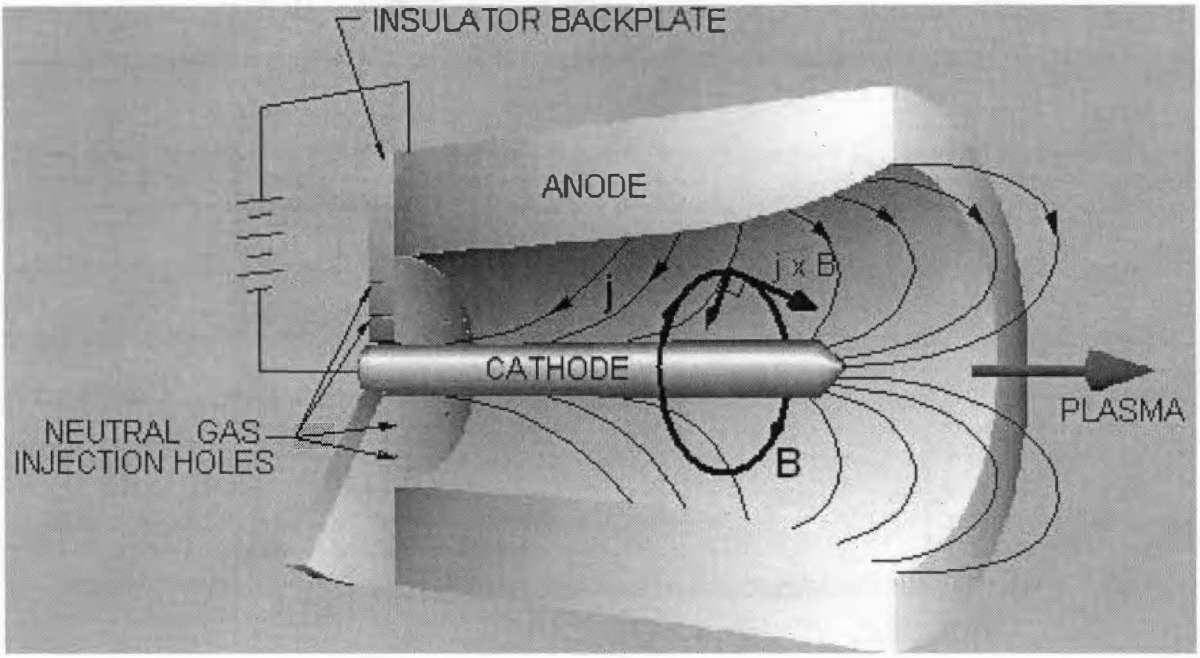


Figure 6: Schematics of an MPD Thruster [6]

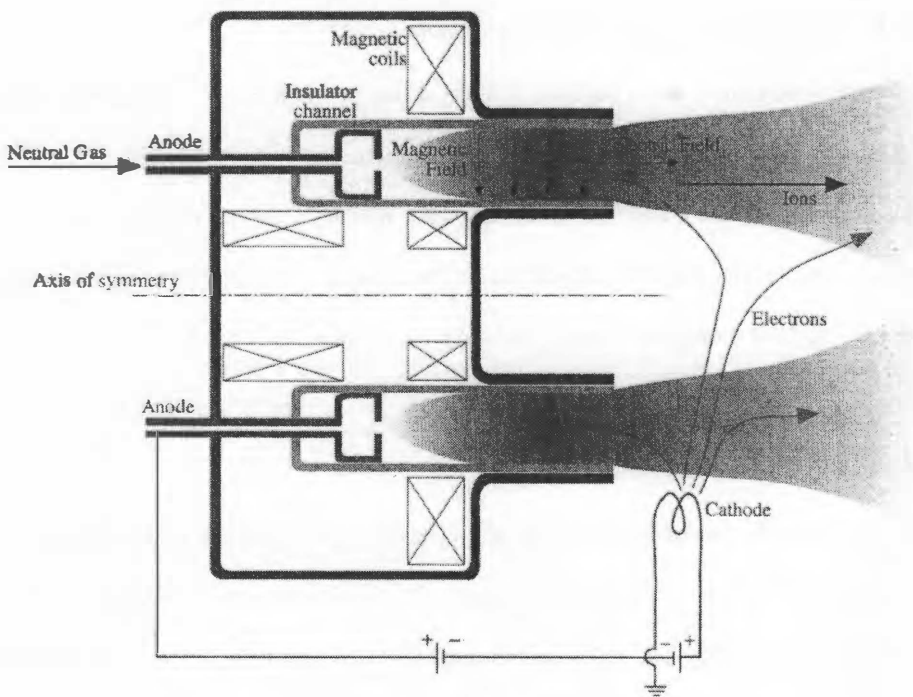


Figure 7: Schematics of a Hall Thruster [6]

i. Operation

PPTs differ from other EP devices by operating in short pulses, usually ~10 μs, and they use a solid propellant, mostly commonly Teflon® [8]. The energy for the microburst is usually stored in a capacitor bank or an inductor coil which is rapidly discharged into the electrode [6]. One type of PPT that has been extensively used in space is the ablative pulsed plasma thruster (APPT) (Figure 8). APPT is the simplest and most used form of PPT in space. The APPT operates by charging a capacitor to 1-2 kV and rapidly discharging the capacitor through a spark plug type of device. This supplies an arc across the face of the propellant [8]. The propellant is a spring fed polymer block; this eliminates the need for a complex mass storage and control system that would be needed for a gas-fed system [6]. Teflon® is very easy and safe to handle, reducing the cost of preparation. During operation the propellant face is ablated by arc pulses; then the ablated material is accelerated by a combination of thermal expansion and self-field electromagnetic forces [6]. The pulse of current (~10 kA) produces a self-induced magnetic pressure almost equal to the gas kinetic pressure. Both pressure gradients accelerate the propellant to speeds at which the kinetic energy equals the ionization energy, which produces a range of specific impulses between 1000-1500 s [8]. For a summary of the benefits refer to Table 1.

ii. Problems

PPTs tend to be used on small and micro satellites for attitude control. This is because the problems related with using a PPT do not adversely effect operation on smaller scales as much as for larger scale operations [6]. PPTs tend to have very low efficiency, 8-13%, and the thrusters have a very large mass compared to the propellant mass (8 times as large on the LES-8 and LES-9 satellites) [8]. For the smaller satellites these problems are tolerable and do not effect the overall performance of the mission. For longer missions, use of a PPT would require a complex feeding system to be able to handle the increased propellant mass [8]. In addition to these problems, the thruster interacts negatively with the spacecraft as well. These negative interactions include plume effects and thermal effects [8]. The plume effects are related to the accumulation of polymer products on the spacecraft that are a result of the propellant ablation

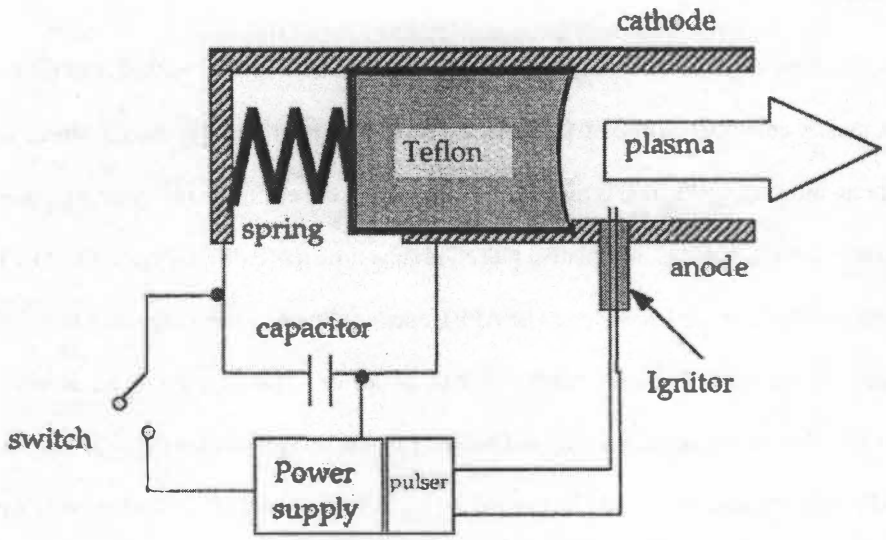


Figure 8: Schematics of an APPT [6]

Table 1: Benefits of using a PPT

Positive Aspects
The propellant feed system and thruster are housed in a single compact unit
Uses a non-toxic propellant
Precision operation through micro pulses
Tunable by varying pulses
Virtually unlimited start-stop capabilities
Multiple in space applications
Proven space capabilities and reliable

[8]. Thermal effects include the heat generated by the thruster, which can damage sensitive satellite components. These interactions are not just associated with PPTs but occur in most EP thrusters.

iii. Past and Future

While PPTs have been used since the 1960's on U.S. and Soviet satellites, it was not until the mid 1990's that research and development of the thruster was revisited on a larger scale. This was primarily for the advent of smaller, micro-satellites for which the PPT can produce small, precise impulses for attitude control on power limited satellites [6]. Micro PPTs have been successfully used in space for two decades [10]. For low average-power satellites they have performed well and are being considered for future missions involving small type satellites [10].

Since PPTs have been readily used in the past and are attractive for smaller satellites, a lot of work has gone into PPT development. Some suggestions of solutions to the problems mentioned earlier are being addressed by both industry and universities. Efficiency can be increased by pulse tailoring, by nozzle recovery of more of the thermal energy, and by operating at higher instantaneous power [8]. The thruster system mass can be reduced by redesign and improvements to the capacitor and electronic technologies [8]. With some advances in the designs, it is believed that PPTs can make the jump from low powered satellite to high-power satellite control and primary thrust responsibilities.

d. Electric Propulsion in Use Today

EP has had limited use in space for a variety of missions: NSSK orbit upkeep, orbit raising, drag compensation, deployment to high LEO orbit from low delivery orbits, total or partial LEO-GEO transfer, deorbiting of spacecraft at end-of-life, orbit phase changes and primary propulsion for a spacecraft or satellite [8]. NASA has not used EP as extensively as Russia but it is committed to development of future thrusters. Currently NASA's activities in EP include: development of gridded ion thruster technology, Hall thruster technology, PPT technology, and very high power EP technology as well as system technology that supports practical implementation of the concepts [9]. As of July 2004, NASA had one active satellite, Earth Observing-1 that utilized a PPT (Figure 9), which continues to operate successfully, and one new

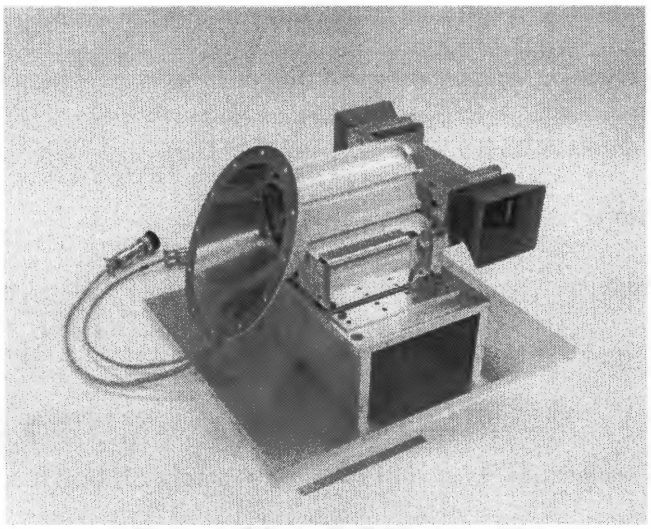


Figure 9: EO-1 APPT Thruster [5]

satellite in development that utilizes EP. NASA is also supporting, through the European Space Agency, another EP spacecraft, SMART 2. This satellite will use a set of colloidal thrusters to position the satellite [9].

Currently NASA has some major projects that support EP; these include Project Prometheus, Energetic Projects, Jupiter Icy Moons Orbiter (JIMO), and High Power Electric Propulsion (HiPEP) just to name a few [9]. Project Prometheus, which is NASA's largest supporter of EP, will develop an EP system that will use a space nuclear fission power system. This will allow for more sophisticated remote sensing to be utilized, for a greater launch window, and for greater spacecraft maneuverability [9]. The main spacecraft design in development is for a 100 kW, nuclear-electric-powered flagship science mission, but at the same time, other ideas are being considered. The two primary technologies in development are for a high powered/high specific impulse gridded ion thruster and improvements to a NASA designed Hall thruster [9].

Although not as well known as Project Prometheus, NASA's Energetics Project is set up to make advances in the areas of advanced power and advanced propulsion. This year it will be replaced by a set of projects, but some of the highlights of the project include:

- Studies conducted in all areas of EP

- Specifically in the area of PPTs, NASA is striving to produce lightweight, multi-thruster PPT systems with high-efficiency, single-axis systems, and to have a better understanding of the physics present in PPT plasmas
- The Energetics Projects plan for PPT to be used for attitude control and translation propulsion, momentum management, drag makeup, orbit raising, and large space structure dynamic control [9]

In 2002, NASA's Office of Space Science released a NASA Research Announcement (NRA) for the development of high power electric propulsion for near term nuclear systems, specifically a high power, high specific impulse, nuclear electric propulsion (NEP) system [11]. From this the HiPEP project was formed. The aim of this project is to develop and demonstrate ion thruster technology capable of satisfying advanced exploration propulsion concepts (Table 2). One such mission to come from this project is the JIMO mission (Table 3). NASA is also developing technologies for high power/high specific impulse gridded ion propulsion system concepts. They are also creating long-life components and modeling, high voltage isolators, high power PPU options, and radiation hardened thruster components and materials [12]. In addition to the high-powered EP missions discussed in this section, NASA is also pursuing high-powered electromagnetic accelerators for deep space missions, including MPD thrusters and PPAs. EP is starting to be of much greater current interest because EP can enable missions to Jupiter's Moons and future human missions to Mars. With future development and support the possibilities for EP use in space are nearly endless.

Table 2: Project Requirements for the HiPEP Project

Requirements
Thrust Power Level 100 kW with growth to 250 kW
ISP of 6000-9000 s
Total Thrust Efficiency >65%
Specific Mass of 30 kg/kW
Propellant Throughput >50kg/kW

Table 3: JIMO Project Requirements

Requirements
Thrust Power Level 20-50 kW
Vehicle Power Level 100-250 kW
Specific Impulse 6000-9000 s
Efficiency >65%
Individual Thruster Propellant Throughput >100 kg/kW
Thrust Mass Target <3 kg/KW
6-10 year operation life
Radiations Tolerance
Technology Maturity

Chapter 3: Approach

The thruster used in this experiment is being developed under a project being funded by the Air Force at AEDC. The project title is Nuclear Fission Electrical Power and Propulsion, Task 03-01 and Contract Number F40600-00-D-0001 [2]. The overall goal of the project is to develop a 3D computational fluid dynamics (CFD) and electromagnetics code that can accurately predict the physical phenomena that occur in the thruster. An example of such a code is the MACH2 MHD code [5]. MACH2 was utilized to simulate the PPA flow and guide the development of the laboratory prototype thruster, including the fuse development. Unfortunately, the MACH2 code lacks the physics necessary to properly model a pulsed plasma thruster (this will be discussed in greater detail in Chapter 4), so, a 3-D electromagnetic version of the GEMS code is being developed that uses modern computational methods [2]. A laboratory thruster, described below in detail, is being used to provide experimental data for code validation. The thruster is designed to operate with only enough fuel for a single firing, or pulse, and thus would is not actually be a thruster that would be used in space. However, this particular thruster design provides good diagnostic capabilities, providing performance that can be monitored and studied in great detail. The detailed data obtained from this experiment is necessary for proper validation of the GEMS code.

a. Thruster and Setup

The experimental thruster uses an electric pulse to explode a thin metallic foil that forms the plasma that acts as the thruster propellant. The electric current generates a self-induced magnetic field, and a Lorenz force is produced that both compresses and pushes the plasma down the length of the thruster. The theory and design of the PPT is provided later in Chapter 4. One 17.5 μF, 40 kV capacitor (Figure 10), on loan from Marshall Space Flight Center, is used to store energy for the current pulse that is delivered to the thruster. A second power source is used to explode the fuel "foil" to generate the propellant plasma. This power source is referred to as the "doghouse" capacitor (Figure 11) and is comprised of a 25 kV capacitor with a triggered spark gap that allows the controller to discharge the capacitor at a precise time. There are two DC power supplies (Figure 12) that are used to charge the main capacitor and doghouse

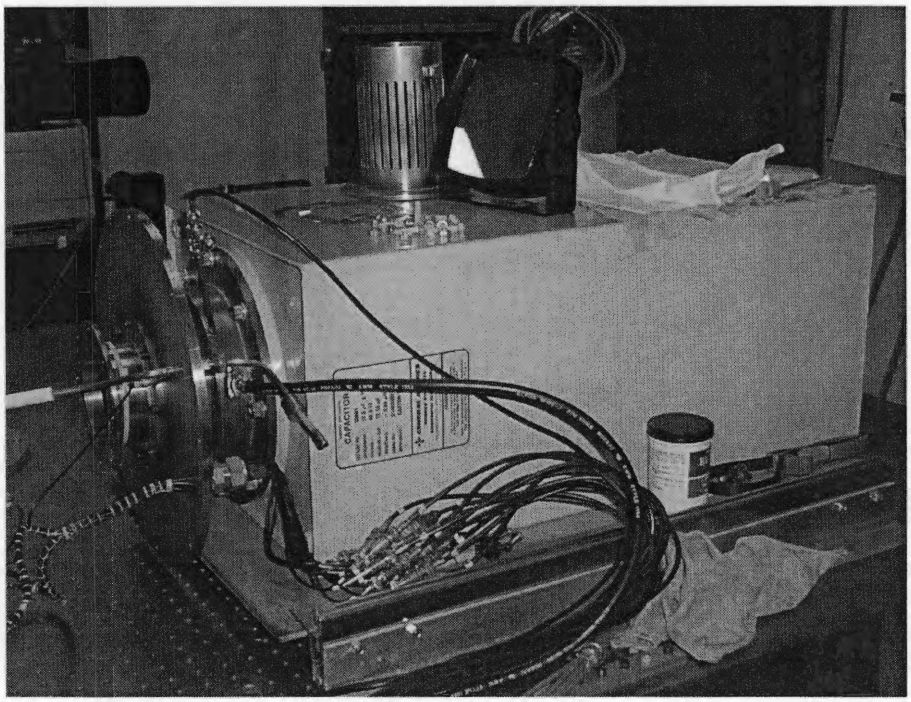


Figure 10: Main Capacitor

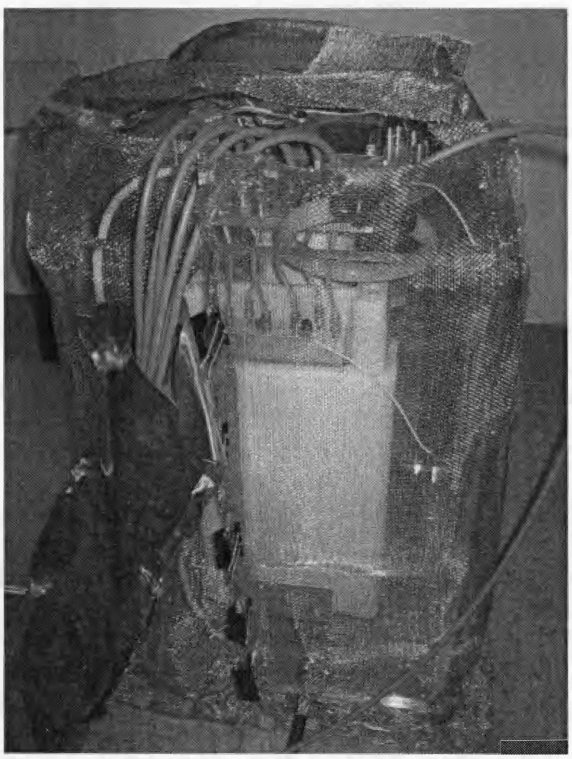


Figure 11: "Doghouse" Capacitor and Spark Gap

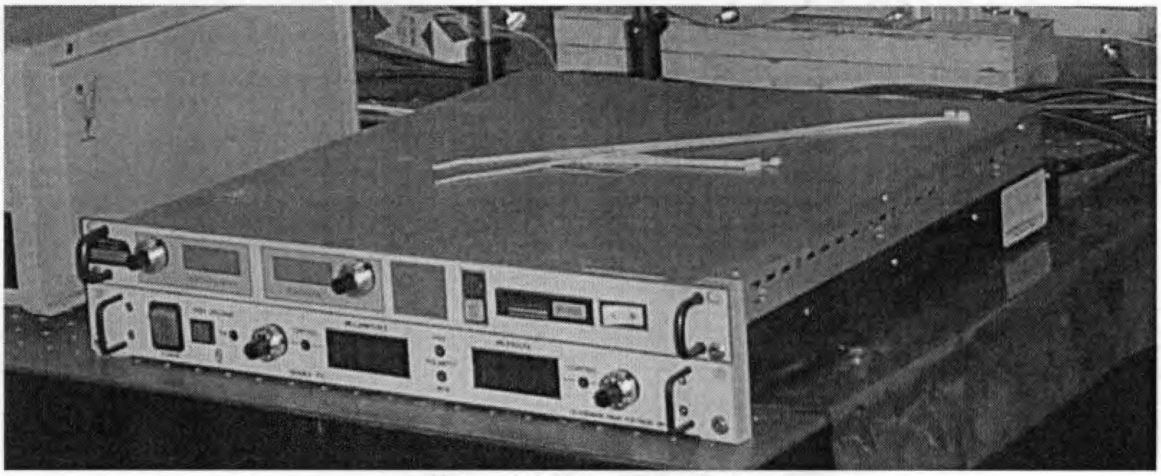


Figure 12: Power Supplies

capacitor. The spark gap that triggers the doghouse power supply is initiated by one central control, which the operator uses to initiate the thruster firing. The central control is also synchronized to initiate the data acquisition system. The PPT design is shown schematically in Figure 13. It is cylindrical in cross-section with a 1 in annulus between the inner and outer electrodes. The plasma is accelerated down the length of this annular gap.

Two cylindrical center bodies are used in this experiment as electrodes, 2 in. and 4 in. (Figure 14) in diameter with the larger electrode broken up into two sections by a quartz insulating ring [2]. The quartz ring is sputtered with gold strips (Figure 15) connecting the two sections of the cylindrical center bodies. The gold strips are vaporized by the ignition power supply (doghouse) to form the plasma propellant that is driven downstream by Lorenz forces due to the current from the main power supply [2]. Gold was chosen as a propellant because it is not used in any other part of the thruster. This will allow the gold propellant plasma to be tracked via emission spectroscopy as it travels down the thruster in future experiments without contamination by other gold sources. Also, gold was chosen because of its high mass, which results in slower moving plasma, and in future firings will be compared against another material of lighter mass, for instance aluminum. For more information on the thruster refer to [30].

Early test firings by Keefer and Moeller [13] of the thruster revealed a rapid firing of the main thruster capacitor that resulted in a relatively non-uniform discharge (Figure 16). The frames in Figure 16 progress bottom to top and left to right. The first frame of this photo is in the bottom left hand corner

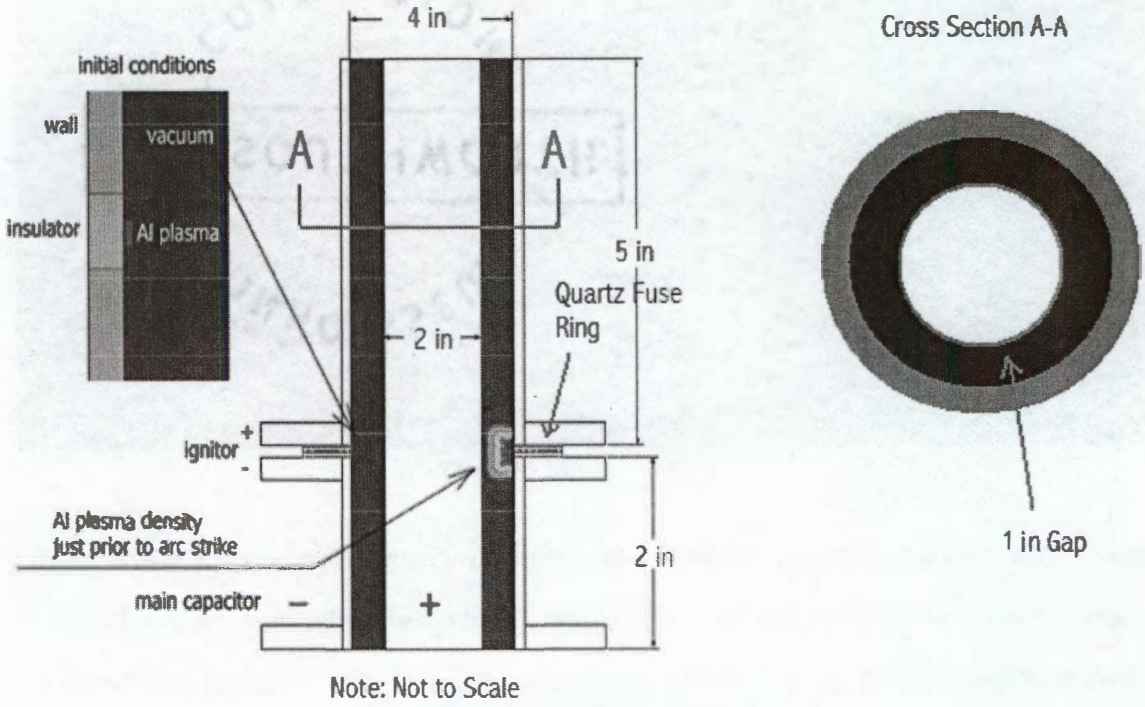


Figure 13: Thruster Schematic [30]

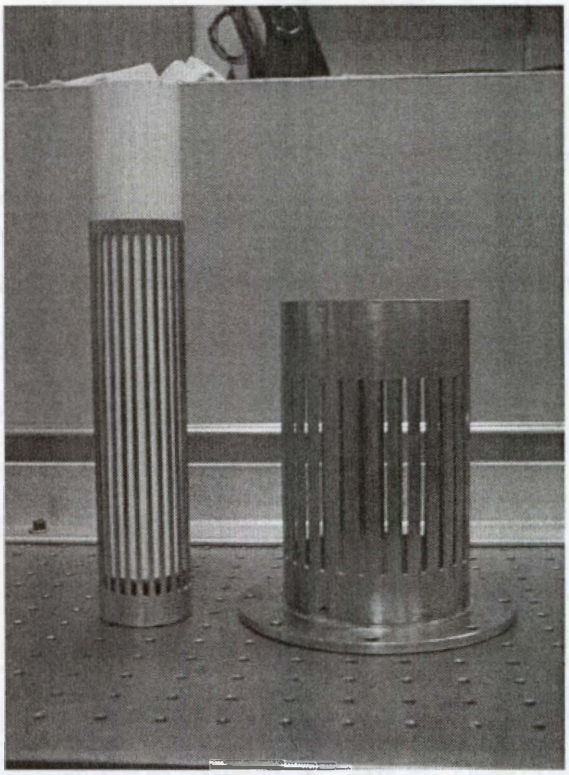


Figure 14: 2 in. Inner and 4 in. Outer Electrodes with Axial Slots

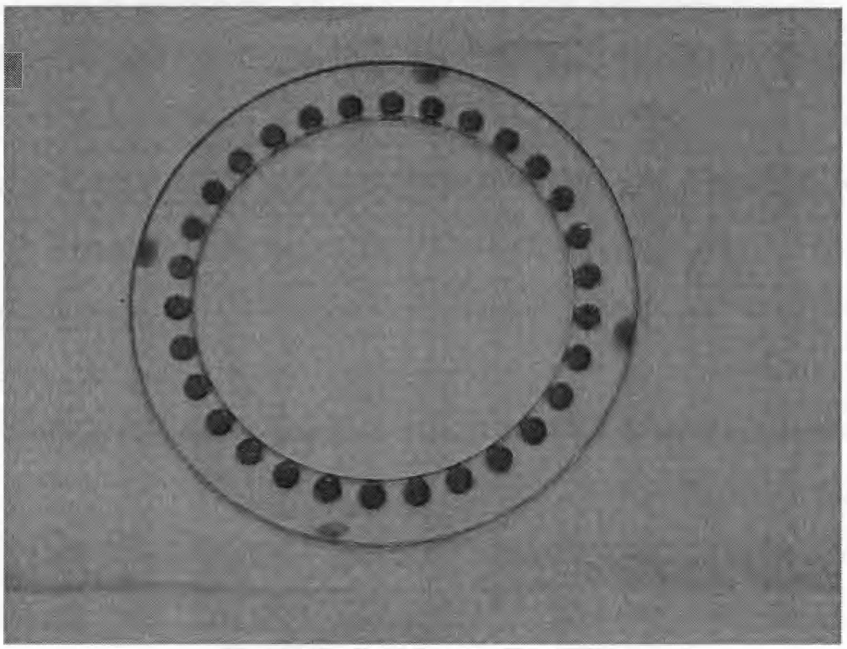


Figure 15: Gold Sputter Fuse Ring

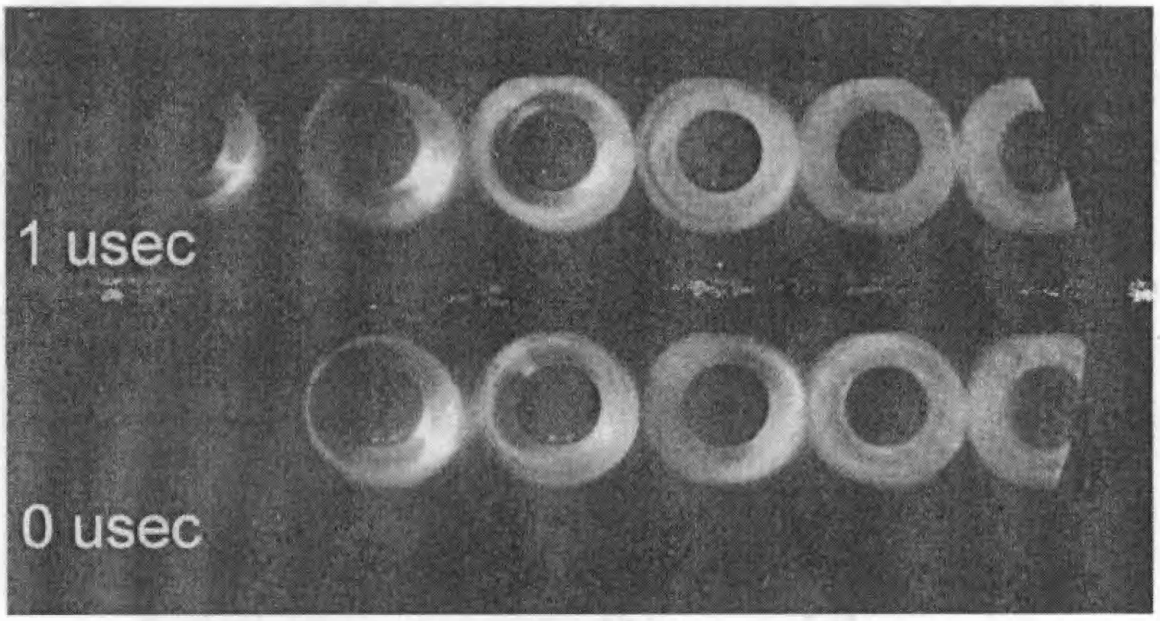


Figure 16: Non-Uniform Plasma Discharge [13]

and the second frame is the one above it and so on. To provide more-uniform data for comparison with the computer simulations the plasma non-uniformities need to be minimized [13]. Because the MACH2 code is 2-dimensional, axisymmetry in the experiment is necessary to make valid comparisons with computer simulation results. In the ideal case the plasma would remain axially symmetric as it travels down the length of the thruster. Several changes were made by Dr. Moeller and Mr. Newt Wright at UTSI to the thruster electrodes in order to combat this non-uniformity. The connection point of the trigger of the high voltage power supply (doghouse) was moved as far away from the fuse ring as possible (Figure 17) to reduce a magnetic flux that is induced at the propellant foils when the "doghouse" is fired [13]. This lowers the magnetic flux density and promotes a more uniform the fuse current.

In addition, the inner and outer electrodes were altered to provide a more uniform plasma discharge. First, axial slots (Figure 17) were cut out of the outer electrode between the quartz fuse ring and the high voltage connection of the trigger capacitor [2]. These slots create an array of parallel inductances between the fuse and the trigger power supply that act as an inductive divider to force the current flowing through the electrode to be uniform [2]. This effect can be explained with the same theory behind a

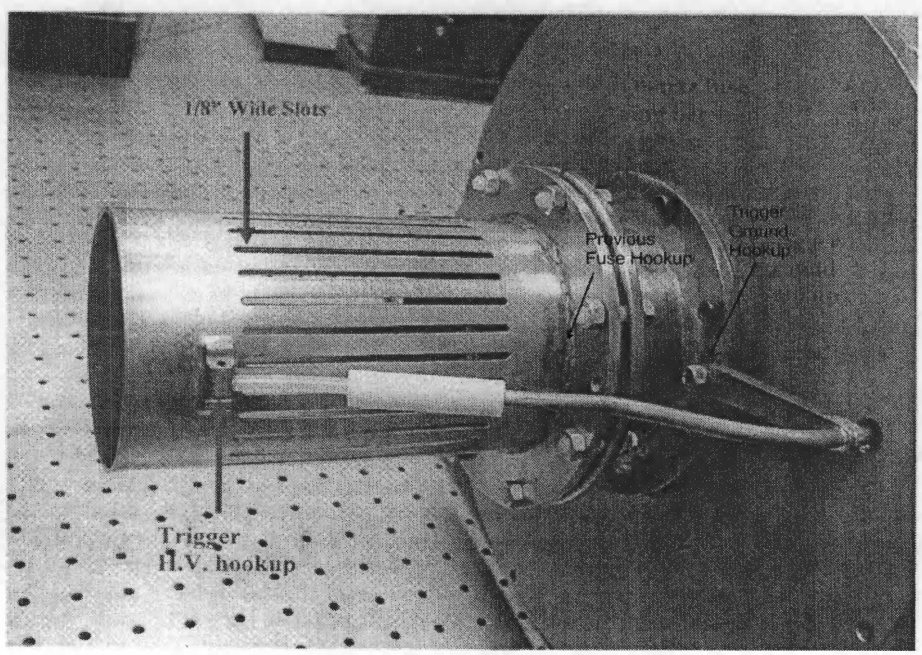


Figure 17: New and Old Trigger Hookup [2]

parallel, equal resistance circuit. When a circuit is designed with parallel equal resistance paths, the voltage drop across each of the current branches is the same. Therefore the current through each branch will be the same when the impedance through each branch is the same.

After implementing the above changes, the thruster was fired and some fuse-plasma non-uniformities still occurred. It was then decided to modify the inner electrode by installing axial slots in it as well. The slots on both electrodes were specially rounded in order to prevent arcing due to the presence of a strong electric field [14]. The inner electrode slots force the main capacitor current to pass through an inductive divider immediately following current initiation, rather than being delayed until the current reaches the slotted section of the outer electrode that is downstream on the fuse disk [13].

The thruster electrodes are housed in a vacuum chamber fabricated from stainless steel tubing and plates designed specifically for this thruster [2]. The main capacitor is sealed off from the actual thruster and the high vacuum region by a G-10 insulating ring that could be filled with sulfur hexafluoride to minimize the possibility of internal arcing [2] if a problem arises. The vacuum system (Figure 18) being used to evacuate the volume around the thruster consists of two different internal pumps. First a mechanical pump brings the test chamber pressure down from atmospheric pressure to roughly 10^{-3} torr, and then a diffusion pump brings the pressure down to an operating pressure between 10^{-5} and 10^{-6} torr. Note that when the thruster operates, the vacuum pump is able to sustain this pressure because the thruster operates with a single pulse and introduces very little mass into the test chamber.

b. Diagnostics

In most plasma experiments the main parameters being studied are the magnitudes of current passing through the plasma and the magnetic and electric fields inside and outside the plasma region [17]. In the present research experiment, the main points of interest were the characteristics of plasma generation, electric discharge (both need to be uniform in order to compare to results obtained with the MACH2 computer simulation) and the induced magnetic field. Several different devices were used to

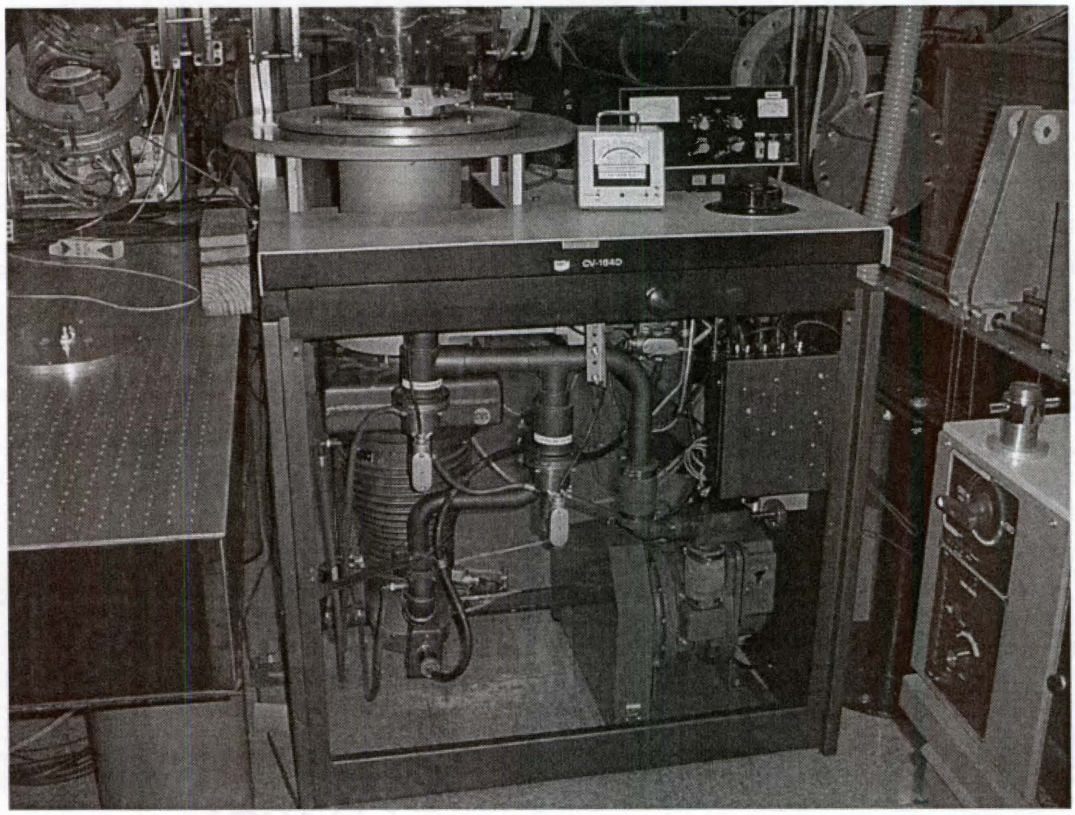


Figure 18: Vacuum Pump

measure these parameters. A flat quartz window was located on the vacuum chamber at the thruster exit to allow for interferometric, photographic and spectroscopic measurements [2]. An additional window on the end of the vacuum chamber (Figure 19) was used for an end-on view of the electric discharge for additional photographic measurements.

A single-beam, heterodyne laser interferometer 1mm in diameter (Figure 20,Figure 21), was used to measure the line-of-sight integrated time dependent electron number density at a single station downstream of the exit plane [2,13]. In future experiments, data may be taken simultaneously at two axial stations in order to provide an estimate of the exhaust velocity [2]. The interferometer has two 50 m lengths of fiber optic cable. This cable length allowed the interferometer electronics to be positioned as far from the plasma as possible and this reduced the signal noise at the oscilloscope recording the data. The six black paddles in Figure 20 are polarization rotators that were adjusted to reach a peak signal value. The data was then recorded on one of two oscilloscope (Figure 22) used for this experiment.

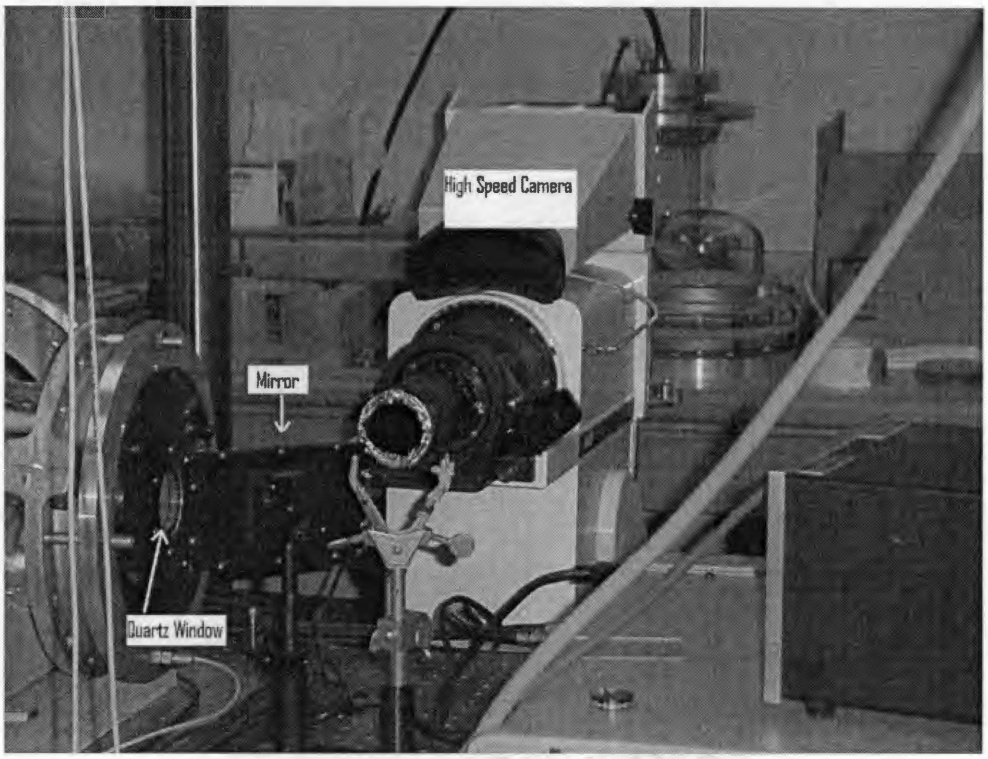


Figure 19: Camera Setup

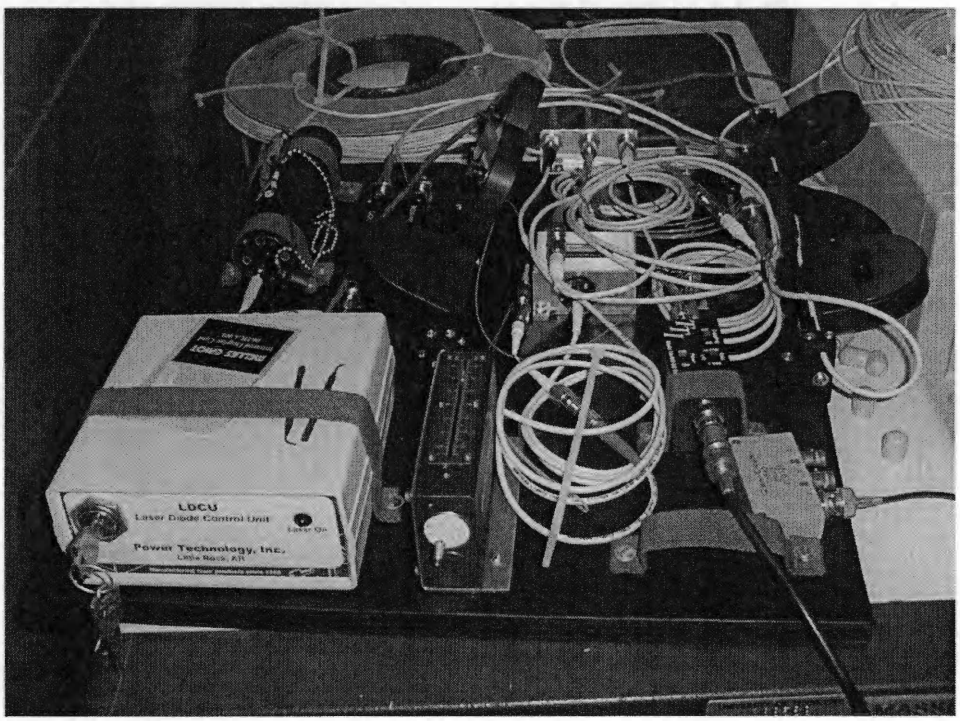


Figure 20: Laser Power Supply and Optics for Interferometer

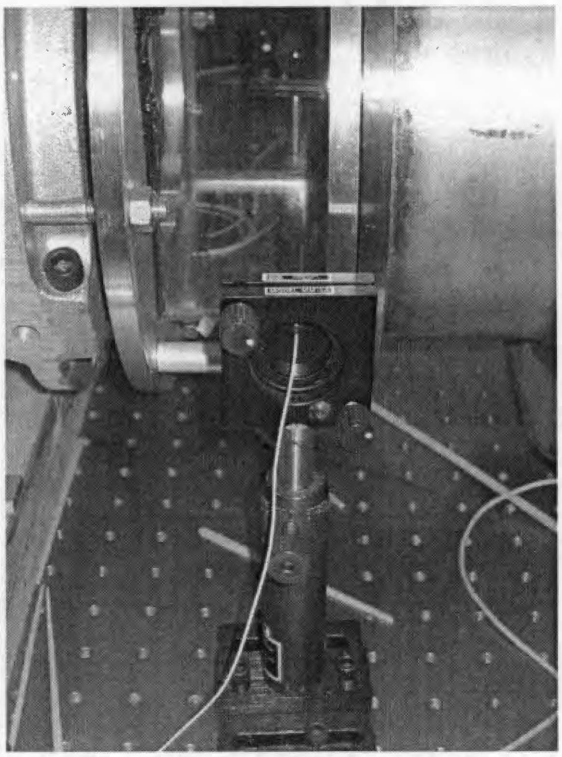


Figure 21: One End of Fiber Optic Laser Interferometer Located at Thruster Exit

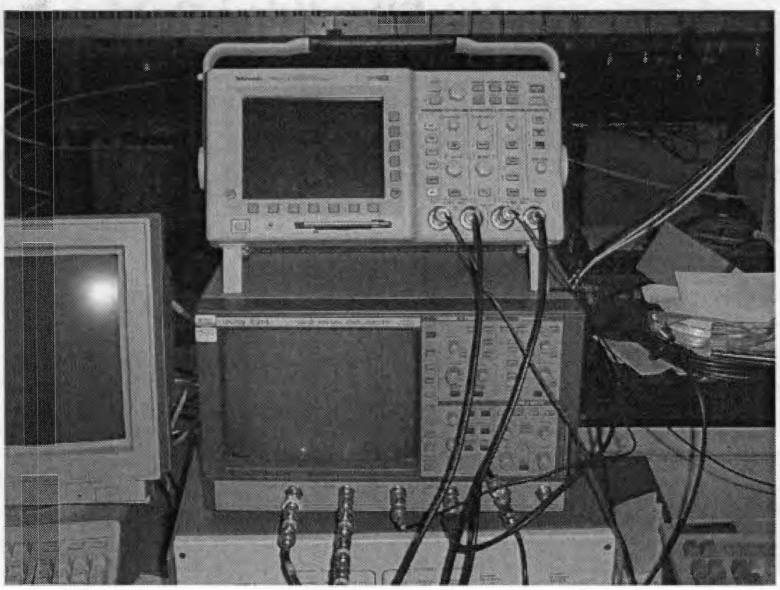


Figure 22: Two Oscilloscopes

A high speed camera (Figure 19), capable of a 20 MHz frame rate, was operated at 1 MHz frame rate for this experiment and was used to take high speed photographs of the plasma discharge as it developed. Two Rogowski coils, in the trigger and main capacitor circuits, were used to measure the time evolution of the current from both the trigger and capacitor [13]. A Rogowski coil consists of a solenoidal coil whose ends are brought around together to form an oval [17]. The coil obtains direct measurements of the total current flowing through its center and is typically used in plasma applications to measure the current flowing through the plasma [17]. A Rogowski coil was used for this application because it required no circuit contact with the current and thus did not disturb the flow of plasma or interfere with other instruments [17].

There were two oscilloscopes used in this experiment to record the signal of both Rogowski coils, the interferometer, and 4 of the 13 B-Dot probes. The oscilloscope, shown in the top of Figure 22, was capable of recording at frequency of 60 MHz; it was used for recording the interferometer data and channels 1 and 2 for 2 of the 13 B-Dot probes. The bottom oscilloscope was used for both Rogowski coils and channels 3 and 4 of the B-Dot probes. Data from all the B-dot probes were recorded via high speed A/D converters cards (Figure 23) that stored the data until it was downloaded. The B-Dot data from the oscilloscope was compared against the data from the converter cards to ensure accurate readings. After a firing, data from the oscilloscopes and the A/D cards were downloaded to a computer for analysis.

c. B-Dot Probes

While the Rogowski coils, laser interferometer, and high speed photography described above were used in this experiment, the main focus of this thesis is on the analysis of data taken from the B-Dot probes. The thruster was equipped with 13 B-Dot probes that were intended to measure the time evolution of the induced magnetic field of the plasma current sheet and thus the characteristics of the current sheet as it traveled down the thruster during a test firing. Five of the B-Dot probes positioned in the outer electrode can be seen in the photograph shown in Figure 24. The 13 probes were positioned as follows (Figure 25):

- One probe upstream of the fuse disk

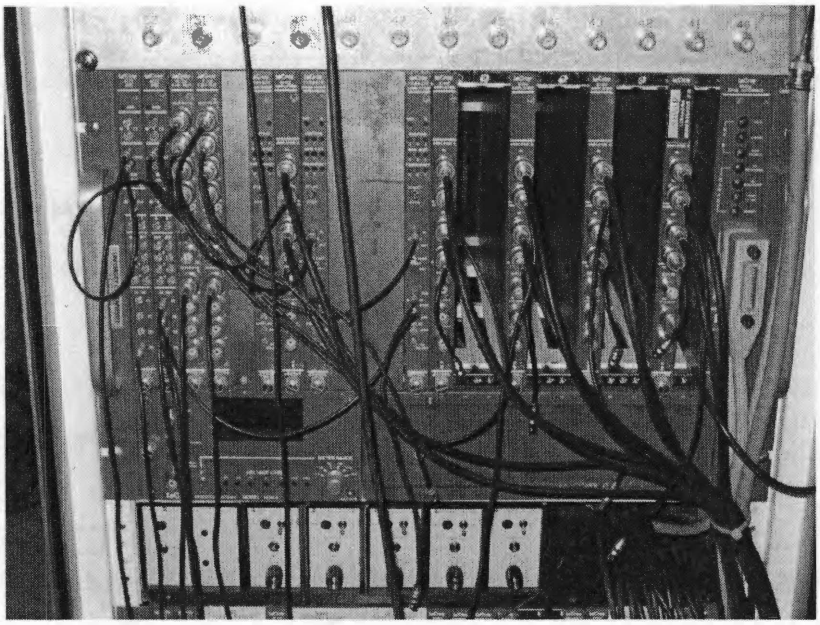


Figure 23: One of Two Data Collectors

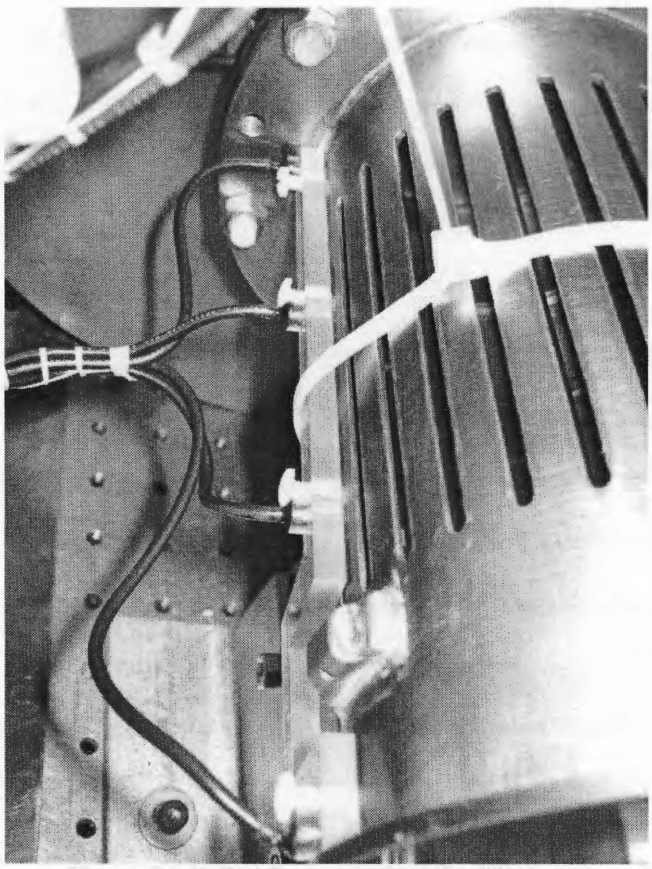


Figure 24: B-Dot Probes in Place on Thruster

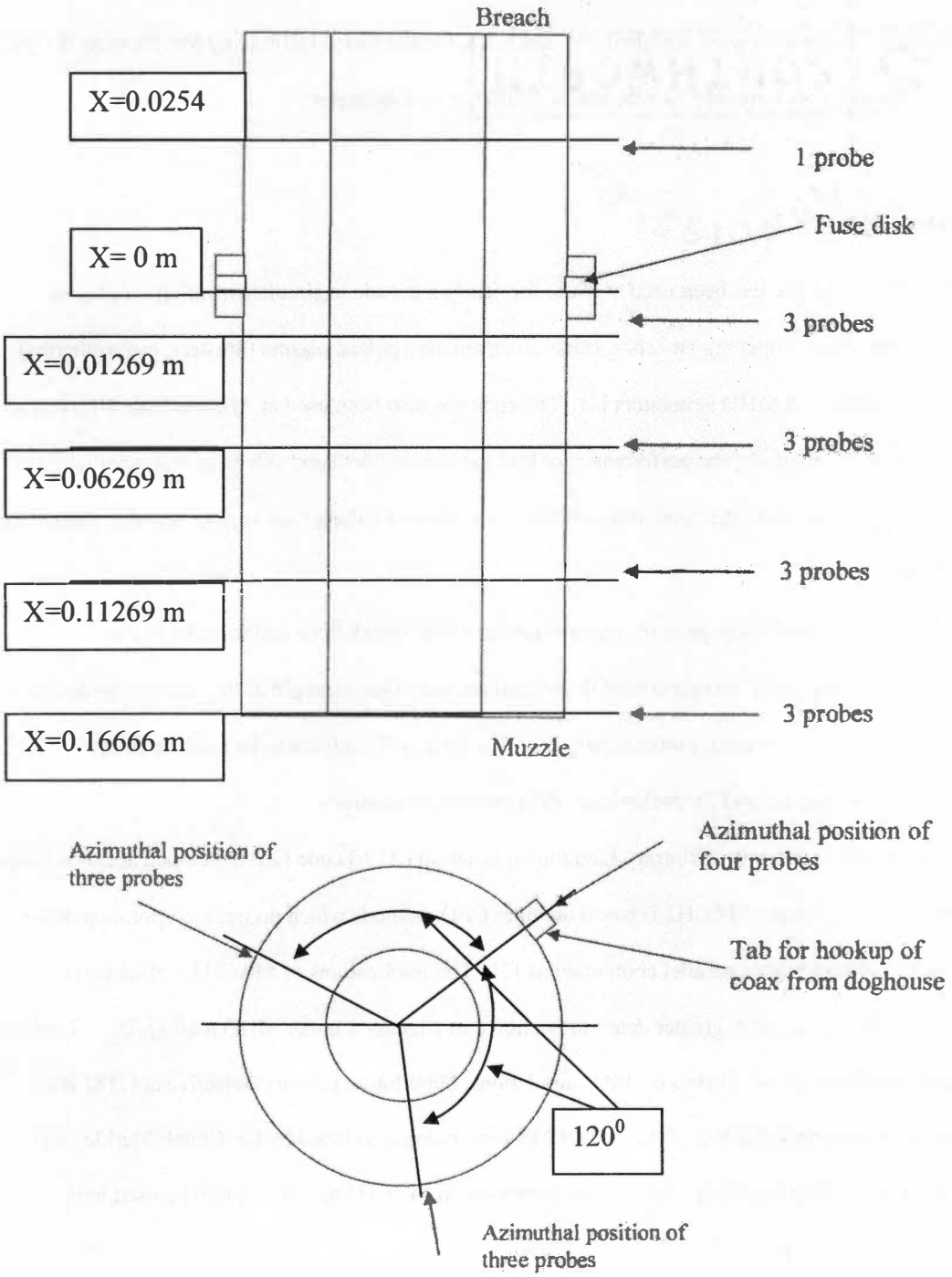


Figure 25: B-Dot Probe Locations [13]

- Three positioned 120° apart at four axial locations evenly spaced between the muzzle and the fuse [14]

The B-Dot probes being used were designed and constructed at the Space Institute by Mr. Newton Wright. They were made using 40 turns of #44 wire that is 1/2000 of inch diameter.

d. MACH2

The MACH2 code has been used at UTSI for nearly a decade to simulate a variety of plasma devices including: plasma opening switches, cable-guns, ablative pulsed plasma thrusters, electrothermal chemical (ETC) guns, and MHD generators [2]. The code has also been used at Arizona State University (ASU), among others, to model the performance of high power self-field and sub nano-watt applied-field MPD thrusters [9]. ASU used the code to model thrust and plasma voltages for various thruster geometries and propellants.

MACH2 was used early on in the experiment for initial simulations and to assist in the development of the laboratory equipment for the overall project. One example of this use was to design the fuse strips used to trigger the main power supply [2]. The code will continue to be used for future developments to the thruster and for preliminary PPA thruster simulations.

The MACH2 code is an Arbitrary Lagrangian Eulerian (ALE) code [13] developed at Los Alamos and Livermore Laboratories. MACH2 is based on older CFD methods which do not incorporate modern CFD techniques of gridding or parallel computations [2]. The implications of MACH2's older CFD architecture will be discussed in greater detail in Section c of Chapter 4 under MHD assumptions. Looking to the future, MACH2 will be utilized for PPA simulations, but a future primary objective at UTSI is to develop an electromagnetic version of the 3-D GEMS code being developed by Dr. Chuck Merkle and his colleagues at Purdue University [2]. For more information on MACH2 and how it will be used in the project please refer to [30].

Chapter 4: Theory

a. Thruster Operation

In electrodynamics, Ampere's Law is used to relate current density changes to the magnetic field strength. The Lorentz Force ($\mathbf{f}_B = \mathbf{j} \times \mathbf{B}$) explains how the plasma is electromagnetically accelerated down the thruster. In order to better understand how this thruster operates, let's look at a channel with current flowing through an ionized gas subjected to both an electric field **E** and a magnetic field **B** that are perpendicular to one another (Figure 26). If the gas has a simple scalar conductivity, σ, the current density can be represented by [19]:

$$\mathbf{j} = \sigma(\mathbf{E} + \mathbf{U} \times \mathbf{B})$$

Equation 2

The vector **j** is the electric current density, and it flows in the same direction as **E**. The $\mathbf{U} \times \mathbf{B}$ term in Equation 2 tends to reduce the net electric field because it established an electric field in the opposite direction as **E**. In addition to flowing parallel to **E**, **j** interacts with the external magnetic field **B** to provide a body force, $f_B = \mathbf{j} \times \mathbf{B}$, which drives the plasma down the PPA, to generate thrust. $\mathbf{f_B}$, the Lorenz force is also refered to as magnetic pressure [22]. Note: The direction of acceleration of the gas is described using the right hand rule for $\mathbf{j} \times \mathbf{B}$ and results in this axial force, $\mathbf{f_B}$, down the length of the thruster [19] (Figure 27). In the case of the laboratory prototype thruster, the discharge current is passed directly through the gold plasma formed between the electrodes and the Lorentz Force drives

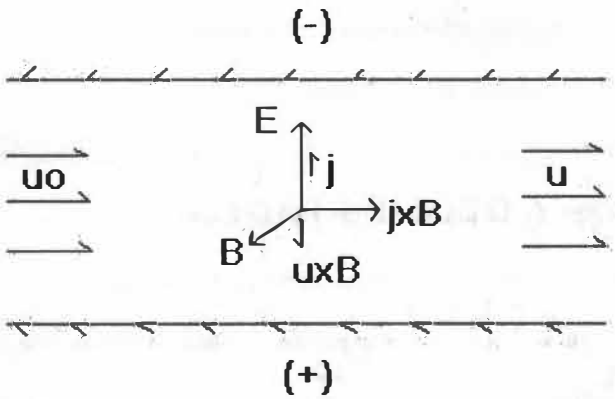


Figure 26: Forces in Thruster

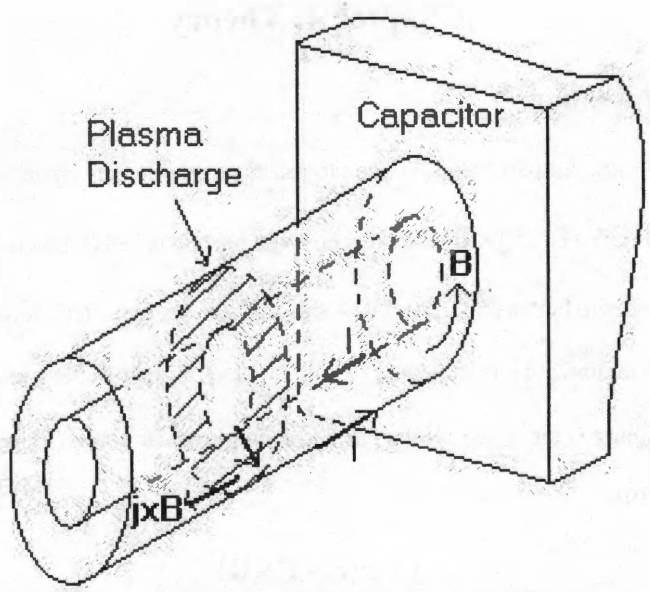


Figure 27: 3-D Thruster Diagram with Plasma Discharge

plasma down the length of the thruster (see Chapter 3 for additional details on the laboratory prototype thruster).

b. MHD Assumptions

PPTs are attractive to rocket designers because in theory they are capable of very high powers (MWatts power levels) and can be throttled. But this has only been proven at a smaller scale in laboratory testing [5,6]. In order to fully understand the behavior and performance of PPTs and to develop them to operate at higher power, an accurate simulation code must be developed. Most EP codes in use today use what are called the MHD assumptions, which states the following:

- Assumes displacement current, **D**, equals zero
- Charge density is zero everywhere in the plasma (the plasma is electrically neutral)
- **B** is specified often by a second order algebraic equation
- The electromagnetic field propagates through plasma by diffusion

A PPT will always either be fired in space or in a vacuum chamber. Therefore the thruster flow field will have two different regions with very different properties, a vacuum region and a region of relatively dense plasma (Figure 28). In a vacuum the displacement current is not zero, which makes the MHD assumption

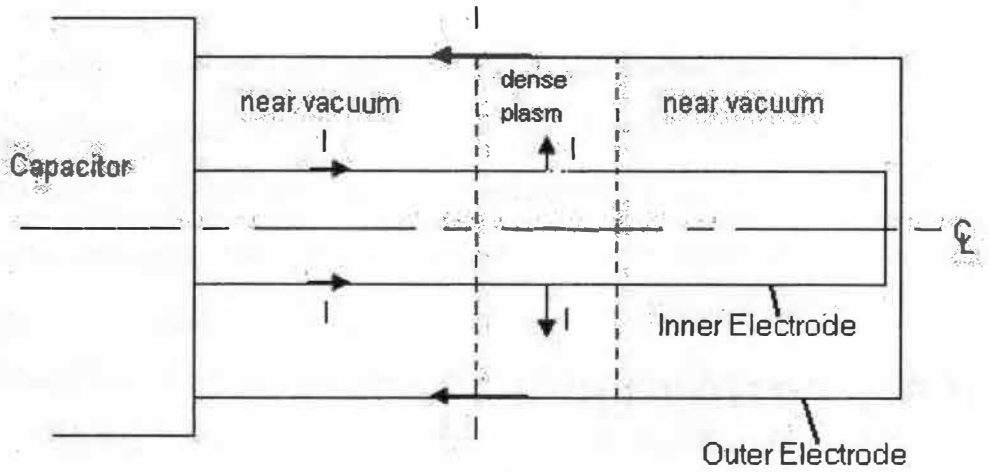


Figure 28: Thruster Set-Up with Current Flow

inaccurate, and the electromagnetic field propagates through the vacuum by waves. Since there will always be vacuum regions when working with PPTs, an electromagnetic code that supports displacement current must be developed. MACH2, a well established MHD code, is currently being used in preliminary thruster simulations. But this requires the use of a fictitious fluid called 'ether' to allow field propagation in vacuum regions via diffusion while adding insignificant mass to the system.

A code that uses the full Maxwellian equations must be developed in order to allow field propagation by both waves in vacuums and by diffusion in plasmas. A full Maxwell's equations solver makes the following assumptions for vacuum propagation:

- **E** and **B** are both first order equations
- The displacement current is not to equal zero
- The **E** and **B** fields are obtained by directly solving first order Maxwell's Equations
- The electromagnetic field propagates through plasma by waves

The General Equation Mesh Solver (GEMS) code, which is currently being developed by Dr. Chuck Merkle at Purdue University, can solve both Maxwell's equations and the MHD-version of these equations. The drawback of using the GEMS code is that it is far more complex than using MACH2 and requires far more computing power.

c. B-Dot Probes

A B-Dot probe is a small magnetic field probe that has a single or series of conductive loops which produces an output voltage proportional to the time rate of change of the magnetic flux linking the loop [20]. Placement and orientation of the B-Dot probes is very important in order to collect the data desired to track the current sheet in the thruster. The stationary circuit, C, (in this case the thruster itself) experiences a time varying magnetic field that passes down the thruster with the plasma flow. Both the time varying electric and magnetic fields travel down the barrel of the thruster, as described by Ampere's Law; the B-Dot probes are specifically placed to record the traveling magnetic field. A discussion of Maxwell's Laws, including Amperes Law, can be found in Appendix A.

B-Dot probes are sensitive only to the component of the magnetic field perpendicular to the plane of the loop and do not respond to fields parallel to the plane of the loop. Therefore the positioning of the probes is extremely important. This can be seen by studying the following equations:

$$V = NA\frac{d}{dt}(\mathbf{n}\cdot\mathbf{B})$$

Equation 3

where V is the voltage that is generated by the loops in terms of the loop geometry [20]. N is the number of coil loops and A is the area in side of one coil loop. An important variable to note, **n**, is a unit vector perpendicular to the plane defined by **A** that describes the orientation of the coil loops. One can further develop this equation to see the effect on orientation by introducing the Biot-Savart Law for **B** and using an alternate expression for the output voltage in terms of current, **I**, and distance, **r**, which results in [20]:

$$V = \frac{\mu_o NA}{4\pi}\frac{d}{dt}\int\frac{(\mathbf{n}\times\mathbf{I})\cdot\mathbf{r}}{|\mathbf{r}|^3}dV$$

Equation 4

Orientation now plays a more important role in this equation because when **I** is parallel with **n**, the cross product $n\times\mathbf{I}$ will be zero and as a result so will the voltage. This means that the probe cannot be parallel to the current, or it will read zero voltage and would provide no data for this experiment. B-Dot probes must be positioned perpendicular to the current in order to record the maximum voltage. Now since the direction of the magnetic field is azimuthal, so must be the axis of the B-Dot probes. In order to maximize

probe voltage, the axis of the B-Dot coil will be positioned parallel to the magnetic field. The exact positioning of the B-Dot probes was discussed in the Chapter 3.

The B-Dot probes are designed to respond to the change in the magnetic field as it travels down the length of the thruster. The output of the probes records in volts, and a conversion from volts to either current or the magnetic flux density, which is measured in Teslas, must be performed. This is done through a calibration process.

The B-Dot probes were calibrated in their specified locations on the thruster by exposing them to a current pulse provided by the thruster trigger power supply. This calibration process exposes the B-Dot probes to similar conditions realized in an actual thruster test. In the calibration process, the thruster electrodes were shorted. This was done by removing the quartz fuse disk from the electrode circuit (Figure 29). Therefore, no plasma is introduced to the thruster while calibrating. The self-induced magnetic field that is naturally created by the current pulse through thruster geometry was used in the calibration process. The two ends of the thruster were shorted with two copper metal plates (Figure 30, Figure 31) to allow the current to flow down the inner electrode to the downstream end of the thruster and back to the upstream and through the outer electrode in order to flow past all of the B-Dot probes. Because no probes are located

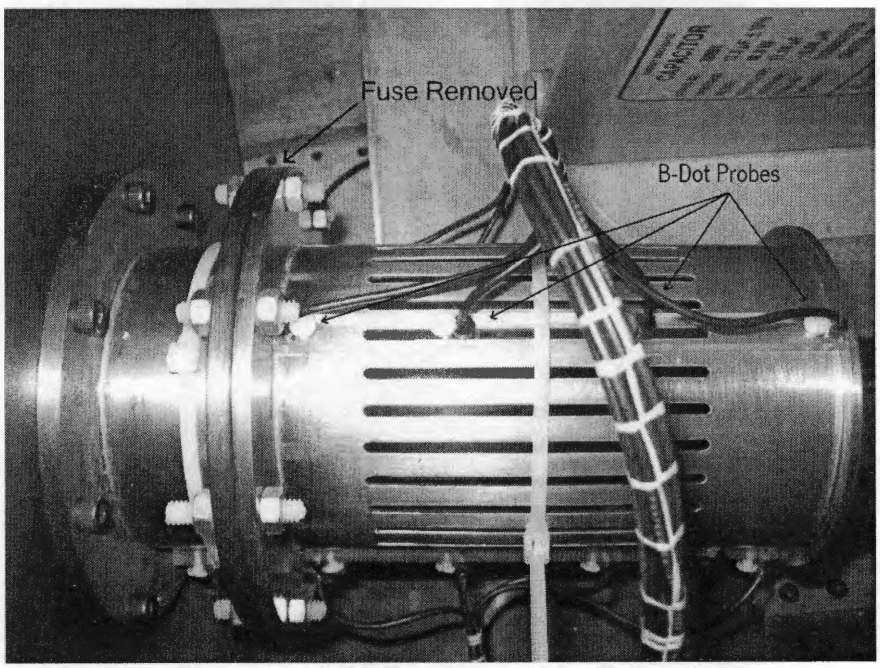


Figure 29: Thruster with the Fuse Removed for Calibration Purposes

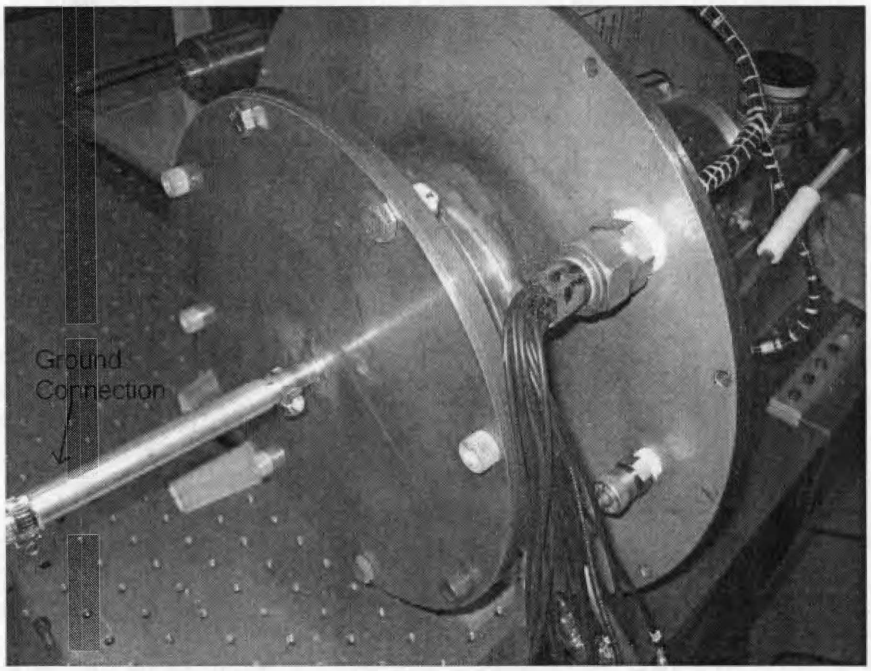


Figure 30: Back of Thruster with Plate Bolted to it for Calibration Purposes

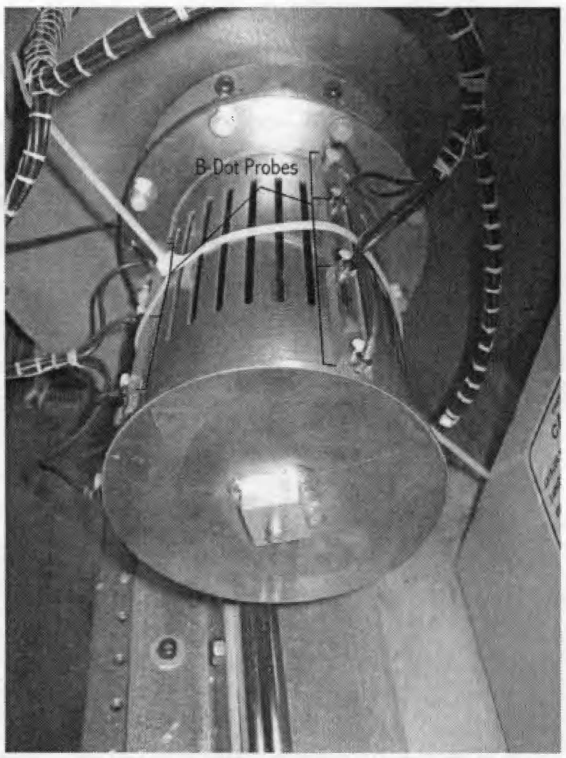


Figure 31: Front of Thruster Setup for Calibration

on the inner electrode, the electrode geometry does not affect the field generated at the radius of the B-Dot probes. To simplify the calibration setup, the inner electrode was replaced with a stainless steel rod (Figure 30). This setup is axially symmetric to promote uniform current flow. The calibration voltages were recorded by the B-Dot probes, and since the current provided by the "doghouse" capacitor is known, a known current was then related to each of the voltages produced by the B-Dot probes. The resulting calibration constants for each of the B-Dot probes can be found in Table 4.

d. Circuit Analysis

The main purpose of this thesis is to provide data with which to calibrate and validate PPA computer simulations of PPAs. Although the PPA is being modeled by both the MACH2, and eventually the GEMS, thruster circuit analysis can provide insight into dynamic behavior of the PPA as a transient electrical circuit machine. With the capacitance of the thruster known, the impedance in the circuit model can be adjusted to match the calculated current in the modeled circuit with that measured in the experiment. The circuit impedance (not including the capacitance) is comprised of the resistance and the inductance of the thruster circuit, R and L, respectively. The resistance and the impedance of the thruster can be found for the applied voltage both with and without plasma (fuse disk removed). Note that there is no easy way to measure these values straight from the thruster. Using the data recorded from the B-

Table 4: B-Dot Integration Constants

B-Dot #	Integration Constant (Amps/volts)
1	9.5438E+09
2	5.8595E+09
3	4.5119E+09
4	4.0845E+09
5	5.8597E+09
6	5.1254E+09
7	4.6073E+09
8	5.3088E+09
9	5.1531E+09
10	6.5861E+09
11	5.6859E+09
12	5.5521E+09
13	6.5722E+09

Dot probes and Rogowski coils, along with the use of Kirchoff's laws, one can make reasonably valid estimates of these values for use in the computer simulations.

A model of the thruster circuit is shown in Figure 32. The two unknown are L and R, while the voltage and current are recorded in the experiment. The circuit capacitance is assumed to be that of the main capacitor. (This assumes the circuit capacitance of the thruster electrodes and external circuit is small when compared to that of the thruster capacitor). When the switch in the circuit is closed, the total voltage in the circuit can be calculated by adding the voltage drop across the different components connected in series, Equation 5. Now, using the basic current-voltage relationships for resistors (Equation 6), capacitors (Equation 7), and inductors (Equation 8), one can write a complete equation for this circuit, Equation 9.

$$v(t) = v_R + v_C + v_L$$

Equation 5

$$v_R(t) = R \cdot i(t)$$

Equation 6

$$v_C(t) = \frac{1}{c}\int_0^t i(\tau)d\tau + V(0)$$

Equation 7

$$v_L(t) = L\frac{di(t)}{dt}$$

Equation 8

$$v(t) = R * i(t) + \frac{1}{c}\int_0^t i(\tau)d\tau + V_0 + L\frac{di(t)}{dt}$$

Equation 9

In this case the initial voltage, V_0, is nonzero. Since the data from the B-Dot probes and the Rogowski coils both are converted to current through calibration constants it is desired to solve Equation 9 for current as well as voltage. In order to solve for i(t) you must differentiate Equation 9 with respect to time (Equation 10).

$$0 = \frac{di(t)}{dt}R + \frac{i(t)}{C} + \frac{d^2i(t)}{dt^2}L$$

Equation 10

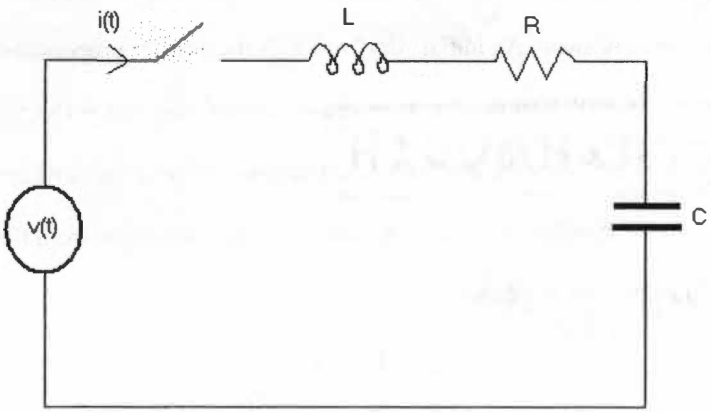


Figure 32: Transient Circuit

Since the power source (the power supply that charges the capacitor) is direct current (DC) the derivative of its voltage with respect to time will be zero. Solving for i(t), this equation gives three possible answers. The underdamped case ($\alpha^2<\omega^2$), critically damped ($\alpha^2=\omega^2$), and the overdamped case ($\alpha^2>\omega^2$).

Where $\alpha = \frac{R}{2L}$ and $\omega = \sqrt{\omega_0^{\,2} - \alpha^2}$. For more information on this process please refer to [25].

For this PPA application, the underdamped solution will be used because it best reflects the observed data from the B-dot probes and the Rogowski coils. Equation 11 gives the underdamped solution. The capacitance is known, and the capacitor voltage is recorded for the time interval of a thruster run. This leaves the resistance, R, and the inductance, L, as the unknowns in our equations. As stated previously the resistance and inductance, both with and without the plasma, are needed for the thruster simulations.

$$i(t) = \frac{V}{\omega_d L} e^{-\alpha t} \sin(\omega_d t)$$

where

$$\alpha = \frac{R}{2L}$$

$$\omega_0 = \sqrt{\frac{1}{LC}}$$

$$\omega_d^{\,2} = \omega_o^{\,2} - \alpha^2$$

Equation 11

The thruster circuit impedance changes when the fuse plasma is present (Equation 12) which leaves four unknowns instead of two. An initial "dry" run with the thruster propellant fuse shorted was conducted on the thruster. This allowed the data from the Rogowski coils and B-Dot probes to fit the curve with R_p and L_p both equal to zero since there is no fuse and no plasma involved in this run. Using all of the other successful runs from the thruster, an average R_p and L_p can be formulated from Equation 11. The results of these runs will be present in Chapter 5.

$$L = L_p + L_0$$

$$R = R_p + R_0$$

When fuse is shorted

$$L = L_0$$

$$R = R_0$$

Equation 12

Chapter 5: Data and Results

a. Data

By firing the PPA in a series of one-shot experiments data was obtained from 13 B-Dot probes (measuring time-resolved magnetic field throughout the thruster), two Rogowski coils (measuring the current flow from two capacitors), and a heterodyne laser interferometer (measuring the phase shift in laser light to give the line-of-sight electron number density [4]). Multiple thruster runs totaling 11 in all were conducted, and each run was analyzed and then compared with other thruster runs, to find trends in the data. In order to compare data from experimentation with predictions taken from the GEMS and MACH2 computer simulations, the data must be put into the proper form. In most cases this involved numerical integration and the application of a calibration constant. However, some data was processed using digital signal processing. The B-Dot probes are the main focus of this thesis, and they provide major portion of the data collected.

i. B-Dot Probes

The B-Dot probe data were initially recorded as voltage vs. time; a representative case is shown in Figure 33. (Note that all dates in the figure descriptions are the day on which the thruster was run.) Data from B-Dot 1 (positioned upstream of the propellant fuse disk) is presented in this figure and was obtained from the run conducted on September 20, 2005. The B-Dot probe data were recorded with two devices; four of the B-Dot probes were recorded onto an oscilloscope and can be compared for discrepancies with the data taken from the LeCroy data collector. The LeCroy data collector recorded data from all 13 B-Dot probes. The data taken from the LeCroy collector are the actual data that are used in the analysis in this thesis. B-Dot 1 is located in position 1 (Figure 34), located 0.0254 m from where the outer electrode is attached to the capacitor, and it is the only B-Dot probe located at axial position 1. The other four axial positions each have three B-Dot probes spaced 120° apart, to form the three different sets, giving a total of 13 B-Dot probe data sets. At a given axial location, each azimuthal location will be related to a data set (Figure 34). Set 1 is located at the same azimuthal position as the trigger power supply hookup; Sets 2 and

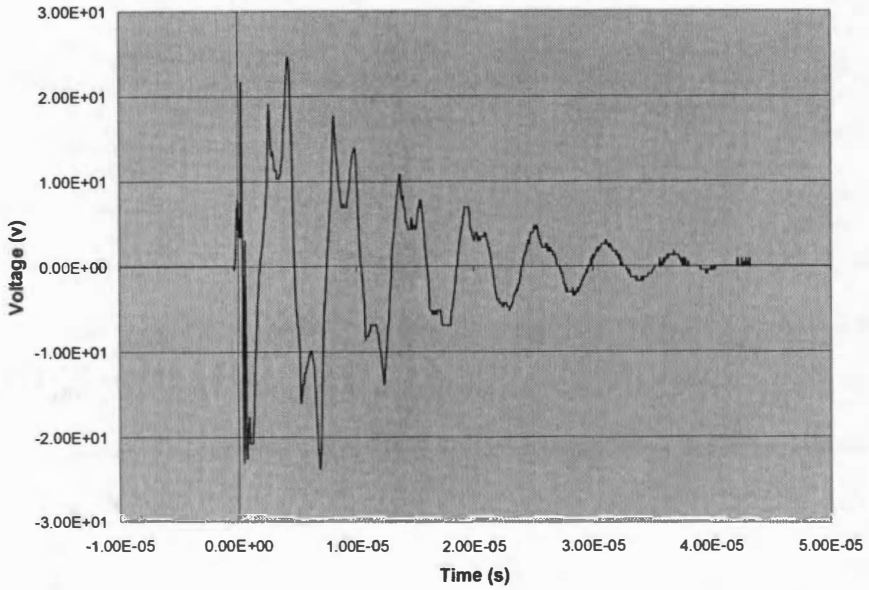


Figure 33: Raw Signal from B-Dot probe 1 Upstream of the Plasma Flow (Sept. 20, 2005)

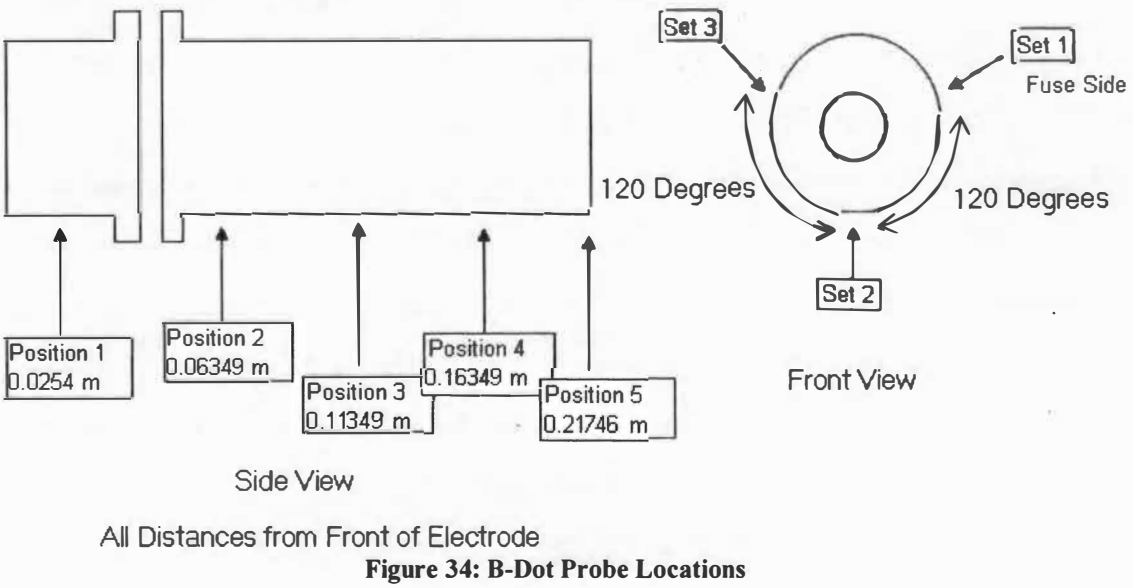


Figure 34: B-Dot Probe Locations

3 are located 120 and 240 degrees clockwise from Set 1, respectively. The axial distances, given in Figure 34, are from the leading edge of the electrode (the connection point to the capacitor). The B-Dot probe numbering is as follows:

- B-Dots 1-5 are located at the Set 1 azimuthal position and correspond to 5 different axial positions
- B-Dots 6-9 are located at the Set 2 azimuthal position and correspond to axial positions 2-4
- B-Dots 10-13 are located at the Set 3 azimuthal position and correspond to axial positions 2-4

Since B-Dot 1 is located ahead of the fuse disk, which is the source for the plasma propellant (in this case gold), it gives data that is the easiest to read of the 13 probes because the current following through the probe is "clean", clean meaning that no plasma has been introduced into the system at this location. By the time the current passes over the last three B-Dot probes, located at the 5^{th} axial position, the magnitude of the current is reduced and asymmetries in the plasma have developed as it accelerates, making it very difficult to interpret the data from these B-Dot probes. Digital signal processing methods were used to help with this analysis, and those methods will be discussed later in this chapter.

ii. Rogowski Coils

The two Rogowski coils, one located in the trigger "doghouse" capacitor circuit and the other located in the "main" thruster circuit, provided data that was recorded as voltage vs. time. Example data can be seen in Figure 35. These data sets were taken from the main and trigger Rogowski coil on the November 29, 2005 run. The amplitude of the data from the trigger Rogowski coil is significantly less than that from the main Rogowski, as can been seen by comparing the two in Figure 35. This is expected because the current flowing from the trigger capacitor is about $1/6^{th}$ of the current of the main Rogowski coil. It should be noted that the trigger capacitor is fired first to generate the plasma propellant, which then closes the thruster circuit to fire the main capacitor. Therefore, the trigger Rogowski data initial spike precedes that in the main Rogowski data (as seen in Figure 35). The main use for the Rogowski data is to help determine the B-Dot probe integration constants, but the data are also used to aid finding the inductance and the resistance of the thruster. The process for finding the integration constants and the

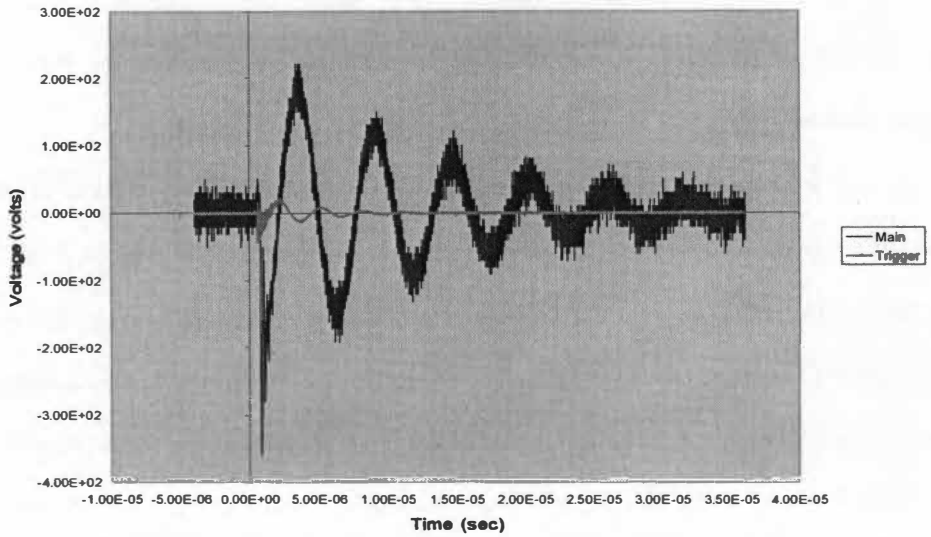


Figure 35: Raw Data from the Main and Trigger Rogowski Coils (Nov. 29, 2005)

inductance and resistance will be described later.

iii. Laser Interferometer

Representative raw data taken from the laser interferometer are displayed in Figure 36 having been recorded by one of two oscilloscopes; again this data was taken from the November 29, 2005 run. The raw interferometer data is dense in time, but it was processed to give a laser light phase shift from which the line of sight electron number density was obtained. The purpose of this data is to directly compare the experimental electron number density with an electron number density predicted by the computer simulations.

b. Data Analysis

Since the data that was recorded from the experiment was not in a form that could be used for direct comparison with the computer simulations, it was analyzed and processed into another form. As stated before, the B-Dot probe data was first analyzed to determine the current, first by integrating the data and then applying an integration constant (Table 4) that is determined through calibration (refer to Chapter 4). When studying the raw B-Dot data (Figure 35) one might notice that there is significant amount of high

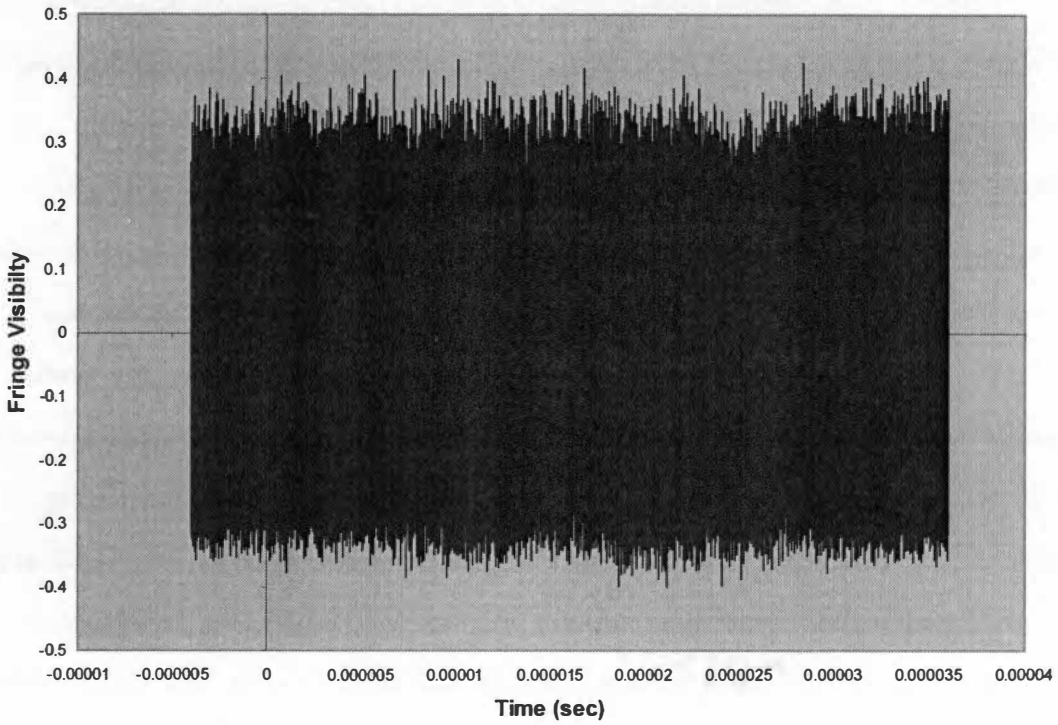


Figure 36: Raw Data from the Interferometer (Nov. 29, 2005)

frequency noise (this is even more evident in some of the other B-Dot probes). Since the ultimate goal when analyzing the B-Dot data is to find the peaks in the graphs of the integrated data that corresponds to when the current sheet passes the probe, most of this noise needs to be removed with filters. This includes B-Dot 1, located upstream of the fuse disk. Although B-Dot 1 does not have any plasma traveling past it, the current sheet still passes it.

Five or seven point median filters were used for this purpose. The median filter is a simple filter that analyzes a set of consecutive data points, either 5 or 7, determines the median value, and the central point in that set is replaced with the median of those points. For instance if the 5 points in the data set are 2, 8, 6, -3, and 5, those points would be rearranged, lowest to highest, as -3, 2, 5, 6, and 8. The median of this set would be 5, the middle number. This median replaces the third number (6) of the original set, and for the next step the new set consists of the old set with the first number replaced by the next number in the overall data set. The median filter moves through the entire set of data in this manner.

This may seem like a simple method but it does an effective job reducing the high frequency noise in the data, as can be seen in Figure 37 which shows a small portion of data taken from the raw data of a B-Dot probe. In order to find a local maximum or minimum of the current (note that the raw data is proportional to the time derivative of current), one must find when the time derivative of the current is zero. In our application, points at which the derivatives are zero can be found on the graph of the raw data taken from the B-Dot probes (the data being studied is the integral of the raw data). The original raw data denoted B-Dot 1 in Figure 37 has ten different points where the curve crosses the x-axis. This would correspond to ten different current reversals (local maxima or minima) in the integrated data in a time-span of $2X10^{-6}$ sec. Applying the median filters reduces the number of intercepts in the x-axis to just one, making the graphs much easier to interpret (in order to find the current reversals in the integrated data) and giving more accurate results (1 current peak instead of 10). The 5 and 7 point median filters produce different results; the 7 point filter tends to flatten out the data more than the 5 point filter. However, each gives essentially the same value at which the time derivative of current equals zero. One potential drawback with using these median filters is a case where no high frequency noise is present. For this special case the filters tend to reduce some of the peaks and flatten out the original raw data when it is not

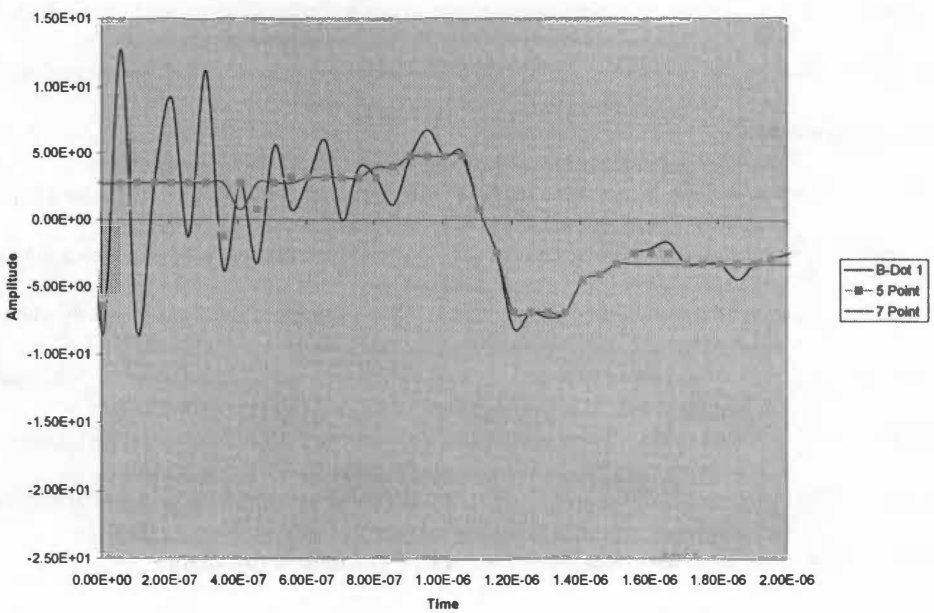


Figure 37: Raw B-Dot Data with Median Filters (Sept. 7, 2005)

desired. So when determining a peak of the integrated B-Dot data, the five or seven point median filter is used only when high-frequency noise is present. It should be noted that median filters are not used for the Rogowski coil analysis because that once the data is integrated it does not have the high frequency noise realized in the B-Dot data.

After the median filters have been applied to the raw B-Dot data, the remaining procedure for the analysis of this data is the same as for the 2 Rogowski coils. For the sake of brevity this process will be discussed just once here. The raw voltage data from the B-Dot and Rogowski coils was numerically integrated to produce the current signals. Both Trapezoidal and Simpson's methods of numerical integration were initially tested (for more information of these methods please refer to [15]). Even though Simpson's rule generally gives a more accurate representation of the data [15], this was not the case in the B-Dot analysis, possibly because of the high frequency noise. Due to the nature of the data recorded for this experiment, the Trapezoidal method gave the more accurate representation [16]. Simpson's method tended to increase the upward or downward drift (discussed later in this chapter) that is already present in the data.

The Trapezoidal method (Equation 13) is a very simple method of numerical integration but for our purposes it did an excellent job. Numerical integration of the voltage signals with the trapezoidal rule was performed using the following equation:

$$\int_{t_{n-1}}^{t_n} f(t_n)dt = \frac{h}{2}\left[f(t_{n-1} + f(t_n)\right] - \frac{h^3}{12} f^{"}(\xi)$$

Equation 13

where h is a determined time step, from $t_n - t_{n-1}$, and $\frac{h^3}{12} f^{"}(\xi)$ is the error introduced using this method. Once the raw voltage data of the B-Dot probe or Rogowski coil has been integrated, the integration constants (Table 4) were applied to the B-Dot data (Figure 38); Rogowski data has also been properly adjusted for calibration (Figure 39). (Note: "trap" refers to the trapezoidal rule, "trap5" or "trap7" refers to the trapezoidal rule applied after either a 5 point or 7 point median filter, respectively) has been applied to the raw data. At this point the data has been used to construct the time-dependent behavior of the current.

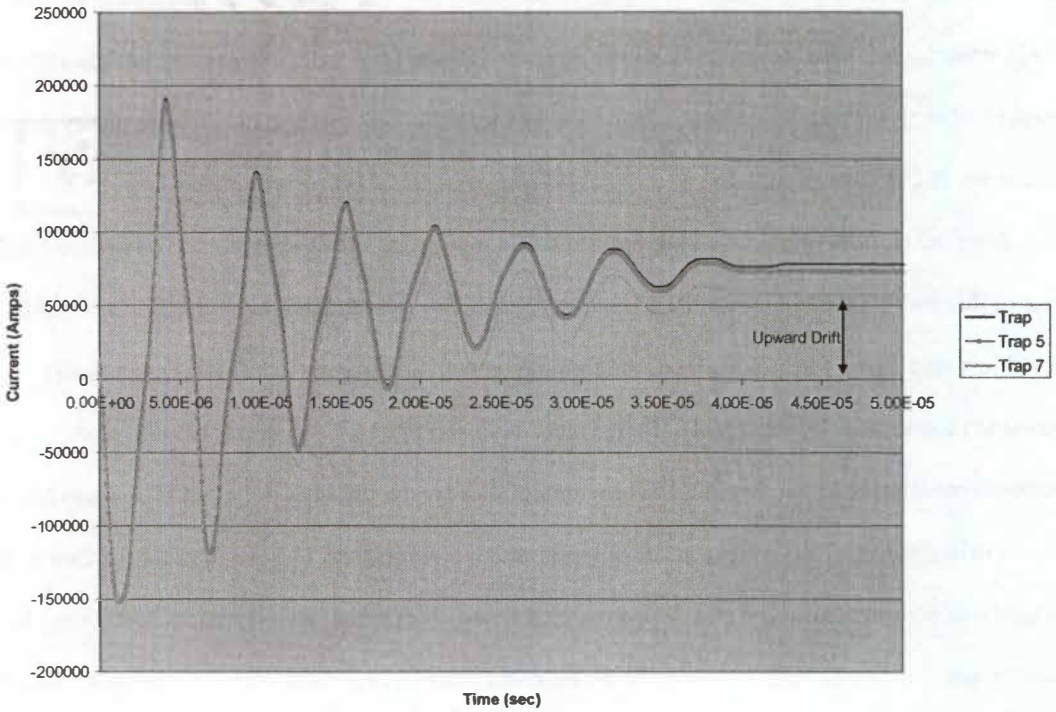


Figure 38: Integrated B-Dot Data from the Raw Data in Figure 33 (Sept. 20, 2005)

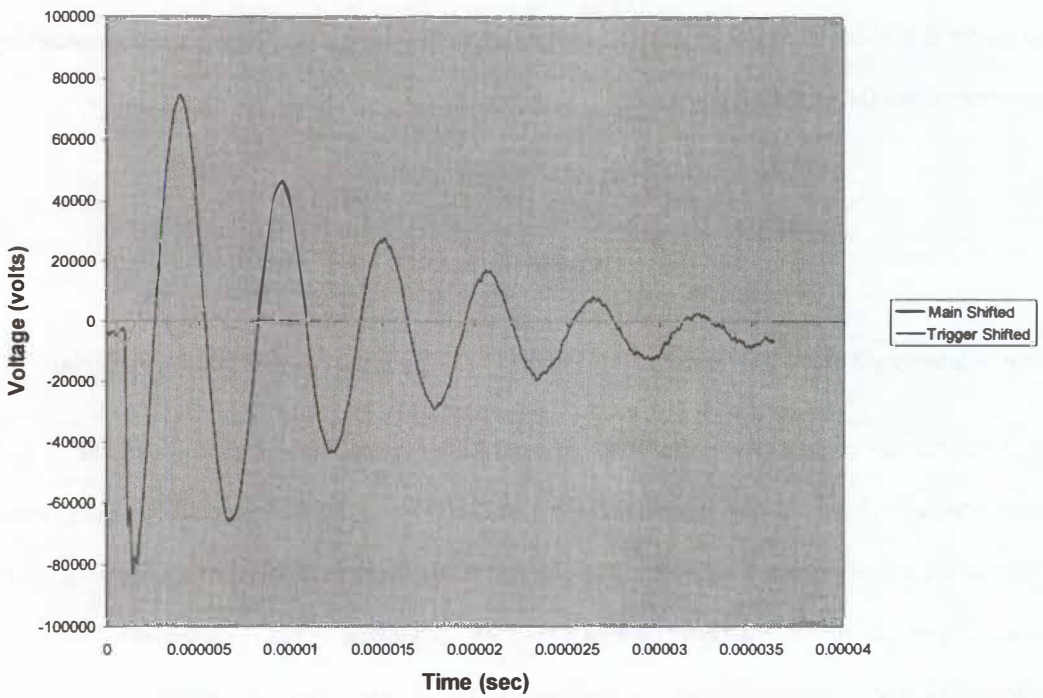


Figure 39: Integrated Rogowski Coil Data from the Raw Data in Figure 35 (Nov. 29, 2005)

The integration constants from Table 4 and the time shifts introduced by variation in channel triggers in the data acquisition system were found using a method referred to as cross correlation (Equation 14) [15]. This variation was caused by the data acquisition system not recording the same occurance in the thruster at the same time on all channels. This may partially be a result of variations in length and resistance in the wires that are connected to the B-Dots and relay the signal to the data acquisition system.

$$cc(d) = \frac{\sum_i \left[(x(i) - mx) * (y(i-d) - my) \right]}{\sqrt{\sum_i (x(i) - mx)^2 * \sum_i (y(i-d) - my)^2}}$$

Equation 14

where d is the time delay and varies to best fit the correlation to give the time shift. The cross correlation of two data sets, x and y, is a standard method of estimating the degree to which two sets of data are correlated. In this case the Main Rogowski coil data is x(i) and the B-Dot probes and trigger are each y(i). cc is the percentage of correlation, not the degree to which the two data sets vary. The latter is what is needed to find the integration constant. Based on Equation 14, Dr. L Montgomery Smith (UTSI) developed a new relationship (Equation 15) which gives the inverse integration constant, c(d), as well as the time shift

$$c(d) = \frac{\sum_i x(i) * y(i+d)}{\sum_i x(i)^2}$$

Equation 15

between the main Rogowski coil and the B-Dot probes that will be applied in a later analysis. This time shift is a result of the delay in the trigger of each channel in the data acquisition system, it varies between 4.28E-07 s and 6.6E-07 s. This may seem like a small value, but when comparing the current data of one B-Dot probe to another, this time delay can be extremely important. The timing of the current peaks in the current data is used to find the velocity of the current sheet; eliminating the error from the data acquisition system results in a more accurate velocity measurement. This cross correlation method is also used to find the trigger Rogowski coil integration constant (2.8973E+09 A/v) and time shift (1.5E-06 sec).

Figure 38 shows the different current curves obtained with trapezoidal integration, one trapezoidal method using 5 point and the other using 7 point median filters. In this graph, the trapezoidal method using

a 5 point median filter appears to be the best method used for further analysis, because it removes most of high frequency noise and because it results in less error in the numerical integration (upward drift) than the 7 point filter. This upward drift results from the integration of a small zero offset. Also note that the deviation between the three methods is inconsequential because the amplitudes and current values are less important than the timing of the passage of the current sheet for the analysis in this thesis.

The integrated B-Dot data had two types of error associated with it, current drift (zero offset) and the time offset. Due to zero offset error in the data collectors and the error introduced using the trapezoidal integration method, the integrated B-Dot data typically had either an upward or downward drift. Referring to Figure 38, one can see that the data does not exactly start at zero and the data has an upward drift when it should be centered around the x-axis. Proper filter selection mitigates this error by eliminating very low frequencies that introduce a direct current shift. The time shift was a relatively easy one to fix as it only involves subtracting or adding the time delay from the start time. This value, along with the integration constants, was found using the cross correlation method discussed earlier in this chapter. Correcting the upward drift, in this case, involved using another filter referred to as a high-pass filter (Equation 16) at the suggestion of Dr. Smith [16].

$$HPF(z) = \frac{2}{2+\omega_a \Delta t} \frac{1-z^{-1}}{1-\frac{2-\omega_a \Delta t}{2+\omega_a \Delta t} z^{-1}}$$

Equation 16

In this equation ω_a is the analog cutoff frequency which is constant for the analysis of the B-Dot probes for all of the different runs at each voltage which in Equation 16 is designated as z. Sample B-Dot data before and after application of the high-pass filter are shown in Figure 40. In order to directly compare data from each of the B-Dot probes to data of the other B-Dot probes and to the Rogowski coils, ω_a must be the same for all cases. A time shift, as a result of using the high-pass filter, also must be the same for all probes in order to not change the timing of these curves. ω_a was arbitrarily chosen at first and then updated until it

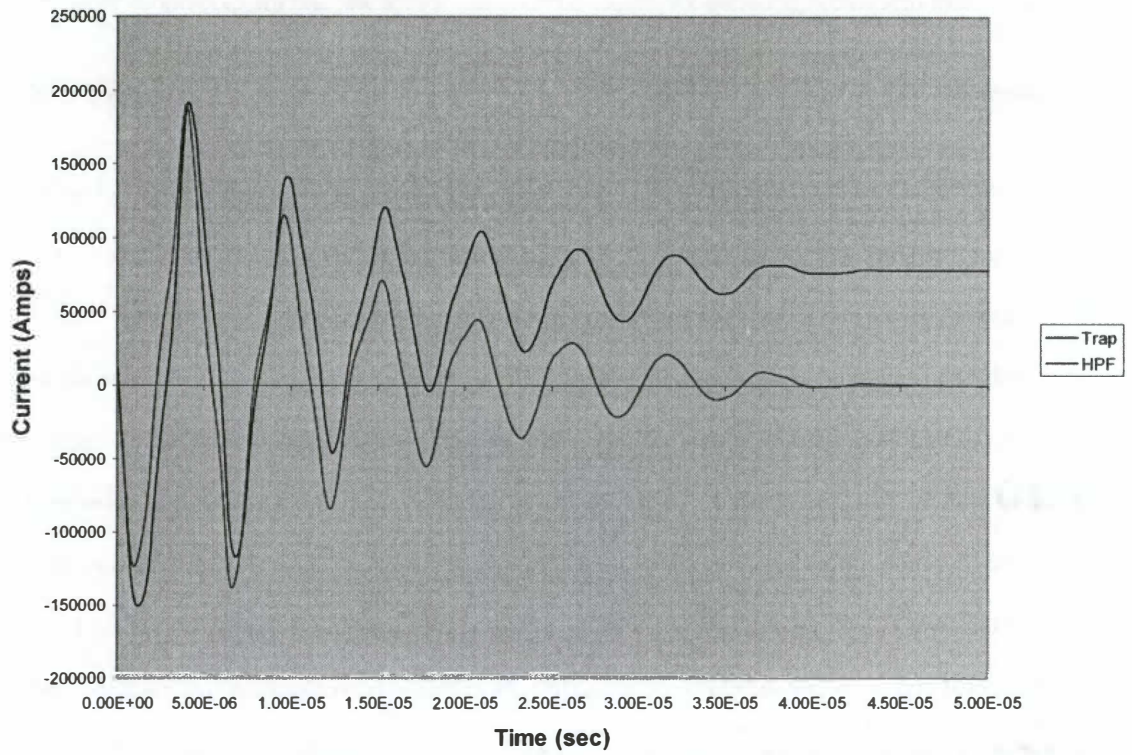


Figure 40: Shifted B-Dot 1 Data (Sept. 20, 2005)

best fit the majority of the data. The final value obtained for ω_a was 0.98. Initially, the high-pass filter was applied in two different ways, either before or after integration was completed. The latter method was utilized because the former tended to introduce a larger time shift. Again timing, specifically timing of the current peaks as they pass the B-Dot probe coils, is so important in this analysis that it must be obtained as accurately as possible. The high-pass filter was also applied to data from the Rogowski coil. This allowed for a direct comparison between B-Dot probe data, Rogowski coil data, and the current predicted by the circuit analysis discussed in Chapter 4. Comparing these three curves helped determine the resistance and inductance of the thruster and plasma (discussed later in this chapter).

i. Thruster Current

As stated earlier, the purpose of this experiment was to provide experimental results for later comparison with similar results made with a computer simulation. One such comparison investigates the thruster current. Looking back to our circuit analysis in Chapter 4, the current in the system was modeled

by Equation 11. But first all of the circuit's voltage, capacitance, resistance, and the inductance elements must be determined. The voltage is determined $\left(i(t) = C\frac{dV(t)}{dt} \right)$ by the main capacitor (charged to 20 kV). The circuit main capacitor capacitance of 17.5 μF is designed into it by the manufacturer. This then leaves the circuit resistance and the inductance elements to be determined. The thruster impedance is the sum of a plasma resistance and inductance and the resistance and inductance of the basic thruster circuit. The circuit resistance and inductance, both with and without the presence of plasma in the thruster, must be found. In order to find the resistance and inductance of the thruster without plasma, the thruster experiment was conducted with the fuse disk shorted. Therefore, the thruster was run without any plasma introduced into the system. For more information on this process please refer back to Chapter 3. Once the run was conducted the data was compared to theoretical results predicted with Equation 11 (Figure 41) based on guessed values of R and L. While the match is not perfect, an excellent representation was obtained after the first peak, especially between the B-Dot probe and theory. The first peak appears to be cut off, believed to be the result of a spike in voltage that occurs when the thruster fires. Looking back to Figure 35, one can see the initial voltage spike when the main capacitor first discharges and a subsequently smooth damped sine wave. This initial high flux, in voltage and ultimately current, appears to cause the discrepancies in the

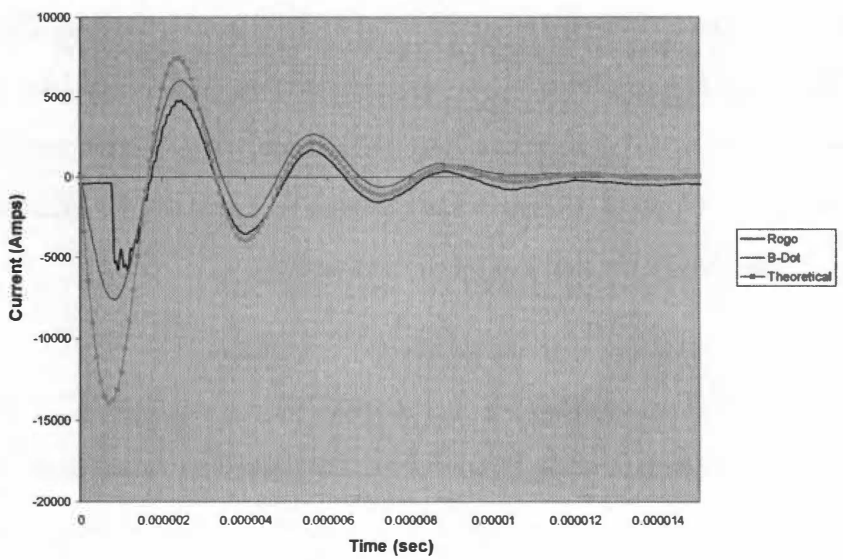


Figure 41: Comparison of B-Dot Probe 1 and Theory (without Plasma) (Oct. 22, 2005)

first peak in Figure 41.

Now with the values of resistance and inductance for the mechanical circuit obtained by the initial analysis, the resistance and inductance of the plasma can be found by adding corresponding plasma impedance values (by trial and error) to the overall resistance and inductance until the theoretical curves best match the current for a thruster with propellant plasma (Figure 42). Since the main goal of this thesis was to obtain and analyze B-Dot probe data to establish thruster current profiles for comparison with the computer simulations, only that data is used for comparison. Once again the first couple of current peaks (Figure 42) do not match exactly, but a very good overall representation was made. The discrepancies between the experimental data and the theoretical data may be caused by a variable resistance introduced into the circuit by the evolving propellant plasma (the theoretical data assumes a constant value of resistance). Since it is very difficult to model a circuit with variable resistance a best fit approach was made. The values of the total resistance and inductance can be found in Table 5. While a good comparison between the theoretical current and the experimental current recorded by the B-Dot probe 1 (Figure 42), this was not the case for most other B-Dot probes. Figure 43 is a comparison of the current history from B-Dot 2 (pink line) and the theoretical current (yellow line). The theoretical value comes nowhere close to

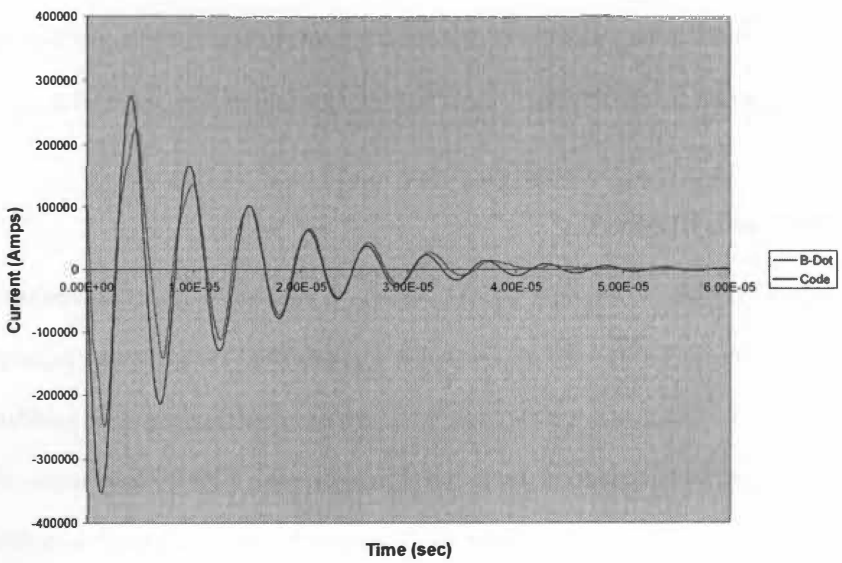


Figure 42: Comparison between B-Dot 1 and Theory (with Plasma) (Nov. 29, 2005)

Table 5: Total Resistance and Inductance Constants for Thruster Circuit with Plasma Present

Resistance (Ohms)	Inductance (Henry)
9E-03	4.5E-08

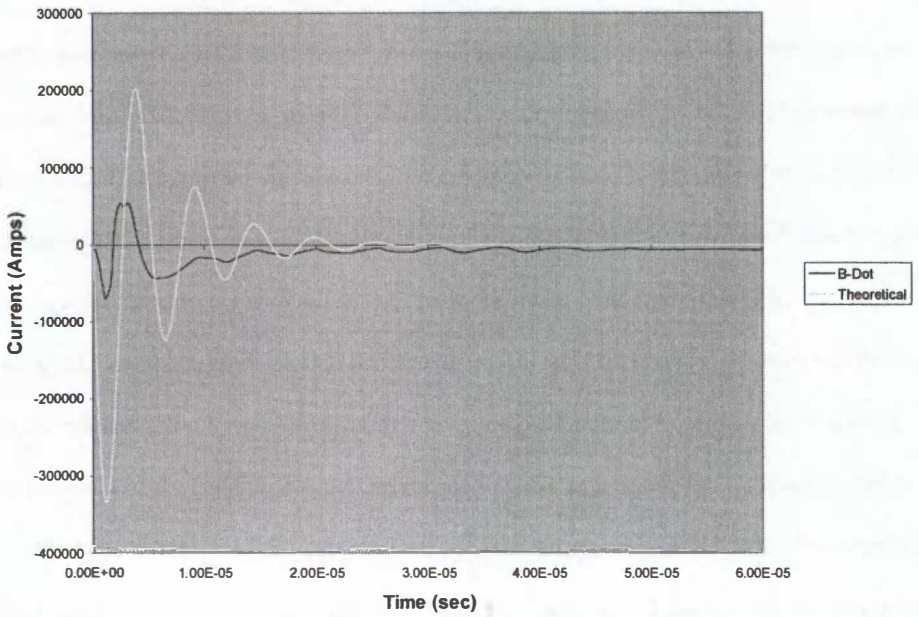


Figure 43: Comparison between B-Dot 2 and Theory (with Plasma) (Nov. 29, 2005)

modeling the actual current. To better match the B-Dot probe data before 30 μs, the circuit resistance must be increased. However, doing so results in a very poor match beyond 30 μs, and thus would not provide meaningful values for the computer simulations. By not being able to accurately model the current with this simple theoretical model, besides B-Dot 1, the need for a more sophisticated model is evident.

ii. Thruster Current Sheet

An optimized PPA has circuit impedance (capacitance, inductance, and resistance) that causes the current to be critically damped during a firing. Since it is not optimized, the laboratory prototype PPA and external circuit used in our work generate a current that is underdamped resulting in an oscillating current that rings down. Therefore multiple current sheets travel from the vase of the thruster to the thruster muzzle. A representative curve is shown in Figure 40. The magnetic field associated with these current sheets is propagated down the thruster by diffusion when the plasma is present and displacement current in

areas where plasma is not present. Note that the oscillating current results in an oscillating self-induced magnetic field that interacts with the current to produce a Lorentz force that is always in the same direction. It is very important to note that the velocity at which these current peaks and the corresponding electromagnetic fields that travel with them depends on the amount of plasma that they carry. During the ringing down of the current in the main thruster circuit, the doghouse trigger circuit that vaporizes the thruster propellant is also ringing down. MACH2 simulations indicate that the propellant mass is injected into the thruster annulus during many periods in the main thruster current. Therefore, the injection of the propellant mass occurs over multiple current peaks as the current rings down. Because the thruster current is ringing, it is important to track individual current peaks to determine the velocity at which each is traveling. MACH2 simulations suggest that greater propellant mass is injected and carried by the thruster current as time progresses for the first several cycles. Therefore, it is anticipated that the velocities associated with the corresponding peaks will decrease because they are carrying additional mass. The analysis of the current sheet velocities follows.

Another physical parameter of the PPA that is important for comparisons with the computer simulation is the velocity of the current sheet. This information was to be obtained from the passage of the peaks of the B-Dot probe data. This is the reason great importance was placed on easily reading these peaks. The timing of the peaks taken from graphs, such as those in Figure 40, and the uniformity of the current sheet at different axial positions can be determined with a skillful examination of the peaks and their timing (this will be discussed later in this chapter). To find the velocity of an object, in this case the current sheet, one needs to find the time it takes to travel a known distance. This distance in the thruster is known since it is simply the distance from one B-Dot probe to the next, and the time it takes to travel that distance can be found by tracking a specific current peak from one B-Dot to the next.

One problem that arose in early analysis was finding the current peaks in the B-Dot data; the B-Dot data is not always as clean as that seen in Figure 38. Therefore, the median filters and the high-pass filters were developed and used to aid this process. Due to the precision of the data recorders an exact time at which some peaks cross a B-Dot probe cannot be determined, a very good estimate can be extrapolated from the graphs. It is important to note that an uncertainty of plus or minus 50 nanoseconds must be

assumed since this is the time step determined by the frequency at which the data was recorded. An example of data that is difficult to interpret is shown in Figure 44. This data was taken from B-Dot probe 13 in the 5th position of Set 3. As one can see, it looks nothing like B-Dot 1 (data shown in Figure 42); it is much harder to determine where the peaks occur, much less find the specific time at which they cross the probe.

It is important to note that the number of resolvable current peaks is drastically reduced from position 1 to position 5. The farther downstream a B-Dot probe was positioned in the thruster, the harder its data was to interpret. This may be the result of the plasma disruption and spreading out axially as the current travels down the length of the thruster. In some cases, even with filters and side by side comparisons, it is impossible to tell exactly where each peak occurs. However, by using 13 B-Dot probes for each run, conducting multiple runs, interpolating the data, and making certain assumptions, some reasonable approximations were made to obtain a good estimation of where these current peaks were located.

All of the peaks that have been found for the run conducted on November 29, 2005 were put into Table 6 showing position (meters) vs. time (seconds). They are also grouped into the three different sets (azimuthal positions) and each peak is numbered, one for the first current peak and so on. This allows for a

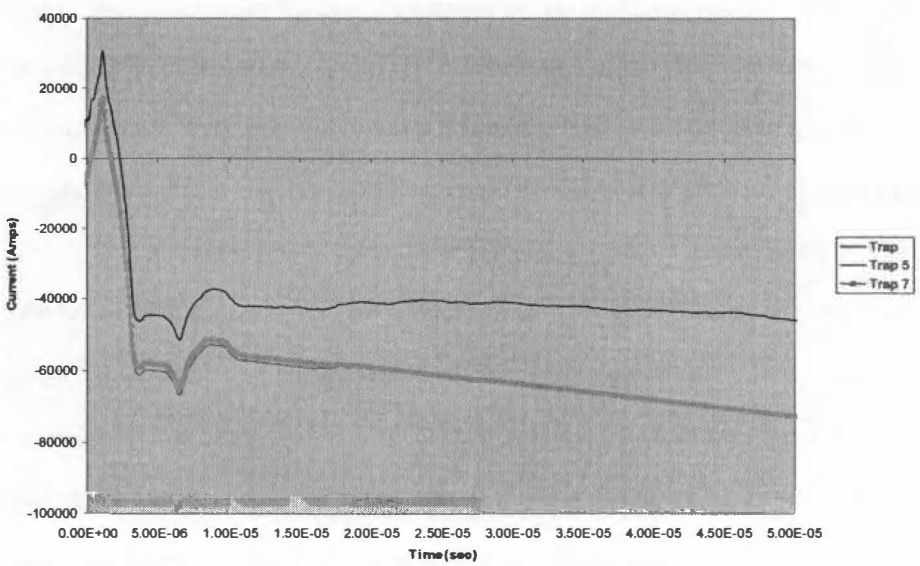


Figure 44: Integrated Data from B-Dot 13 (Sept. 7, 2005)

Table 6: Table Showing Times When Current Passes B-Dot Probes (Nov. 29, 2005)

B-Dot #	Azimuthal Pos	Position #	Distance (m) from Capacitor	Peak # 1	2	3	4	5	6	7	
1	0	1	0.0254	1.90E-06	4.80E-06	7.40E-06	1.03E-05	1.28E-05	1.57E-05	1.83E-05	
2	0	2	0.063495	1.98E-06	5.34E-06	8.86E-06	1.17E-05	1.42E-05	1.69E-05	1.95E-05	
3	0	3	0.113495	2.38E-06	7.63E-06	1.06E-05	1.29E-05	1.55E-05	1.74E-05	2.03E-05	Set 1
4	0	4	0.163495	1.99E-06	8.39E-06	1.12E-05	1.36E-05				
5	0	5	0.217465	2.77E-06	9.52E-06						
6	120	2	0.063495	1.80E-06	5.50E-06	8.90E-06	1.16E-05	1.42E-05	1.74E-05	2.00E-05	
7	120	3	0.113495	2.61E-06	7.51E-06	1.03E-05	1.36E-05	1.58E-05	1.88E-05	2.09E-05	
8	120	4	0.163495	3.12E-06	8.12E-06	1.21E-05	1.51E-05	1.79E-05			Set 2
9	120	5	0.217465	5.35E-06	1.09E-05	1.41E-05	1.61E-05	1.90E-05			
10	240	2	0.063495	1.88E-06	5.58E-06	8.89E-06	1.15E-05	1.43E-05	1.74E-05	1.98E-05	
11	240	3	0.113495	2.51E-06	6.71E-06	1.03E-05	1.33E-05	1.58E-05	1.85E-05	2.12E-05	Set 3
12	240	4	0.163495	2.35E-06	8.75E-06	1.29E-05	1.52E-05	1.79E-05			
13	240	5	0.217465	4.01E-06	8.91E-06	1.25E-05	1.93E-05	2.19E-05			

complete analysis of the B-Dot probe data of one thruster firing from this single table. The following examples are from the test run conducted on November 29, 2005.

For the experimental thruster firing to have the most impact on the development of a 2-D, axisymmetric computer simulation, the thruster must fire with an azimuthally uniform plasma. One can confirm the degree of azimuthal uniformity with the high-speed photographs of the firing, along with the B-Dot probe data. Because the B-Dot probes track changes in the magnetic field, and ultimately the current sheet, azimuthal uniformity can be studied by comparing subsequent current peaks in the data. For simplicity's sake, only the first two peaks are compared side by side. By studying when a single current peak crossed the B-Dots in each set, the azimuthal uniformity of the thruster at that point in time can be established. Then studying multiple peaks the plasma formation can be visualized. Figure 45 shows current peaks grouped into sets. (Note that sets and positions are shown in Figure 34.) The first group of three lines, one for each set, is the first peak; and likewise, the second group corresponds to the second peak (refer to Figure 34 for B-Dot probe and Set locations). The solid line refers to Set 1, the thin dotted line refers to Set 2, and the thick dotted line refers to Set 3.

For uniform plasma the lines for each peak would be the same. Note that since the velocity of the current sheet slows down as time passes, the slopes (velocity) of the first peak will be larger than the second peak. While not indicative of a uniform current, the curves of the first current peak are the same shape at each azimuthal position. This suggests that the small amount of plasma carried by the first current

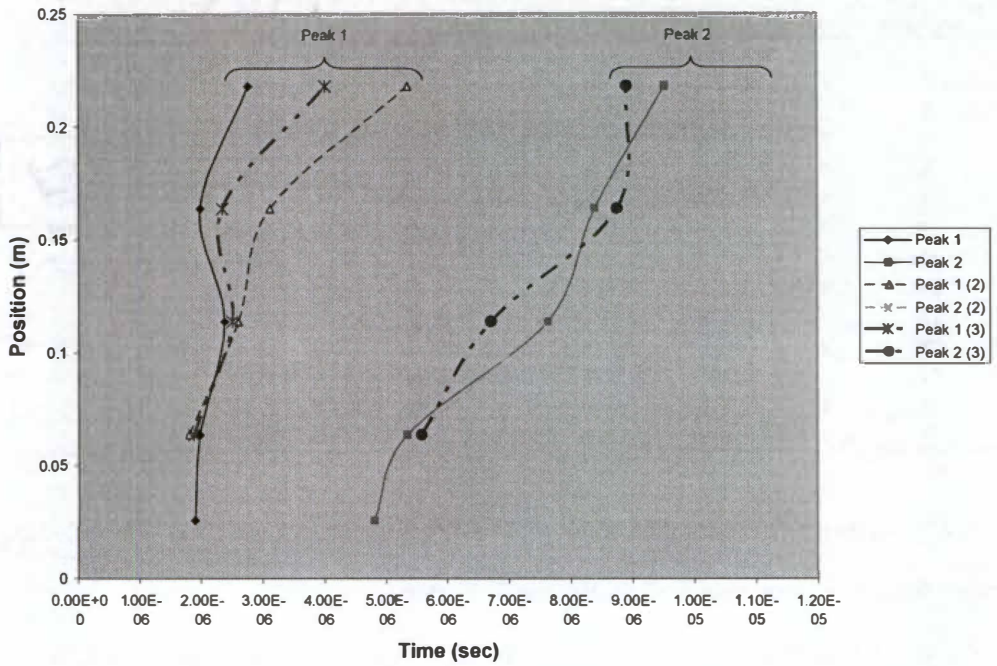


Figure 45: Peak 1 to Peak 2 Comparison for Sets 1-3 (Nov. 29, 2005)

pulse retains the same relative position as it travels down the thruster barrel. The same cannot be said for the second current peak; the order in which the current sheet passes each set changes from one position to the next. For instance for the first peak, Set 1 (solid line) registers first in all but the second axial position (where all three sets registered at the same time), then Set 3 (thick dotted line), and finally Set 2 (thin dotted line). For the second peak the order in which set registers a current peak changes for each position, indicative of a non-uniform current (and plasma) distribution.

Another way to asses the uniformity of the thruster plasma would be to analyze Figure 46. This is a graph of axial position along the length of the thruster vs. time. This graph describes the tracking of the first current peak (which if looking at Table 6 would be the first column of times), as if viewed from the side as it travels down the length of the thruster, and taking vertical slices at the five different axial B-Dot probe positions. So when the magnetic field passes a probe, the slice would be removed and placed at the corresponding time. Ideally, for an azimuthally uniform plasma and current sheet, this graph should have five straight vertical lines signifying uniform plasma that travels down the thruster. But this is not the case for this example test run, as can clearly be seen in Figure 46. While this graph shows that the thruster does

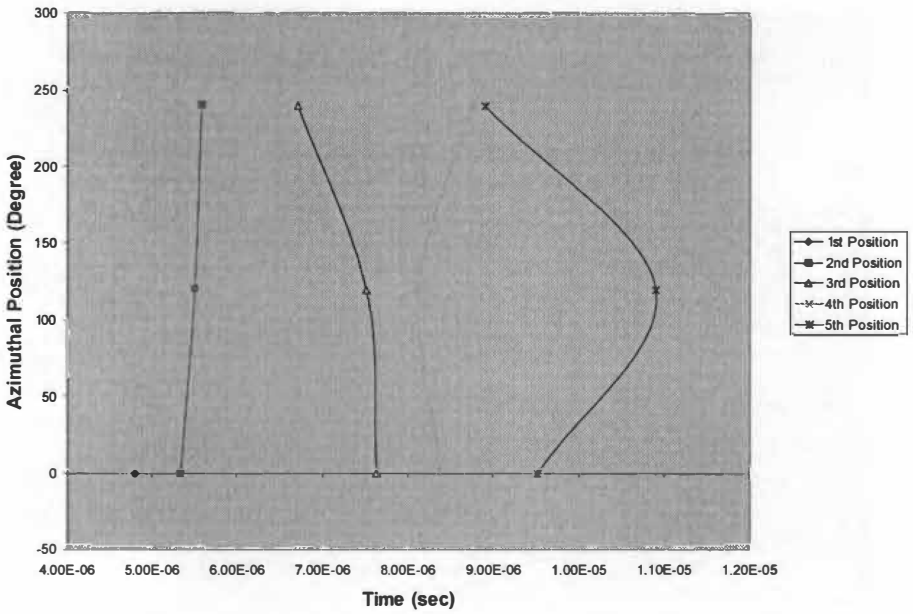


Figure 46: Azimuthal Position of the thruster vs. Time (Nov. 29, 2005)

not fire uniformly, it does indicate the location in the thruster that is closest to uniformity. This location is the second position (the first position downstream of the fuse disk) and has the most vertical of the three lines. As one progresses farther down the thruster curvier lines suggest that a non-uniform plasma was developing.

The apparent non-uniformity may be the result of difficulties in analyzing the less intense current peaks as the thruster exit is approached. This results in a lower current making the data harder to interpret. This situation can be seen in Figure 47, which is a graph of the current obtained from B-Dot probes 6-9 from Set 2. Looking at the first peak, the current is strongest at position 2 (pink line) and lowest at position 5 (purple line). Positions 3 (yellow line) and 4 (blue line) give currents in between the two, respectively. Another point to note from Figure 47 is that the B-Dot data, specifically in B-Dot probe 9 (pink line), give a current that is always negative or a always positive. The B-Dot data should give a current that is centered around the x-axis and oscillates between positive and negative values, such as in Figure 40. The constant negative current is not the result of eddy currents or some other phenomenon but is a result of the error involved in using numerical integration. A high-pass filter was used to help alleviate this problem, but since the filter was chosen to give optimum results for all the B-Dot probes and not just this particular B-

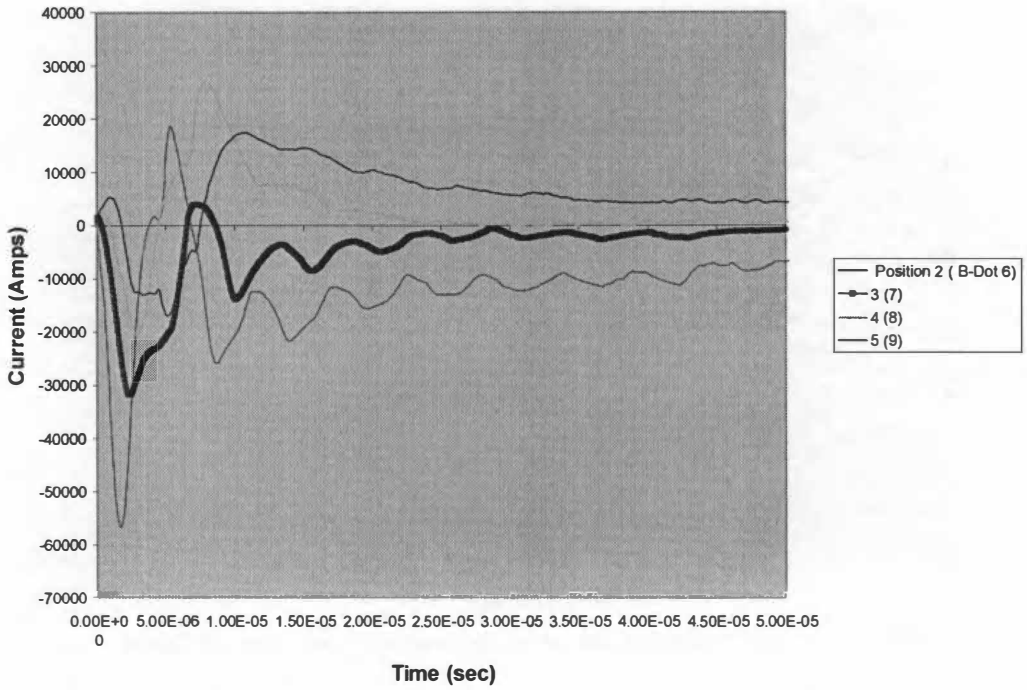


Figure 47: Current comparison for Set 2 (Nov. 29, 2005)

Dot probe, it gives the results seen in Figure 47. A constant filter was needed because if a different filter was used on each B-Dot, the time shift associated with using that filter would be different for each B-Dot. By using the same filter with the same constants, that time shift is the same for all the B-Dot probe data, minimizing this error.

The velocity data for Set 3 can be found from the position vs. time plot shown in Figure 48. The velocities of the peaks are the slopes of the curves (distance vs. time), which are shown in the linear regression equations (shown by each curve in the plot). By looking at the slope of the first line and then that of the subsequent lines from this graph the velocity starts out around 63 km /s and decreases with subsequent current peaks. The equation of the each line is in the form of $y = mx + b$ where m is the slope of the line. The equation of each line is shown above its respective line in the figure. Note that while data was found for all four positions (up to peak five in this case), this is not the case in every thruster run. For some cases only two points could be taken from the B-Dot graphs because close to the thruster exit (i.e. positions 4 and 5), it can sometimes be impossible to find a 3rd and 4th current peak. For the most part, graphs like that shown in Figure 48 do a good job of showing the velocity decrease with the current peak

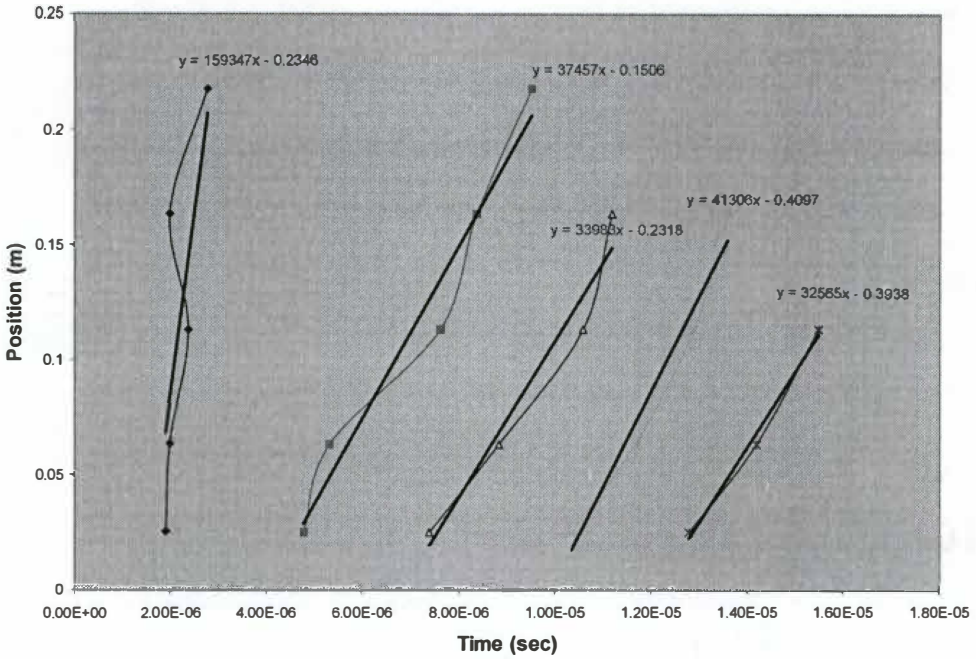


Figure 48: Velocity Data for Set 3 (Nov. 29, 2005)

number. This velocity decrease is likely caused by more plasma mass being carried down the thruster with each subsequent current pulse. When the thruster is first fired, a small amount of plasma is carried by the first current pulse, and as time progress, more plasma enters the electrode annulus to be swept away by the current. The lower the plasma mass that is carried with a current pulse, the faster the current pulse travels. If more peaks were added to the graph in Figure 48 it would likely show a further decrease in the velocity. This velocity decrease is similar for all of thruster runs. While initial values are not always equal the velocity tends to approach between 20 and 30 km/s around the 4^{th} peak.

In Figure 49 the velocity for each set are compared against one another. The velocity from Sets 2 and 3 slightly varies, but the slopes of the velocity vs. current peak # for these sets are similar. The velocity decrease discussed previously can be observed easily in this graph, with the velocity rapidly decreasing until it levels out around 25 km/s. Set 3 gives interesting results. The velocity starts at approximately 63 km/s, then decreases to 31 km/s, but then rises to 38 km/s before settling at 19 km/s. The velocity increase associated with peak 4 may be due to misinterpretation of the B-Dot data. When dealing with a small time scale (microseconds), a small shift in data could result in a very large swing in the

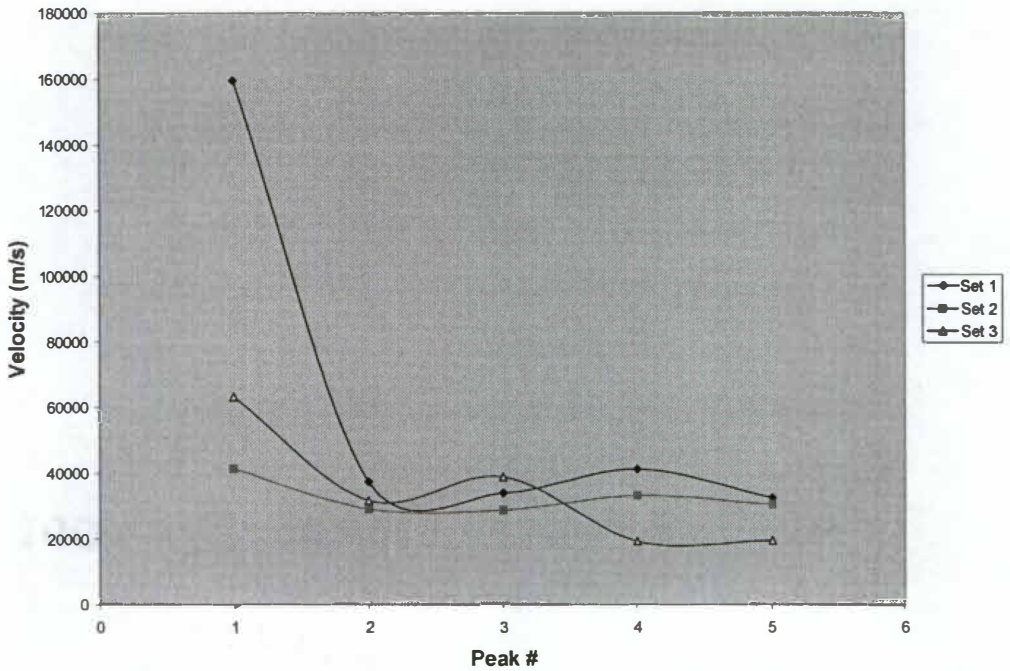


Figure 49: Velocity for all Three Sets (Nov. 29, 2005)

velocity data. Once again using multiple runs will help reduce this uncertainty. Another interesting observation to take from Figure 49 is the very large velocity for Set 1, when compared against the other two sets. Set 1 is located at the same azimuthal position as the trigger power supply hookup. When the current is released from the trigger capacitors, current will flow through Set 1 before reaching Sets 2 and 3. This may lead to a much larger current that propagates at a faster speed.

A photograph of a typical thruster firing is shown in Figure 50. While Figure 50 is not the picture taken during the thruster firing used in this discussion (the picture of this thruster firing did not develop properly), it is representative of most thruster firings (note that time progresses from bottom to top and from left to right for the frames in this photograph). Looking at the fourth frame (second frame from the left on the top row), the current starts on the right side (where Set 1 is located) and then travels around the thruster as time progresses. After the current has been evenly distributed the velocities should be closer together. This is the case realized in the B-Dot probe analysis (Figure 49) where by the second peak the three sets are grouped very close together. Again this is open to interpretation, but these trends may be confirmed through computer simulation.

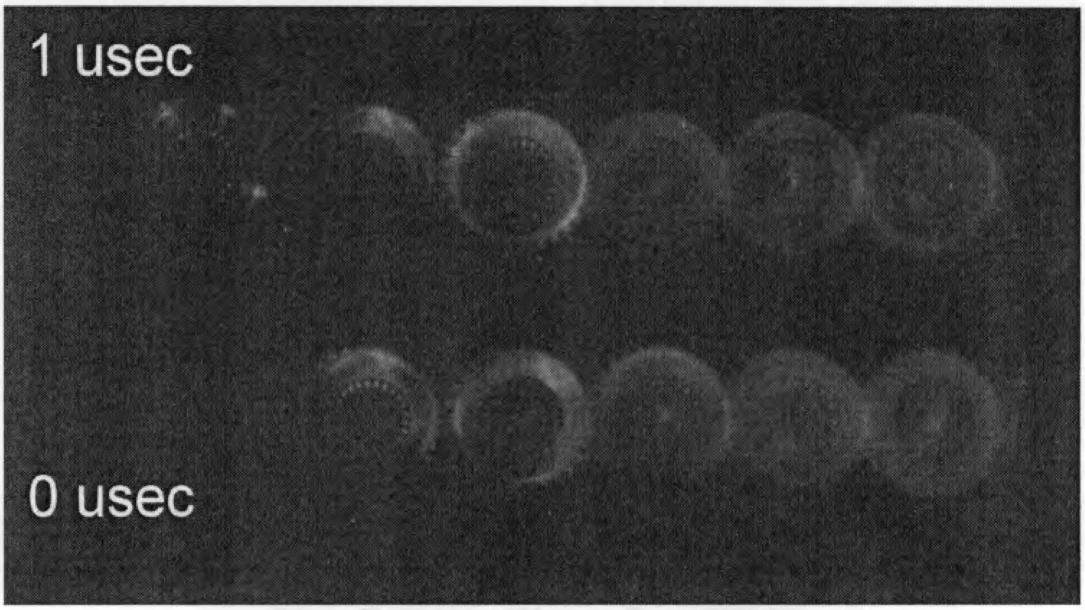


Figure 50: Picture of Thruster Firing (9/20/05).

These trends will be established by studying multiple thruster runs. B-Dot 1 is the B-Dot probe located before the fuse disk in position 1. This B-Dot probe records the current that goes into the thruster before it reaches the propellant. By comparing the B-Dot 1 data from multiple thruster runs one can determine whether the same current is going into the thruster for each run. Figure 51 shows that this very nearly the case. While one run does not show the exact same current as the others it is a very close comparison. In fact two of the runs, October 30 and September 7, give results that are difficult to distinguish from each other (Figure 51). By being able to hold values such as current entering the thruster constant from one run to the next a better comparison with computer simulations can be made. This is especially true for this case since B-Dot 1 can be accurately modeled using theory as shown in Figure 41.

An extremely important performance measurement for all propulsive thrusters is the propellant exit velocity. From exit velocity the specific impulse (Isp) can be found by dividing the exit velocity (in m/s) by the gravitational constant 9.81 m/s^2. While the exit velocity from a single run was found and discussed earlier in this chapter, it is important to compare exit velocities from multiple thruster runs to see if the thruster is producing similar velocities realized at axial position 5. Figure 52 compares the velocities associated with Set 1 of three different runs taken on September 7, September 20, and November 29, 2005. While not exact matches, the exit velocities for the various runs are very similar to one another. The first

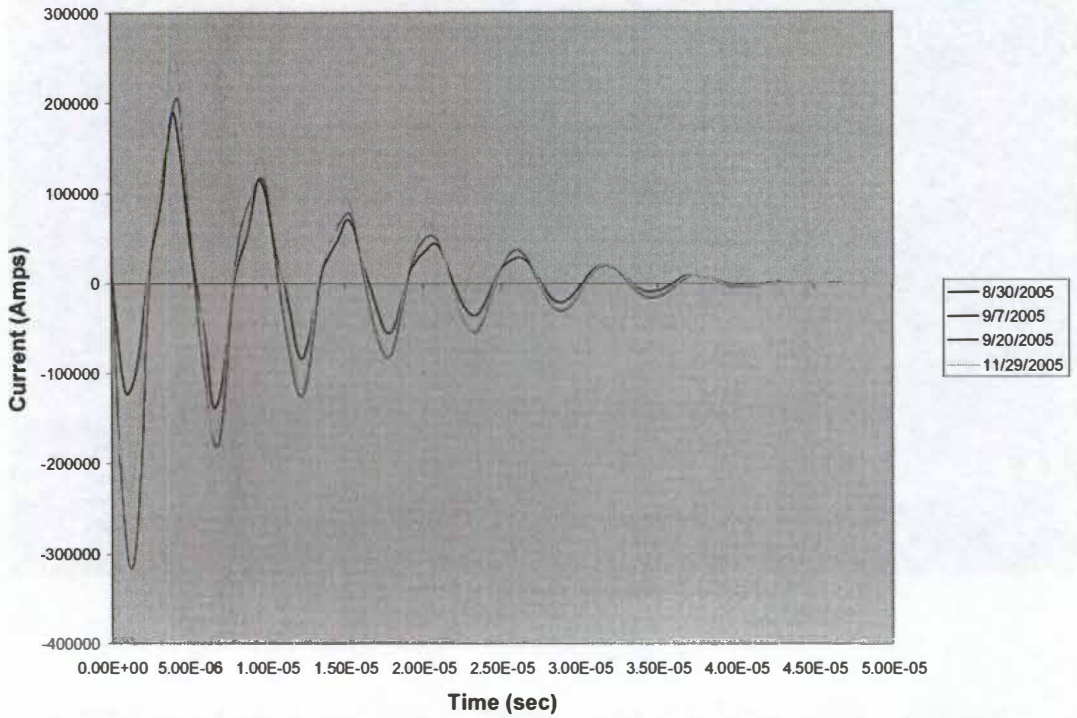


Figure 51: Comparison of Integrated B-Dot 1 Data for Multiple Thruster Runs

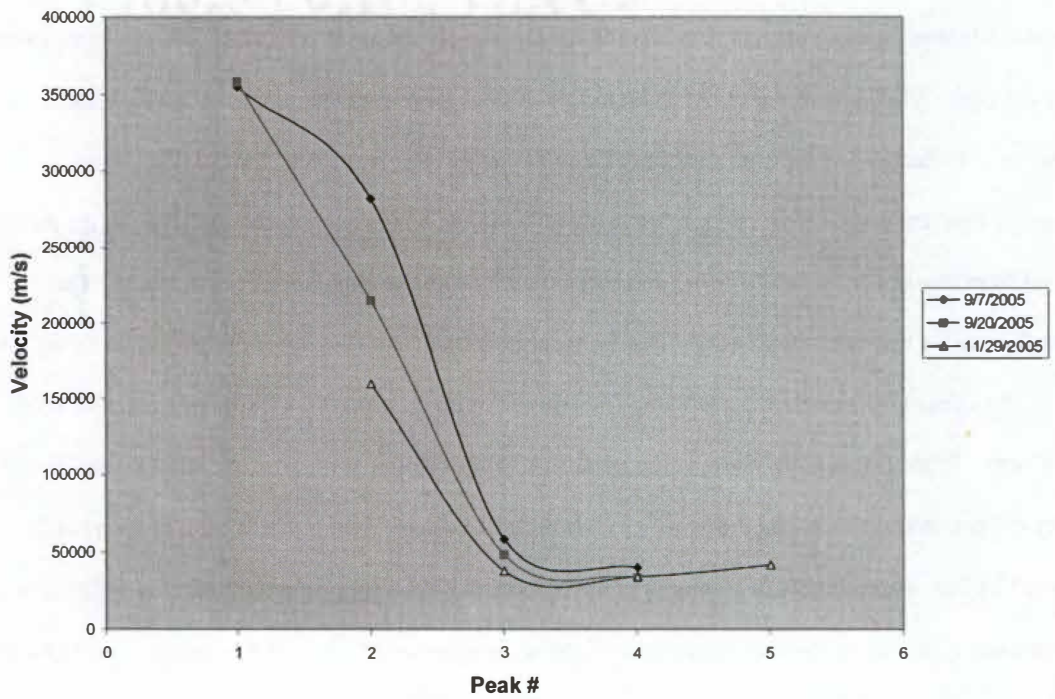


Figure 52: Current Sheet Velocity for Multiple Thruster Runs

two current peaks have a greater variation than the last two peaks, which are within 20 km/s of each other for peak 3 and within 10km/s for the last peak. For the run on November 29 (yellow line) the first peak was not found because of noisy data that presumably results from electronic interference with the commencement of current flow in the main capacitor (as seen in Figure 35). Therefore it was thought that this would not give an accurate representation of the velocity at this time in the thruster discharge. A curve could be fit to the lines in Figure 52 to describe the velocity over time, if the computer simulations would call for it. The corresponding values for Isp began at around 35,000 seconds but then drops drastically to level out between 2500 seconds and 4000 seconds. The very high initial Isp values are not representative of the thrusters actual Isp. The high initial Isp values are due to minimal plasma propellant traveling along with the current for early peaks. The Isp values for peaks 3, 4, and 5 are better representations of the mass average specific impulse. Initial computer simulation runs using MACH2 give an Isp of approximately 10,000 seconds for the first peak and drops significantly for subsequent peaks. The amplitude of the first predicted peak is about 3.5 times that realized in the experiments, but the same trends are seen.

iii. Laser Interferometer Data Analysis

The last of the data to be analyzed was provided by the laser interferometer. Direct comparison of the experimental data with computer simulation results is pretty straight forward for this physical variable. The raw data (Figure 36) was processed using two computer programs written by Smith [16]. The first program was designed to perform a phase demodulation of the signal from the laser interferometer. The program required, as inputs, the interferometer signal, frequency filter, and carrier frequency, and then outputs the phase shift data (Figure 53). The filter [16] was a low-pass filter based on a cut-off frequency of 250 MHz. The second program was designed to give the electron number density. It required the interferometer signal, filter (same as the one used in the first program), and a phase-to-density conversion factor (5.60654E+20 1/radians-m^2) determined by the type of laser [16] used to illuminate the plasma. This program worked by finding a reference sinusoidal signal from which it extracted the carrier frequency and the phase-shifted data found from the previous program, and outputs the line of sight electron number

density (Figure 54). It has been found that this plot is representative of that seen in other runs, suggesting a reasonable degree of repeatability.

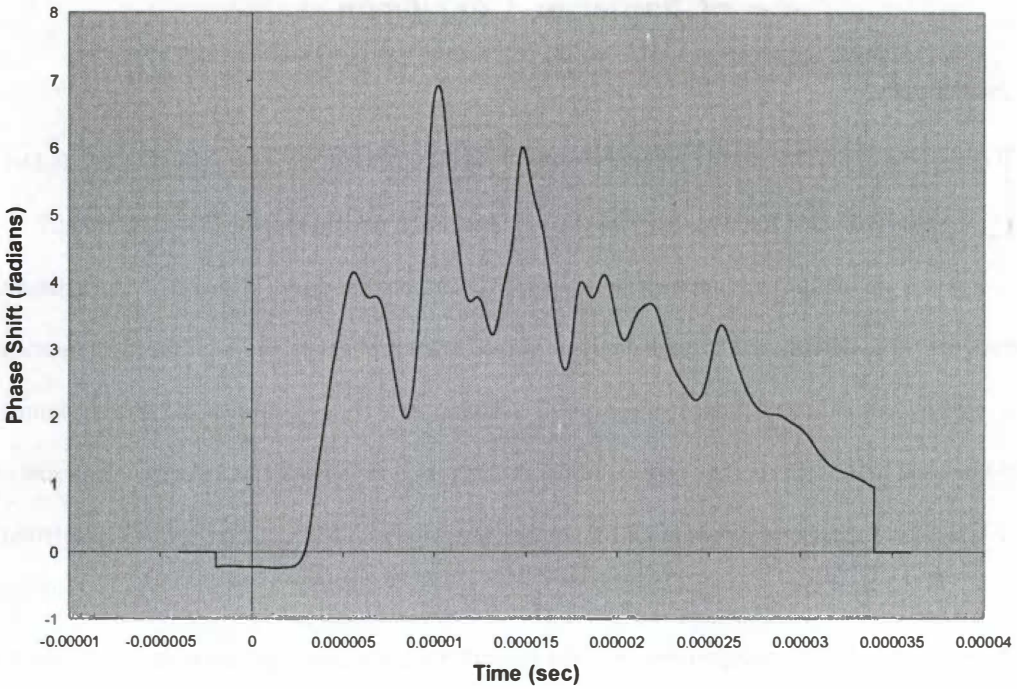


Figure 53: Interferometer Phase Shift Data (July 1 , 2005)

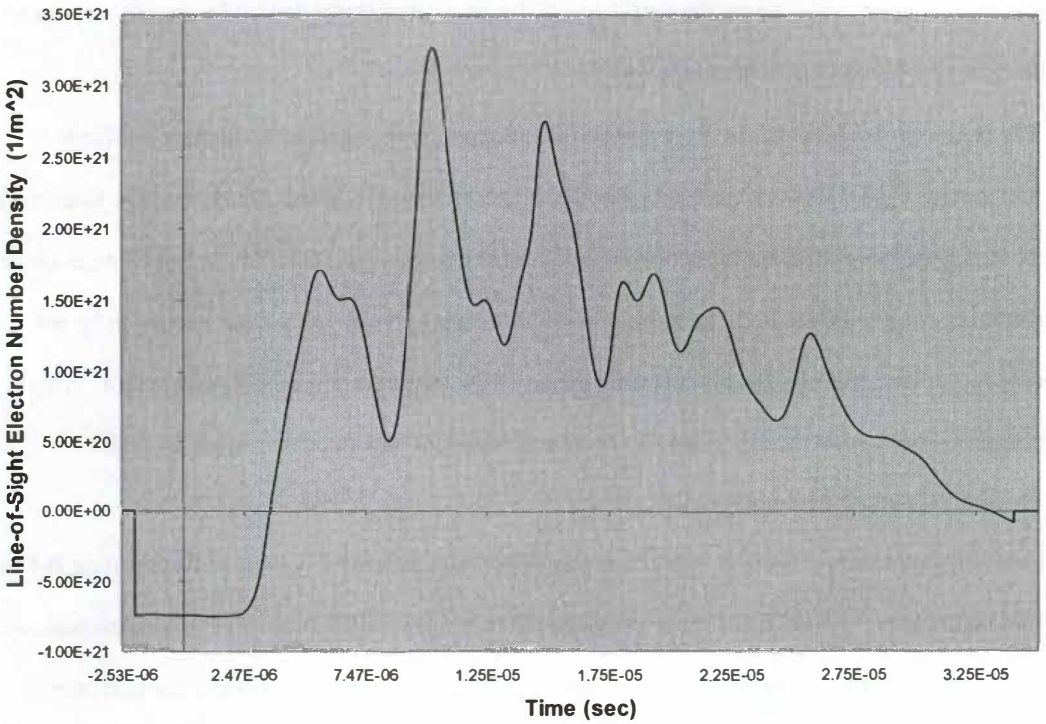


Figure 54: Electron Number Density taken from Interferometer (July 1, 2005)

Chapter 6: Conclusion

a. Summary

Through an extensive study of the laboratory Pulsed Plasma Accelerator using thirteen B-Dot probes, a laser interferometer, and two Rogowski coils, it is fairly evident that the 2D, axisymmetric MACH2 computer simulation will not be able to completely model this specific thruster. The azimuthal asymmetries that were determined through analysis of the B-Dot probe data and high speed photography precludes reliable detailed simulations using any 2-D axisymmetric code. However, a 2-D axisymmetric code might be used to describe certain aspects of the thruster such as Isp and exit velocity. Data analyzed in this thesis will provide useful information for comparison with both MACH2 and GEMS simulation results.

In order to make any comparisons with the computer simulations, a proper method was needed to analyze the experimental data. The laser interferometer was fairly easy to analyze because of the use of excellent computer-based analysis programs written by Smith [30]. Once the correct digital filter was selected it was just a matter of running the data through the program. This data will be directly compared against future MACH2 and GEMS simulation runs.

The B-Dot probe data and the Rogowski coil data prove to be a greater challenge. Multiple methods and various digital filters were used to create the best method to analyze the data. The Rogowski coil data needed to be integrated, multiplied by an integration constant, and then put through a digital high-pass filter in order for it to be studied. In addition to all those steps, the B-Dot probes needed to be put through a median filter before integration to eliminate any high frequency noise that was present. All of this was necessary to interpret the B-Dot probes and Rogowski coil data to provide data for future comparison with the computer simulations.

Once this process had been completed, it was shown that the current obtained from certain B-Dot probes could be modeled. By using a simple circuit analysis and Kirchoff's laws, a very good estimate of the current that passes B-Dot probe 1 was made. Since the MACH2 simulation will use the exact same equation and constants determined in this theoretical analysis, MACH2 can simulate the current as well as shown in Figure 41. It was also shown that, except B-Dot probe 1, all the other B-Dot probes cannot be

accurately modeled using this method, presumably due to time varying plasma conditions that are not azimuthally uniform. This strengthens the case for the development of a fully three-dimensional simulation code, such as the GEMS computer simulation code.

Additionally, by studying the B-Dot probe data and the exit velocity of the thruster for different runs, it was shown that the thruster experiment is reasonably repeatable, giving similar current sheet velocity trends for different runs. Repeatability is probably the most important factor when trying to model any experimental set-up with a computer simulation. Without repeatability reliable comparisons with computer simulation are not possible.

Finally, the Isp for the thruster was found to start out at around 32,000 seconds after the main capacitor was fired and then level off between 2500 and 4000 seconds which is a better representation of the mass averaged specific impulse. This compares favorably with preliminary MACH2 simulation results. While it has been shown (Figure 51, Figure 52) that certain aspects (such as current flowing past B-Dot 1, exit velocity, electron number density, and Isp) have shown repeatability others, such as the B-Dot probes 2-13, have not. They tend to vary greatly from one thruster firing to the next. However, the overall characteristics of B-Dot probes 2-13 (Isp, exit velocity) tend to show similar results.

b. Recommendations

First and foremost, once the MACH2 computer simulation is complete, an in depth comparison of the simulated and experimental B-Dot probes and the laser interferometer data needs to be made. This comparison will guide modifications to the simulation codes, as necessary. Since MACH2 will not accurately model the 3-D plasma in the thruster, comparisons with the GEMS computer simulation must be made. But until GEMS is finished, the thruster can still continue to contribute to improving the MACH2 simulations. While resistance, impedance, and the current for B-Dot 1 have all been used to help develop MACH2 circuit models, other values such as current sheet velocity, Isp, and line of sight electron number densities can all be compared with simulation results. An area in which better data is required is near the thruster exit. However, additional instruments may need to be added to the thruster setup in order to

achieve this. Continued operation of the thruster and comparisons with the computer simulation will contribute to the development of a more accurate simulation code.

There are also improvements that can be made to the thruster set-up to help obtain additional and more accurate data from the thruster. By adding B-Dot probes to the inner electrode, a more complete analysis of the current sheet can be made. Currently B-Dot probes are only located on the outer electrode, and it has been seen in similar experiments that the plasma travels faster on one electrode than on the other. By placing B-Dot probes on the inner electrode this could be recorded for the PPA thruster.

Since it has been established that the line-of-sight electron number density at the thruster exit does not vary temporally greatly from one run to the next, the laser interferometer could be used as another way to find the plasma velocity at the thruster exit. By moving the laser interferometer farther downstream and determining the additional time it takes one number density peak to register at the new location compared to that at the original position, velocity can be determined. Lastly a spectrometer could be utilized to record spectral data from which the electron temperature and the plasma species concentration might be obtained. This would provide additional information for comparison with MACH2 and GEMS simulations, as well as to guide the development and validation of the GEMS simulation. Once again the more information the computer simulations have on the thruster the more accurately these simulations will be.

References/Bibliography

References/Bibliography

1. Office of Space and Defense Power System. 6 June 2004. Dept. of Energy. 21 Mar. 2005 <http://www.ne.doe.gov/space/space-desc.html>.

2. Keefer, Dennis R., Trevor Moeller, and Joel W. Muehlhauser. "Research Support for Nuclear Fission Electrical Power and Propulsion." Task 03-01, Contract Number: F40600-00-D-0001.

3. Keefer, Dennis, and Robert Rhodes. "Numerical Simulation of Cableguns Using MACH2." *IEEE Transactions on Plasma Science,* vol. 31 pp.248-255, April 2003.

4. Smith, J. M., Dennis Keefer and Newton Wright, "Interferometric Investigation of a Cablegun Plasma Injector," *IEEE Trans. Plasma Science,* vol. 28, pp. 2272-2275, Dec 2000.

5. Keefer, Dennis and Robert Rhodes. MACH2 Simulation of an Electrothermal Gun. IEEE. International Pulsed Power Conference. Monterey, CA. June 1999.

6. Choueiri, Edgar Y., and Robert G. Jahn. "Electric Propulsion." Encyclopedia of Physical Science and Technology. 5 vols. New York: Academic P, 2002.

7. Hrbud, Ivana. Electric Thrusters. NASA MSFC. NEP Tutorial. Huntsville, AL.

8. Martinez-Sanchez, M., and J.E. Pollard. "Spacecraft Electric Propulsion-An Overview." Journal of Propulsion and Power Vol. 14, No. 5 (1998): 688-699.

9. Dunning, John W., et al. "An Overview of Electric Propulsion Activities at NASA." Joint Propulsion Conference, AIAA-2004-3328, Ft. Lauderdale, FL, July 11-14, 2004.

10. Kamhawi, H., Turchi, P.J, and Leiweke, R.J. "Design and Operation of a Laboratory Bench-Mark PPT." Joint Propulsion Conference, AIAA 96-2732, Lake Buena Vista, FL, July 1-3, 1996.

11. Elliott, Frederick W., et al. "An Overview of the High Power Electric Propulsion (HiPEP) Project." Joint Propulsion Conference, AIAA-2004-3453, Ft. Lauderdale, FL, July 11-14, 2004.

12. Oleson, Steven R., "Electric Propulsion Technology Development for the Jupiter Icy Moons Orbiter Project." Joint Propulsion Conference, AIAA-2004-3449, Ft. Lauderdale, FL, July 11-14, 2004.

13. Keefer, Dennis R., Trevor Moeller. "Quarterly Report for Task 03-01." 07/01/04-09/30/04.

14. Keefer, Dennis R., Trevor Moeller. "Quarterly Report for Task 03-01." 10/01/04-12/31/04.

15. Burden, Richard L., and J D. Faires. Numerical Analysis. 7th ed. Pacific Groove: Brooks/Cole, 2001.

16. Smith, L. Montgomery. Personal Communication. Mar. 2005-Dec. 2005.

17. Hutchinson, I H. Principles of Plasma Diagnostics. 2nd ed. Cambridge, U.K.: Cambridge UP, 2002. 11-45.

18. Electric Propulsion. Seminar at NSSTC. Feb. 2002.

19. Jahn, Robert G. Physics pf Electric Propulsion. New York: McGraw-Hill Book Company, 1968.

20. Stratton, Julius A. Electromagnetic Theory. New York: McGraw-Hill Book Company, 1941.

21. Lochte-Holtgreven, W, ed. Plasma Diagnostics. Amsterdam: North-Holland Company, 1968.

22. Lorrain, Paul, Dale R. Corson, and Francois Lorrain. Electromagnetic Fields and Waves. 3rd ed. New York: W. H. Freeman and Company, 1988.

23. Winch, Ralph P. Electricity and Magnetism. 2ndnd ed. Englewood Cliffs: Prentice-Hall, 1963.

24. Holt, E. H., and R. E. Haskell. Foundations of Plasma Dynamics. New York: The Macmillan Company, 1965.

25. Smith, Paul W. Transient Electronics. 1st ed. West Sussex: John Wiley & Sons Ltd., 2002.

26. Hoskins, W. Andrew, Michael J. Wilson, Michael J. Willey, and Nicole J. Meckel. "PPT Development Efforts at Primex Aerospace Company." AIAA 99-2291, 1999.

27. Burton, R L., and P J. Turchi. "Pulsed Plasma Thruster." Journal of Propulsion and Power 14 (1998): 716-735.

28. Eom, G S., G C. Kwon, I D. Bae, G Cho, and W Choe. "Heterodyne Wave Number Measurement Using a Double B-Dot Probe." Review of Scientific Instruments 72 (2001): 410-412.

29. Piejak, R, V Godyak, and B Alexandrovich. "The Electric Field and Current Density in a Low-Pressure Inductive Discharge Measured with Different B-Dot Probes." Journal of Applied Physics 81 (1997): 3416-3421.

30. Moeller, T, D Keefer, B Rhodes, et al. "Comparison of Experimental and Computational Simulations Results of a Pulsed Plasma Accelerator." International Electric Propulsion Conference, IEPC-2005-008, Princeton University, Oct. 31-Nov. 4, 2005.

Appendix A

Appendix A

a. Maxwell's Equations

Electromagnetic theory is based on four experimental equations known as Maxwell's equations. Maxwell's equations [20], together with some set of boundary conditions describe how electric and magnetic fields interact and behave. While entire books have been devoted to this subject, a brief overview of the four equations will be given here for background purposes. In order to obtain a more complete feel for the subject please consult [20-22]. The Maxwell Equations in differential form based on the assumptions that the fields penetrate magnetic and/or polarizable media in SI units are as follows:

$$\nabla \times \mathbf{H} = \mathbf{J} + \dot{\mathbf{D}}$$
Equation 17

$$\nabla \times \mathbf{E} = -\dot{\mathbf{B}}$$
Equation 18

$$\nabla \cdot \mathbf{B} = 0$$
Equation 19

$$\nabla \cdot \mathbf{D} = \eta$$
Equation 20

Equation 17 is know as Ampere's Law and Equation 18 is known as Faraday's Law; both will be discussed in greater detail in Sections i and ii, respectively.

Equation 19 implies that the magnetic monopoles are nonexistent [23]. For a closed surface the magnetic flux directed inward towards the South Pole will equal the flux outward from the North Pole [23]. This results in a net magnetic flux of zero. This will always be the case for dipole sources [23]. Equation 20 relates the divergence of **E** to the charge density; also known as Gauss's Law. This simply states that the electric flux, η, out of any closed surface is proportional to the total charge enclosed within the surface [23]. Gauss Law is to electricity as Ampere's Law is to magnetism (please refer to the following section).

i. Ampere's Law

In order for current to flow in this experiment, one must create a complete circuit; with this current a magnetic flux density **B** at some point, P, shows up in the neighborhood of the circuit [23]. In other

words when a current, I, flows there is a magnetic field created by that current that is located around the circuit. For the case of the PPA lab prototype studied in this thesis, the two electrodes connected to the capacitor create a complete circuit when plasma is present in the annular region (see Chapter 3, Figure 13, for the description of the lab prototype PPA). Ampere's Law relates the change in the magnetic flux dB at a point P to the current flowing through this point over a length of circuit, dl. Ampere's Law deals with both the magnitude and direction of the change in the magnetic field. The magnitude will be considered first. Relating dB to the current, I, just in magnitude, it can be shown:

$$dB = \mu_o I dl(\sin\theta)/4\pi r^2$$

Equation 21

where r is the distance from dl to P, μ_o is the permeability of free space valued at $4\pi X10^{-7}$ W/A-m, and θ is the angle between dl and r.

Note that dB in the above equation is just a scalar. When the direction is incorporated, d**B** becomes a vector. For specific details refer to [20, 21]. Ampere's Law states that the direction of the magnetic field is perpendicular to the plane determined by dl and r; this can be seen visually using the right hand rule. Ampere's Law results in a magnetic flux density with both magnitude and direction:

$$d\mathbf{B} = \mu_o I d\mathbf{l} \times B\mathbf{i}_r / 4\pi r^2$$

Equation 22

where $\mathbf{i}_r$ is the unit vector pointing in the direction of the increasing r.

ii. Faraday's Law

Faraday's Law deals with induced electromagnetic force (emf). Winch [23] describes Faraday's Law with four statements:

1. *Whenever a conductor moves across a magnetic flux or visa versa the magnetic flux through a circuit changes and emf is induced.*
2. *The emf last only during the change.*
3. *The induced emf is proportional to the rate of change of the number of magnetic flux lines.*
4. *The induced emf is such as to oppose the change that is produced Lenz's Law.*

This last statement, Lenz's Law, is particularly important when discussing the operation of the thruster. It will be discussed in greater detail in the next section of this chapter. Getting back to Faraday's Law and combining these statements into a mathematical expression yields:

$$e = -N\frac{d\phi}{dt}$$

Equation 23

where e is the induced emf given in volts, φ is the number of magnetic flux lines through the circuit, and N is the number of single turns of wire, (for the experiment in this thesis it refers to the turns of wire in the B-Dot probe). The integral form of Faraday's Law is given by:

$$\oint E\cos\theta dl = -\int_A [d(B\cos\alpha)/dt]dA$$

Equation 24

where E is the electric field intensity, A is the area enclosed by the circuit, and α is the angle between B and the normal to the plane of the circuit. Once again for additional details on this subject please refer to [20-22]. Now E is a result of the changing magnetic flux and is not an electrostatic field intensity. The line integral of $E \cdot dl$ around any closed path is equal to the negative of the change in the magnetic flux through the surface bounded by the closed path [19]. In order to express the line integral in terms of $\mathbf{E} \cdot d\mathbf{s}$ around a closed path one must consider an imaginary closed path and not a conducting circuit. Winch states *this assumption is allowed because the electric field intensity due to a changing magnetic flux exists whether the conduction circuit is present or not, since its existence does not depend on the presence of moving charges* [23]. So Equation 24 now becomes:

$$\oint \mathbf{E} \cdot d\mathbf{s} = -\int_A \frac{d\mathbf{B}}{dt} \cdot d\mathbf{A}$$

Equation 25

Equation 25 accounts for the rate of change of **B,** whether it is change of magnitude, direction, or both [19].

Appendix B

Appendix B

Below is a complete analysis of the data taken from the November 29, 2005 thruster run. All other thruster runs were analyzed in the same way.

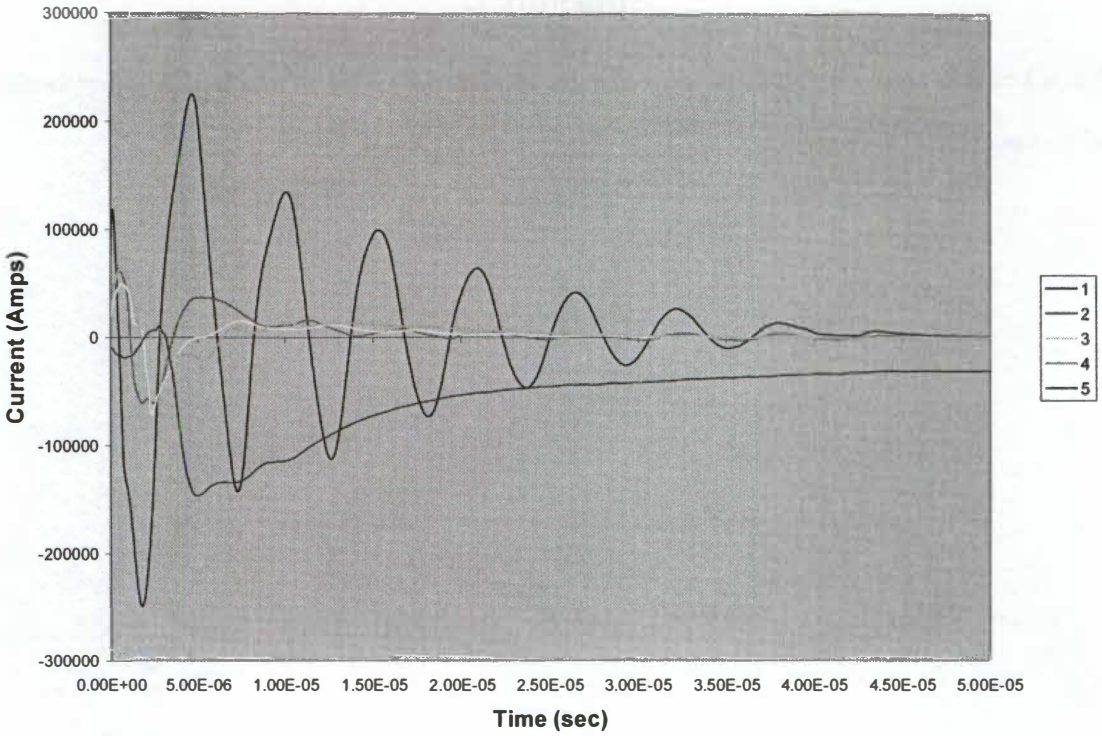


Figure 55: Set 1 B-Dot Integration

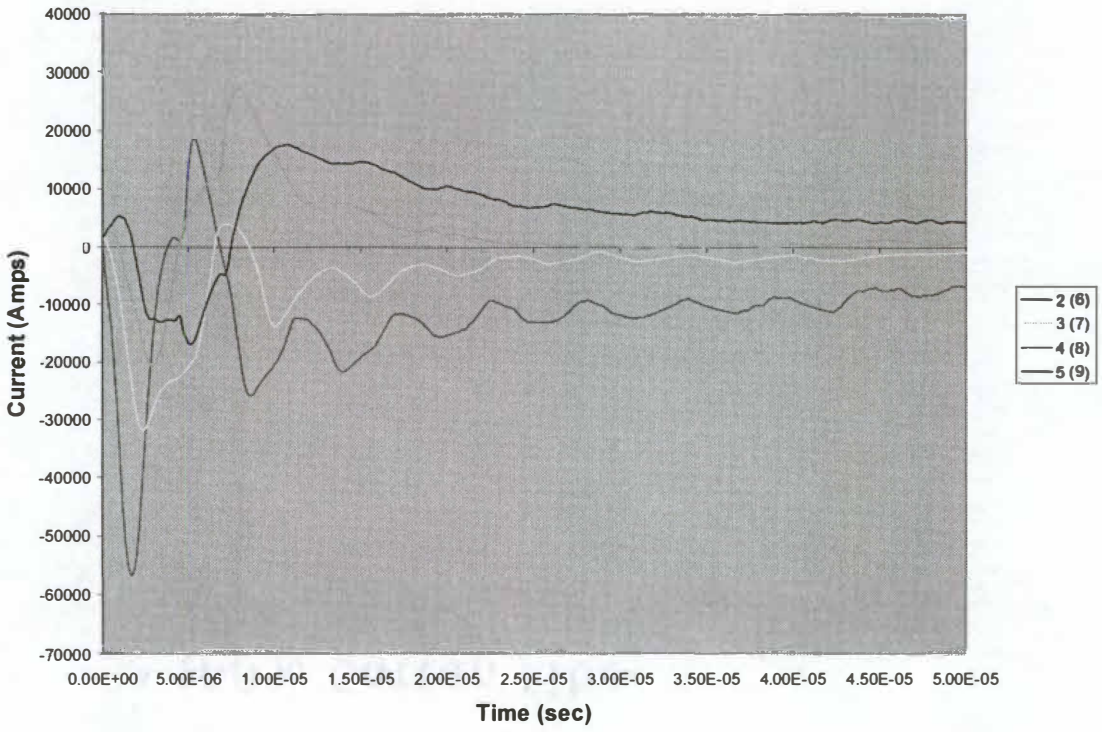


Figure 56: Set 2 B-Dot Integration

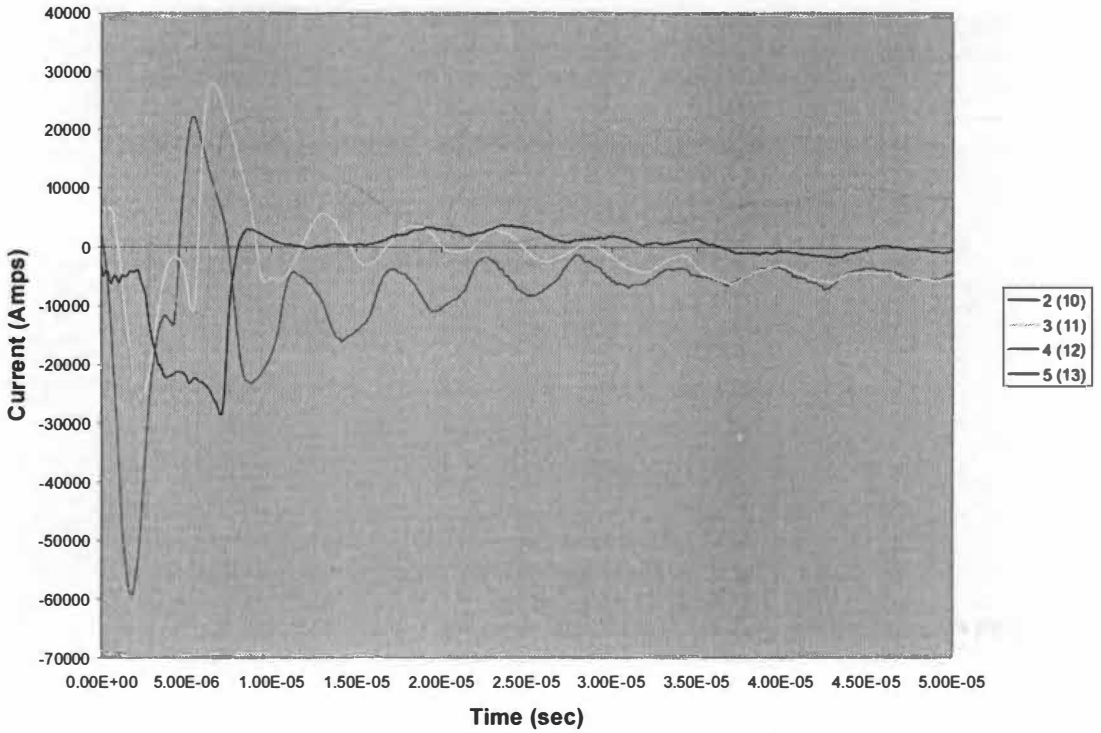


Figure 57: Set 3 B-Dot Integration

Table 7: B-Dot Peak Analysis

B-Dot #	Azimuthal Pos	Position #	Distance (m) from Capacitor	Peak # 1	2	3	4	5	6	7	
1	0	1	0.0254	1.90E-06	4.80E-06	7.40E-06	1.03E-05	1.28E-05	1.57E-05	1.83E-05	
2	0	2	0.063495	1.98E-06	5.34E-06	8.85E-06	1.17E-05	1.42E-05	1.69E-05	1.95E-05	
3	0	3	0.113495	2.38E-06	7.63E-06	1.06E-05	1.29E-05	1.55E-05	1.74E-05	2.03E-05	Set 1
4	0	4	0.163495	1.99E-06	8.39E-06	1.12E-05	1.36E-05				
5	0	5	0.217465	2.77E-06	9.52E-06						
6	120	2	0.063495	1.80E-06	5.50E-06	8.90E-06	1.16E-05	1.42E-05	1.74E-05	2.00E-05	
7	120	3	0.113495	2.61E-06	7.51E-06	1.03E-05	1.36E-05	1.58E-05	1.88E-05	2.09E-05	Set 2
8	120	4	0.163495	3.12E-06	8.12E-06	1.21E-05	1.51E-05	1.79E-05			
9	120	5	0.217465	5.35E-06	1.09E-05	1.41E-05	1.61E-05	1.90E-05			
10	240	2	0.063495	1.88E-06	5.58E-06	8.89E-06	1.15E-05	1.43E-05	1.74E-05	1.98E-05	
11	240	3	0.113495	2.51E-06	6.71E-06	1.03E-05	1.33E-05	1.58E-05	1.85E-05	2.12E-05	Set 3
12	240	4	0.163495	2.35E-06	8.75E-06	1.29E-05	1.52E-05	1.79E-05			
13	240	5	0.217465	4.01E-06	8.91E-06	1.25E-05	1.93E-05	2.19E-05			

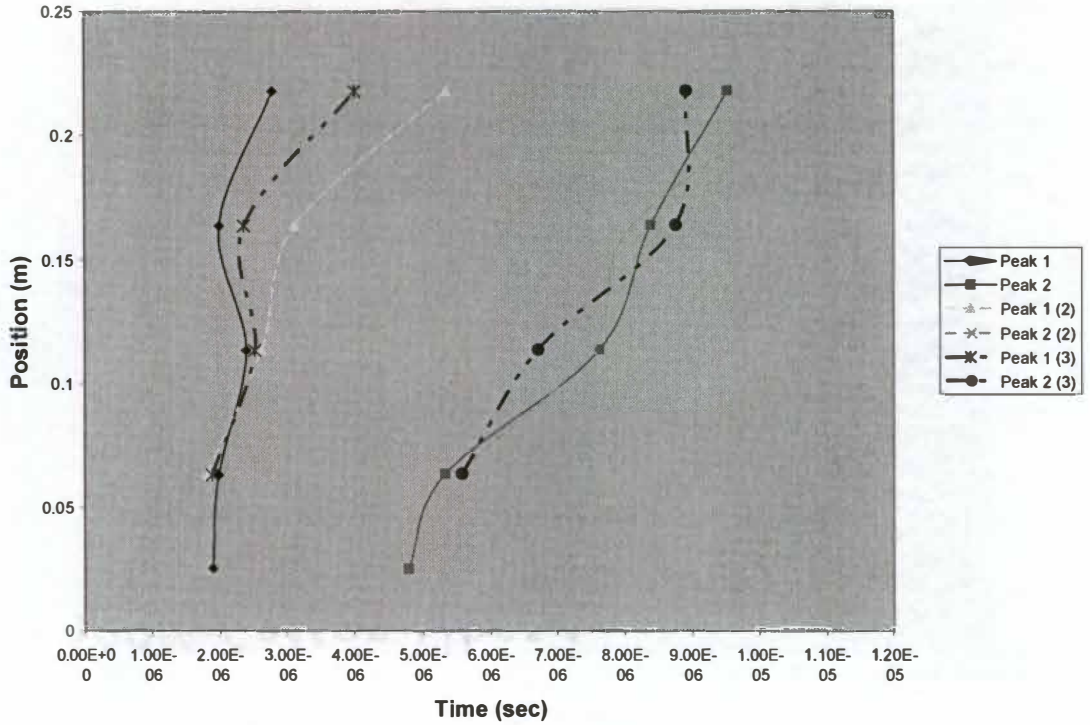


Figure 58: B-Dot Peak Position vs. Time (for Peaks 1 & 2)

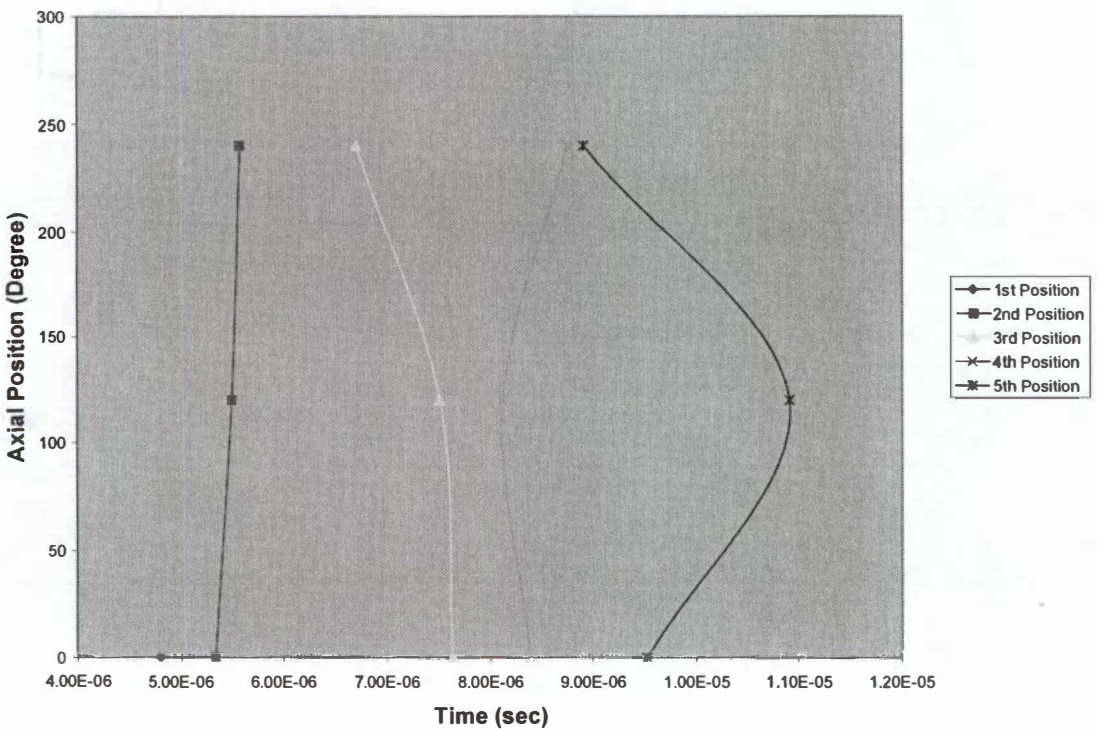


Figure 59: B-Dot Axial Position vs. Time (Peak 1)

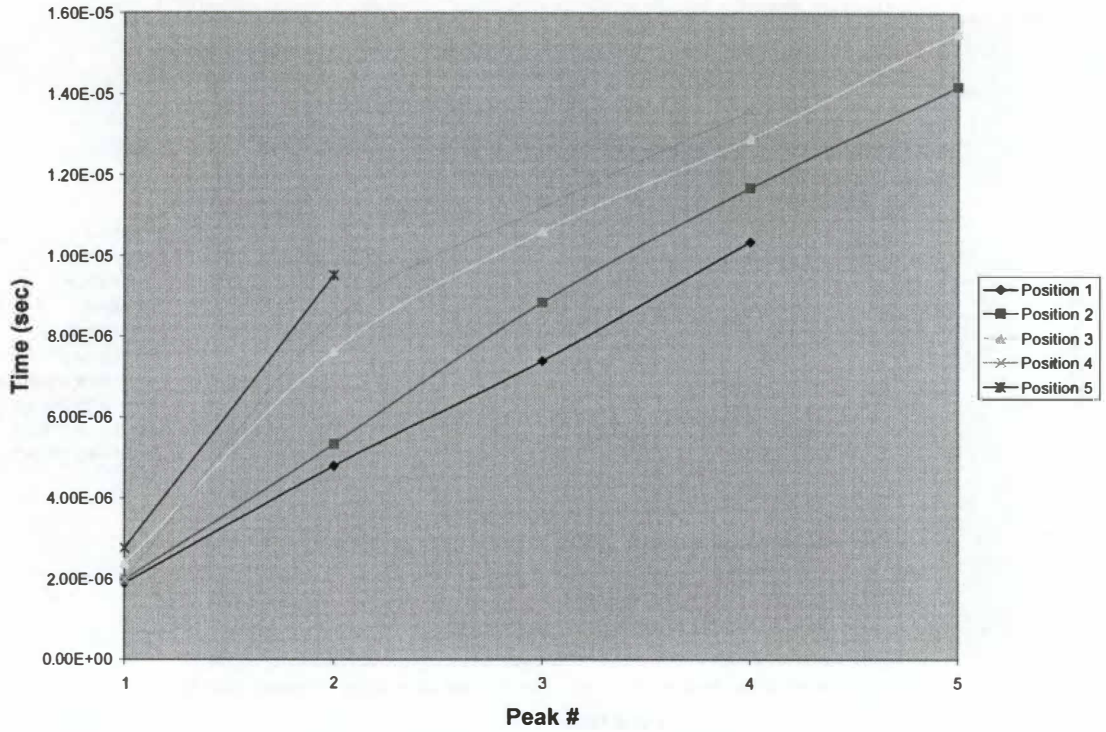


Figure 60: Time vs. B-Dot Peak # (Set 1)

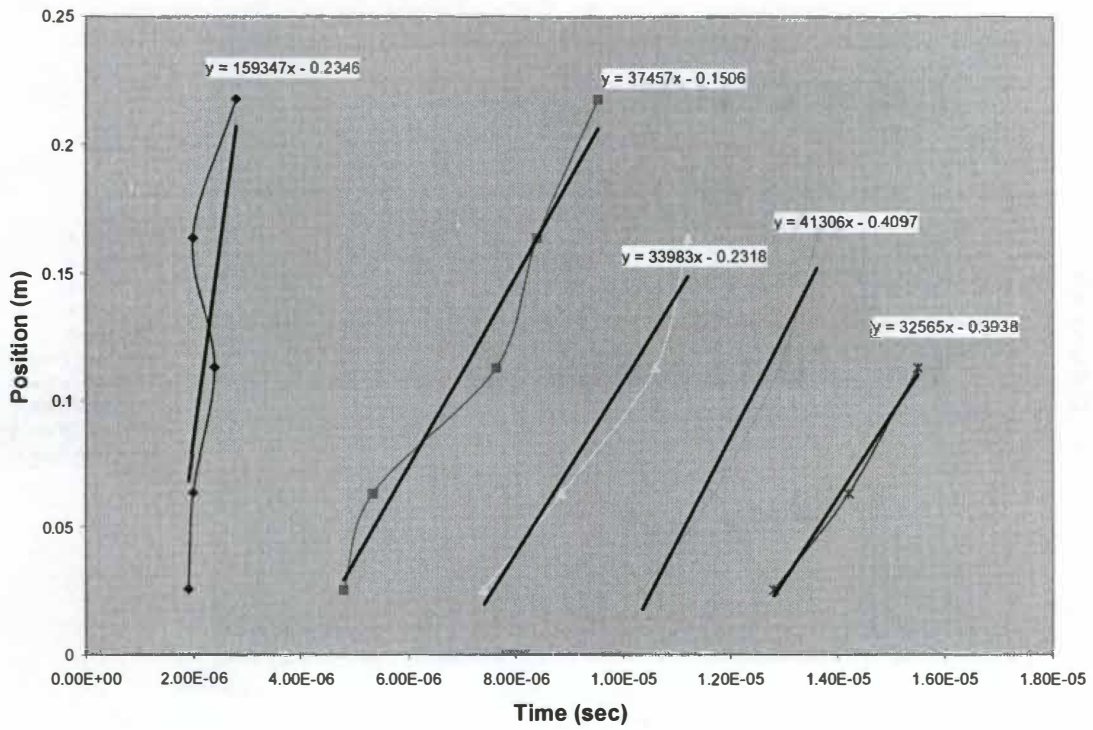


Figure 61: B-Dot Peak Analysis (Set 1)

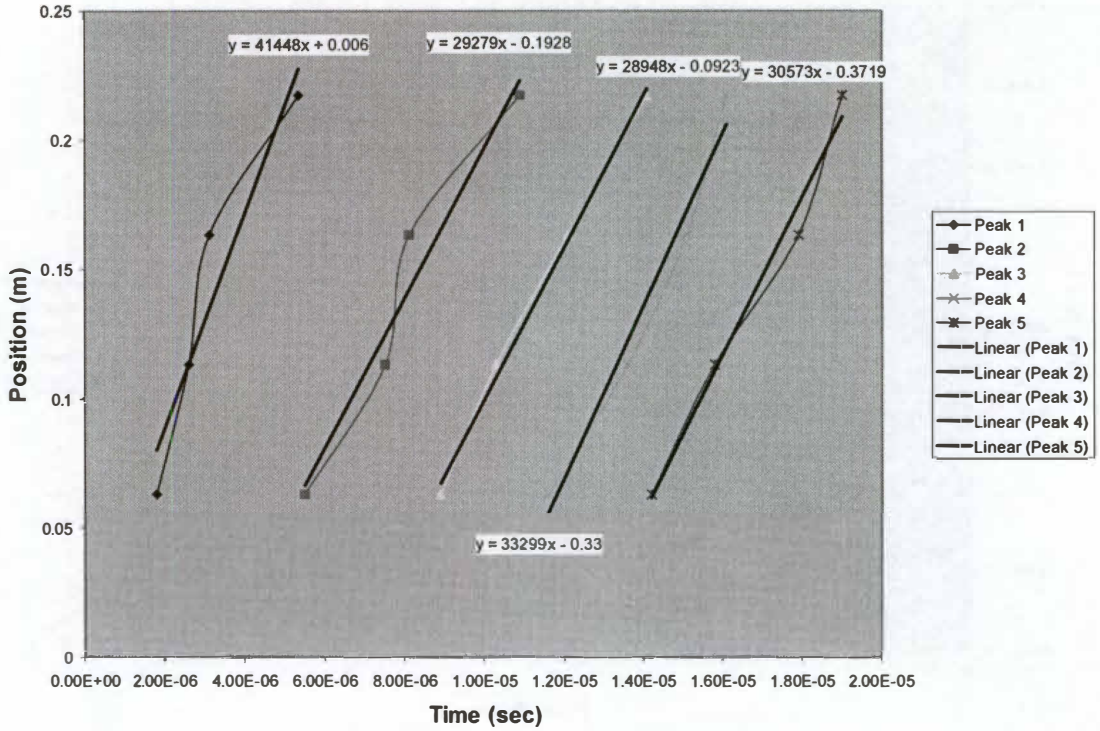


Figure 62: B-Dot Peak Analysis (Set 2)

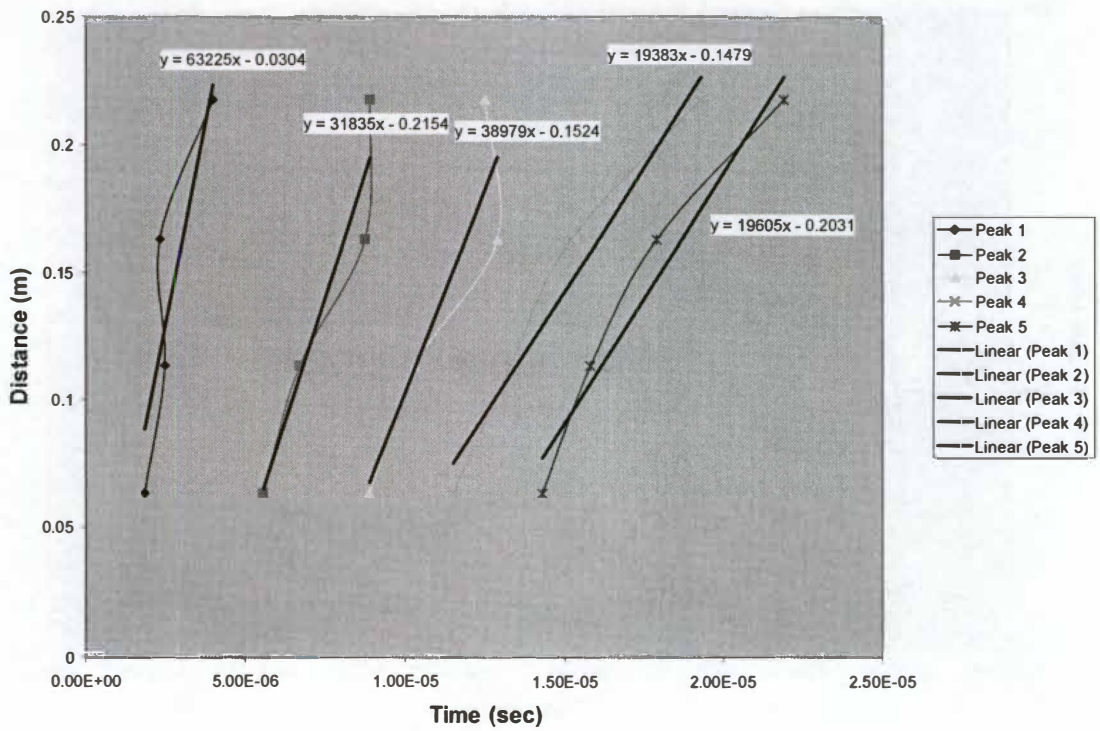


Figure 63: B-Dot Peak Analysis (Set 3)

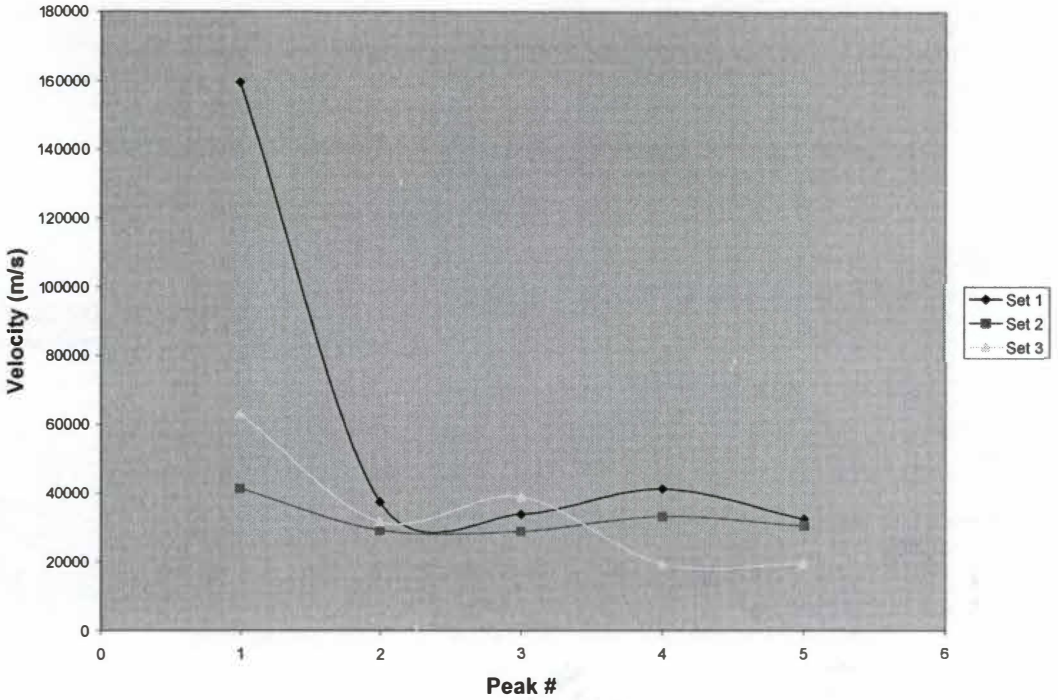


Figure 64: Magnetic Field Velocity vs. Time (B-Dot)

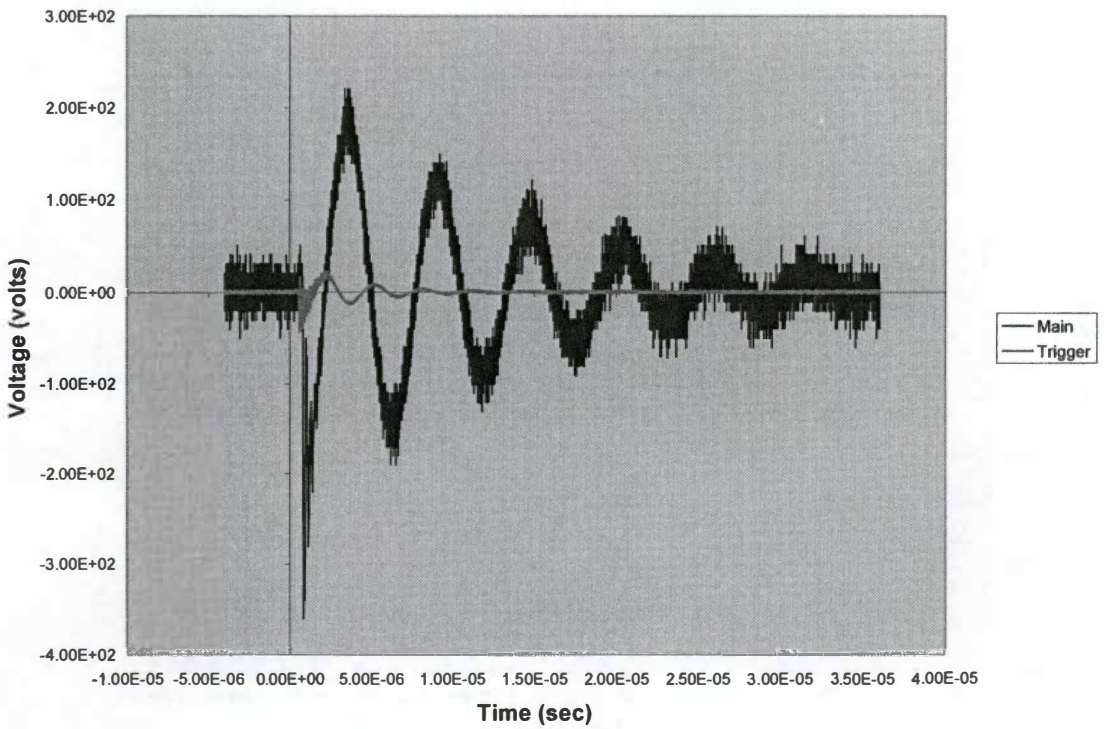


Figure 65: Raw Rogowski Coil Data

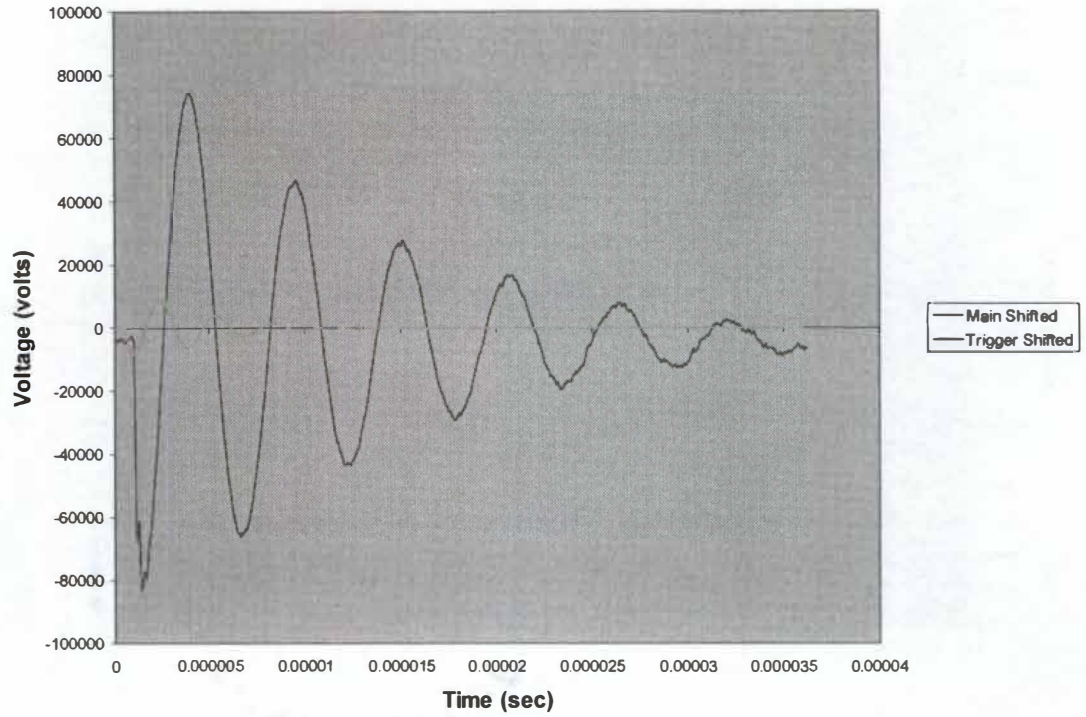


Figure 66: Integrated Rogowski Coil Data

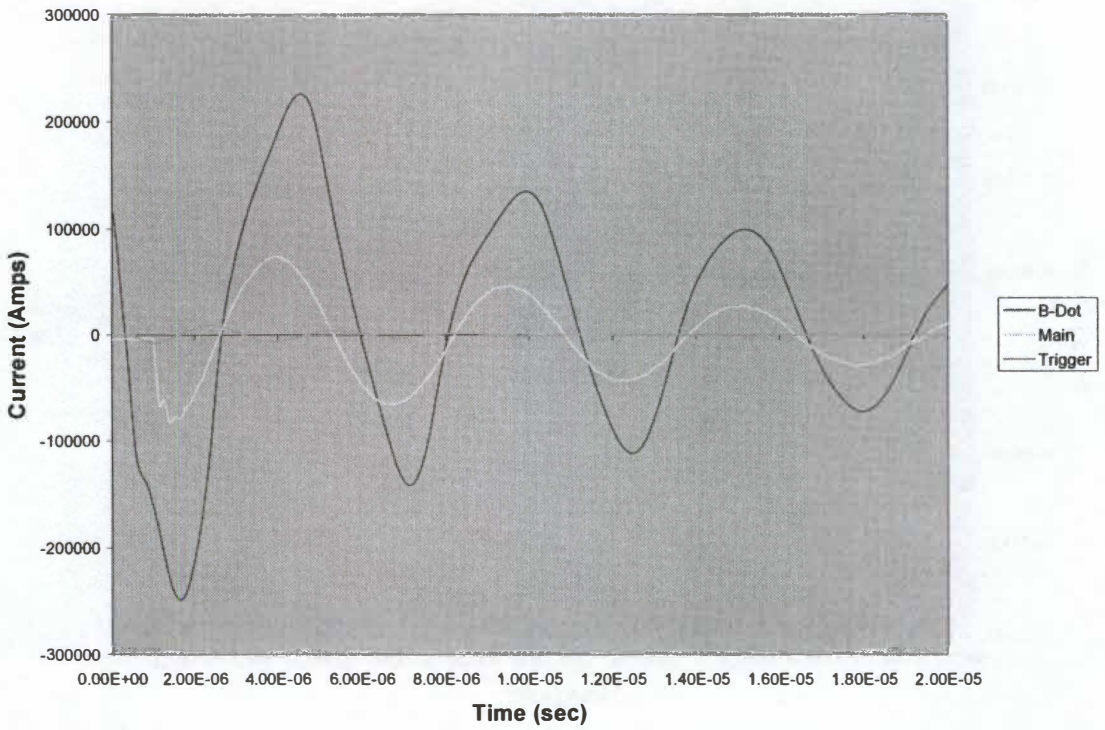


Figure 67: Integrated B-Dot Data Compared against Integrated Rogowski Coil Data

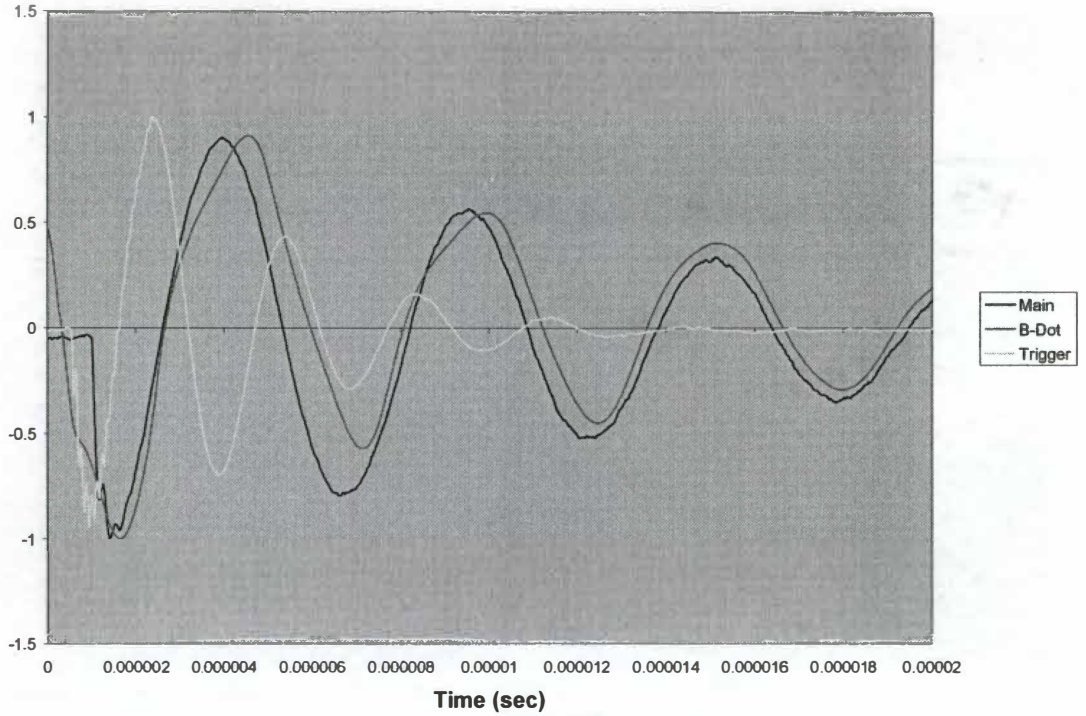


Figure 68: Normalized Rogowski Data

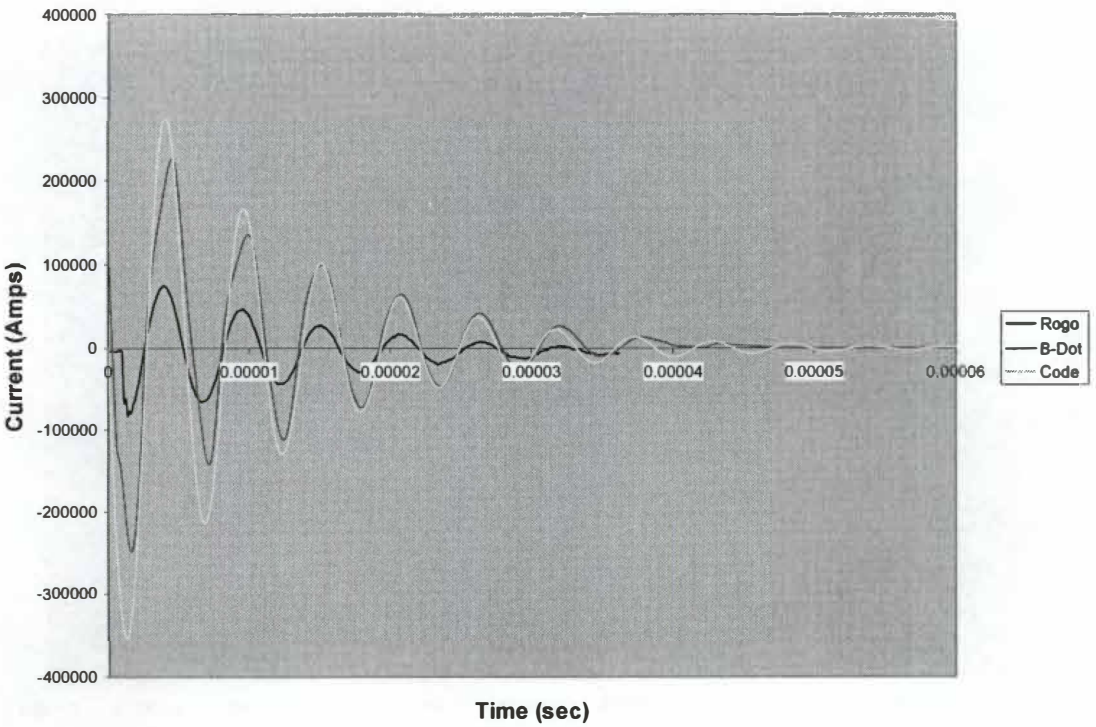


Figure 69: Circuit Analysis Compared against Integrated B-Dot Data

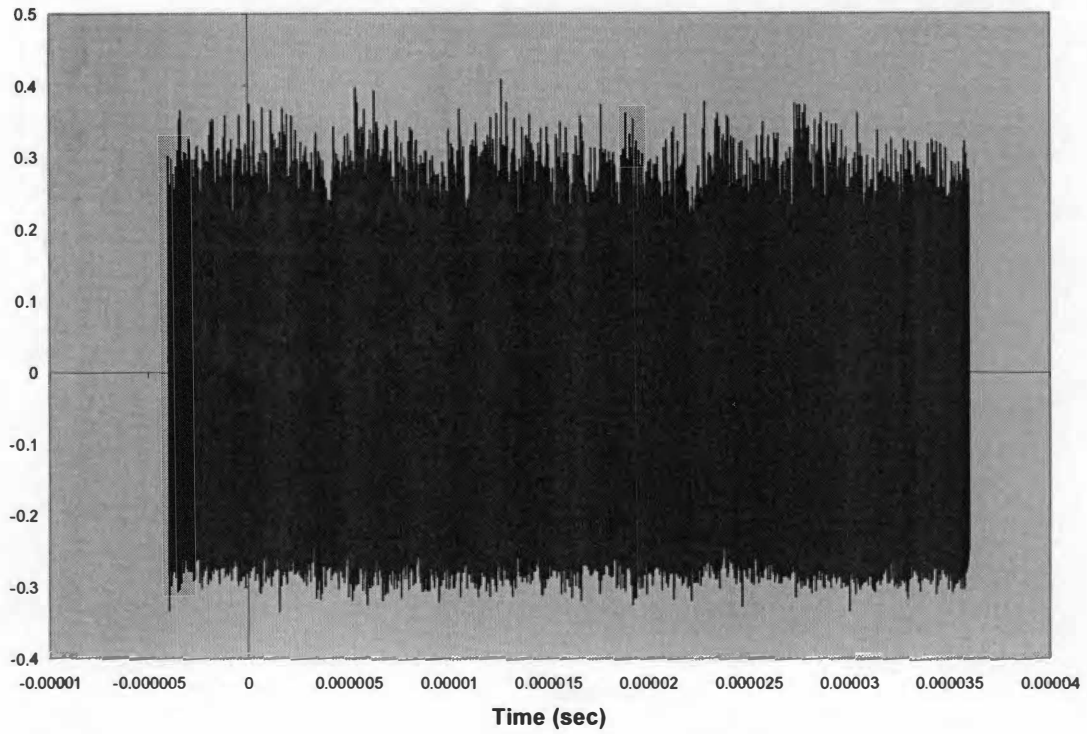


Figure 70: Raw Interferometer Data

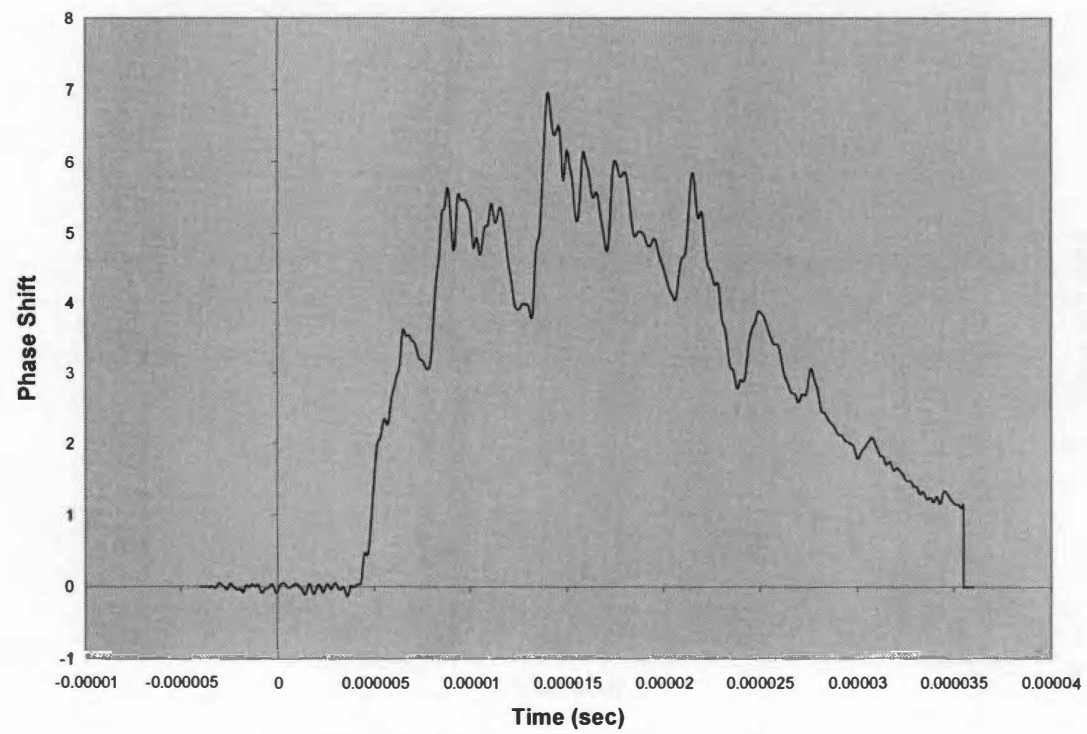


Figure 71: Interferometer Phase Shift Data

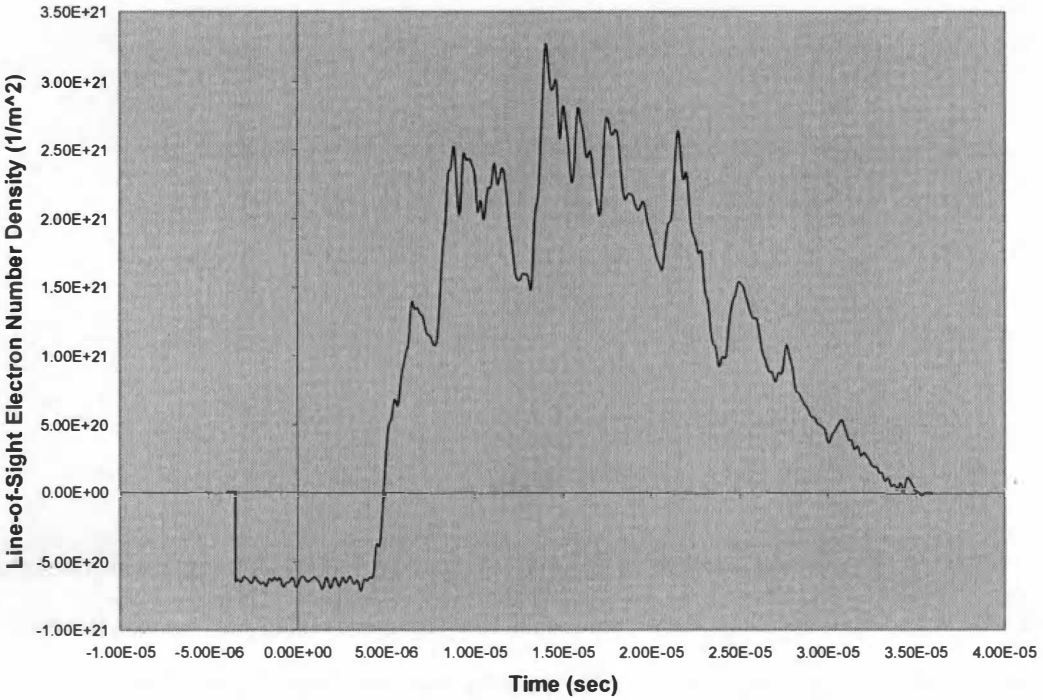


Figure 72: Interferometer Electron Number Density

Vita

Daniel Michael Rooney was born in St. Louis, MO on May 4, 1981. Up until recently he has lived his entire life in St. Louis, attending Mary Queen of the Universe grade school and Christian Brothers College High School where he graduated in 1999. From there he went to St. Louis University were he graduated with a Bachelors of Science in Aerospace Engineering in May of 2003. He finally left St. Louis to attend University of Tennessee Space Institute in Tullahoma, TN. He received his Masters of Science in Aerospace Engineering in August of 2006. Upon graduation Daniel will go to work for ATK in Elkton, MD as a project engineer.

8768 6507 15
11/08/06 VA